To the Graduate Council:

I am submitting herewith a dissertation written by C. Wayne Long entitled "Modeling of Glass Flow During Arc Fusion Splicing of Fiber Optic Filaments." I have examined the final copy of this dissertation for form and content and recommend that it be accepted in partial fulfillment of the requirements for the degree of Doctor of Philosophy, with a major in Engineering Science.

Walter Frost, Major Professor

We have read this dissertation
and recommend its acceptance:

Accepted for the Council:

Vice Provost
and Dean of The Graduate School

MODELING OF GLASS FLOW DURING ARC FUSION SPLICING OF FIBER OPTIC FILAMENTS

A Dissertation

Presented for the

Doctor of Philosophy

Degree

The University of Tennessee, Knoxville

C. Wayne Long

August 1989

DEDICATION

This dissertation is dedicated to those individuals who dare to persist in competing with themselves by striving for goals not easily attained. It is further dedicated to those who encourage and support these efforts.

ACKNOWLEDGMENTS

The author is indebted to all who have assisted and offered encouragement in this investigation. In particular, the author gratefully acknowledges the love, support, and encouragement offered by his wife Gwenn and their children; Jeff, Jennifer, and Janette.

Many have contributed their time and considerable effort, to the author's formal and informal education. As a result, this experience has been both possible and personally rewarding. Among these extraordinary individuals are Doyle Fraser, Duke Gerhardt, Bob Doehrman, and the author's major professor; Dr. Walter Frost. A special thank you is extended to Dr. Robert Turner for his singular role in providing advice and encouragement in the pursuit of the Doctoral degree program.

An acknowledgment of appreciation is extended to BDM International for its constant support as an employer. The author is grateful for advice, friendship, and research support provided by Dr. Paul Ruffin, Guidance and Control Directorate of the Research, Development, and Engineering Center at the U.S. Army's Missile Command in Huntsville, Alabama. Indebtedness is acknowledged for the counseling and technical assistance provided by FWG Associates of Tullahoma, Tennessee in their support of the Army's research efforts.

In a similar manner, a heartfelt thank you goes to the author's parents Rosie Bell and Harry Calvin, "H. C.", Long for the love and support they continually provided to their son; the author, during the many learning experiences of his youth.

ABSTRACT

Fiber optic technology is undergoing rapid development with many applications requiring direct fusion of short filaments to form one long continuous fiber. Automatic devices have been developed to heat the fiber ends in an electric discharge and bring them into contact for fusion to occur. Current practice is to establish splicing parameters for each unique splicing condition through experimental testing. This study develops an analytical model for the arc fusion splicing process. The model enables parametric studies, sensitivity analysis, quick determination of optimum splicing procedures for unique conditions, and can be used to provide analytical guidance in experimental research.

A physical model of the fiber optic splicing process is developed which incorporates heat transfer along with thermal and viscoelastic strain. An empirical model of electric discharge heating is used to supply an energy source model to one-dimensional heat transfer calculations of radiation, conduction, and convection. A numerical model is employed where temperatures are calculated for each grid element of the fiber at each time step. Physical properties of the high silica fiber optic material are modeled as functions of temperature. A two-dimensional physical model of viscoelastic glass flow is developed from force balance considerations and considers deformation due to thermal, viscous and elastic strain. Maxwell stress-strain relationships are assumed.

Finite difference numerical algorithms are derived for an Lagrangian viewpoint. Simultaneous equations for heat transfer are solved implicitly in a tri-diagonal matrix routine. Simultaneous

equations for viscoelastic flow are solved by back substitution techniques that account for boundary condition transitions upon gap closure.

Experiments were conducted using a commercial arc fusion splicer to provide experimental verification of the analytical model. Evolution of the fiber distortion was photographically recorded for repeated heating cycles of a continuous element and a free end respectively. The geometric distortion of the element with time was compared to predictions obtained with the analytical model.

The analytical model was found to display all of the physical phenomenon of the fiber deformation observed in the experiment including an unsymmetrical necking down and eventual separation of the filament. Magnitudes of the deformations were, in general, found to be overpredicted after several heating cycles.

Preliminary results indicate the relative importance of the convection heat transfer coefficient in determining the fiber's temperature profile. Viscoelastic response of the glass filament's free surface is shown to be dominated by surface tension forces. Surface profiles show a tendency to evolve unsymmetrically into a necked down region which must be countered by a press stroke during an actual splicing process.

It is concluded that the analytic model correctly simulates all major phenomenon associated with the arc fusion splicing process. Therefore, it constitutes an attractive alternative to large-scale experimentation for obtaining large data bases to be used in parametric and sensitivity analysis.

PREFACE

The research represented by this dissertation has been supported by the Guidance and Control Directorate of the Research, Development, and Engineering Center at the U.S. Army's Missile Command. Although the research was performed to advance technology used in a specific fiber optic payout system, the results have broad commercial and research applications. In addition to those applications in optical fiber splicing, the results of this work have direct applications in the manufacturing of fiber components such as fiber filaments, splitters, and tapers, where a detailed modeling of glass flow with free boundaries is needed.

TABLE OF CONTENTS

LIST OF TABLES

LIST OF FIGURES

LIST OF SYMBOLS

VARIABLES

x, y, z	cartesian coordinates
r, θ, z	polar coordinates
r, θ, ϕ	spherical coordinates
A	cross-sectional area
B	irradiation
E	Young's modulus
F	force
Fa	force due to atmospheric pressure
Fs	force due to surface tension
G	shear modulus
H	cell length
L	length
N	total number of fiber cells
p	radiation strength
Pa	atmospheric pressure
Q	heat flux
R	fiber radius
S	stress
t	time
T	temperature
U	internal thermal energy
v	velocity
V	Volume
k	thermal conductivity

A_s	surface area
C_p	heat capacity (specific heat)
h_c	convection heat transfer coefficient
I_d	electric discharge current
k_c	molecular thermal conductivity
k_{gas}	thermal conductivity of gas
k_{rad}	thermal conductivity due to radiation
n_o	index of refraction
P_e	total electric power
R_r	surface curvature in r-ø plane
R_x	surface curvature in x-r plane
T_{gl}	glass transition temperature
V_d	electric discharge voltage
å	absorption coefficient
e_λ	monochromatic emmissive power

GREEK SYMBOLS

α (alpha)	absorptivity
α_{th}	linear coefficient of thermal expansion
ß (beta)	plane angle
γ (gamma)	shear strain
δ (delta)	gap length
ε (epsilon)	strain
ε_E	elastic strain
ε_{Th}	thermal strain
ε_V	viscous strain
ε_{rad}	emissivity

ν (nu)	viscosity
κ (kappa)	thermal conductivity
λ (lamda)	wavelength
λ_{tr}	Trouton's coefficient of viscous traction
η (eta)	Poisson's ratio
ρ (rho)	density
σ (sigma)	surface tension
σ_p	standard deviation of radiation
μ (mu)	absolute viscosity
θ (theta)	plane angle
ϕ (phi)	plane angle
ψ (psi)	plane angle
ω (omega)	solid angle

CONSTANTS

c	speed of light (3×10^{10} cm/sec)
e	base, natural log (2.71828)
g	Earth's gravitational acceleration (980.7 cm/sec^2)
h	Planck's constant (6.62618×10^{-34} joule/sec)
K	Boltzman's constant (1.38066×10^{-23} joule/°K)
R_g	universal gas constant (1.98588 cal/mole-°K)
σ_{SB}	Stefan-Boltzman constant (5.67032×10^{-12} watt/cm^2-°K^4)
π	pi (3.14159)

SUPERSCRIPTS

n	time index of incremental time step

SUBSCRIPTS

i	node index of incremental fiber cell
j	interface index of incremental fiber cell
l	matrix index
m	matrix index
M	index indicating position of fiber gap
N	index indicating total number of fiber cells
r	component in radial direction
t	component in tangential direction
x	component in axial direction
0	reference value
ap	component in direction of applied force
eff	effective value
left	left interface
right	right interface
gap	related to gap between fiber ends
gas	related to gas in the electric discharge
init	initial value
cond	thermal conductivity term
conv	thermal convection term
rad	thermal radiation term
tr	component in direction transverse to applied force

MATH SYMBOLS

$\sqrt{}$	square root of
Σ	discrete sum
$\int$	integral of

$d[\ ]/dt$	time differential operator
$d[\ ]/dx$	spatial differential operator
Δ	change in value or finite difference
Ln	natural (Naperian) logarithm
Log	logarithm (base 10)
exp	exponential
$\propto$	proportional to
$[\ ]_{abs}$	absolute value operator
f( )	function of variable

MISCELLANEOUS

$\tilde{n}$	unit normal vector
°C	degree Centigrade (Celsius)
°F	degree Fahrenheit
°K	degrees Kelvin
°R	degree Rankine

CHAPTER I

INTRODUCTION

This dissertation gives the background, physical formulation, mathematical construction, and operational details of an analytical tool developed for studying fiber optic arc fusion splicing. It represents the first recorded simulation of all major physics effects, engineering parameters, material properties, and operator selectable controls throughout the fusion process.

To date, experimental studies into the optimization of splice characteristics have resulted in a relatively large empirical data base for a few specific fibers. However, each fiber type and splicing condition presently require an exhaustive series of experiments to establish a statistical data base for each variable in the splicing process.

The primary objective of this effort was to develop a computer based model to expedite analysis of the fiber optic arc fusion process by parametric studies of splicing parameters. A secondary objective was the development of an analytical tool to enable a systematic study of the influence of variables inherent in the process.

Requirements on the model were to simulate electric discharge heating, heat transfer involving a semi-transparent fiber, variation of material properties over a wide temperature range, viscoelastic flow coupled with free boundaries, and externally applied mechanical forces. In addition, the model must be capable of adjusting these conditions as a function of time.

Background

Rapid advances in fiber optic technology have placed increasing demands on the ability to perform high strength, low optical loss, inter-connections between fiber optic filaments. Fiber optic connectors have undergone a rapid improvement in their ability to satisfy these demands where size and flexibility is not a critical factor. Many other applications can only be satisfied by fusing the filaments directly together as discussed by Kao, Drake, and Long [1,2,3].[1]

Commercial devices are currently available which fuse glass fibers together by immersing the splice region in an electric glow discharge as shown in Figure I-1. This process has become popularly known as arc fusion splicing. It is noted that magnitudes of the discharge currents are typically in the milliampere range which characterize a type of discharge known as a glow discharge.[2] Details of the electric discharge are discussed in detail in Chapter II.

Virtually all arc fusion splicers have been derived from laboratory devices with their operating parameters determined empirically [4-21]. Although these experiments have shown that splicing conditions can be improved by controlling certain parameters, trade-offs are often made in splice properties [22-47]. These trade-offs are compounded by a wide variety of fiber optic filament materials and sizes in common use.

---

[1] Numbers in brackets correspond to similarly numbered references in the Bibliography.

[2] In keeping with popular terminology, the fusion process will be referred to as arc fusion splicing throughout the remainder of this dissertation.

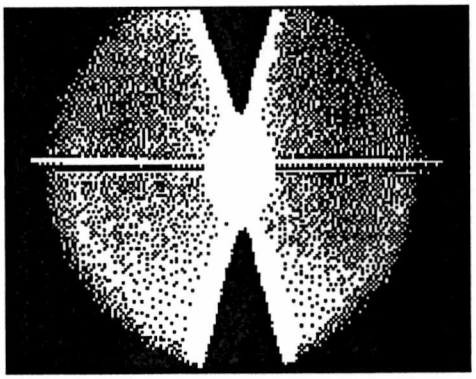

Figure I-1. Arc Fusion Splicing of Fiber Optic Filaments

No analytical technique is available to systematically investigate splice properties and the various trade-offs required with practical splicing procedures. Present practices require a series of parametric studies to derive optimum settings for each new splicing condition encountered. These studies are often very time consuming and expensive due to the stochastic nature of many of the process parameters. There is clearly a need for an analytical tool which can be used to conduct parametric studies on the effect of changes in process variables and to predict their probable distributions over a wide range of values and combinations of settings.

Fiber Optics

Fiber optic filaments are waveguides which are typically constructed with three axisymmetric layers of material; a central light conducting core region, a cladding region for maintaining light in the core, and a protective outer polymer buffer region.

Filaments of primary interest in this investigation are those in which both the core and cladding are composed of a high silica glass. These filaments are commonly found in telemetry link applications where a low optical loss and high tensile strength are required. The silica composition provides high tensile strength with very small amounts of dopant added to control the index of refraction profile.

The filaments are assumed to be of the standard 50/125 graded index construction. In this construction, a 50 micron diameter optical waveguide region is surrounded by a 125 micron diameter cladding and substrate glass region.

A polymer buffer coating is usually placed on the glass fiber optic filaments to protect its surface from abrasion and help distribute micro-bending stresses. The buffer coating typically has a 200-300 micron outer diameter. It is removed from the fiber at the arc fusion splice region and is therefore of little interest in this investigation. A cross-section of a typical fiber is shown in Figure I-2.

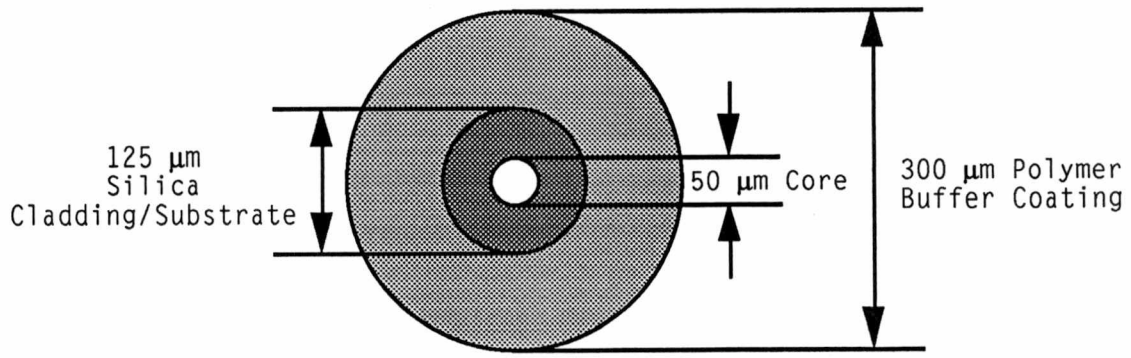

Figure I-2. Cross-Section of Typical Fiber Optic Filament

The core and cladding regions shown in the figure are typically composed of high silica glass differentiated by graded changes in the

index of refraction due to dopant material added to the glass during manufacture. The outer glass substrate layer is almost always composed of pure silica due to its high strength. Because only minute amounts of dopant material are added to the silica glass in the optical waveguide region, the physical properties of the fiber are essentially those of a pure silica glass fiber.

Arc Fusion Splicing

Arc fusion splicing of glass fiber optic filaments is accomplished in three primary operations. They consist of preparing clean, flat-faced fiber optic ends, performance of the arc fusion splicing operation, and replacement of the protective polymer coating. These operations are shown schematically in Figure I-3.

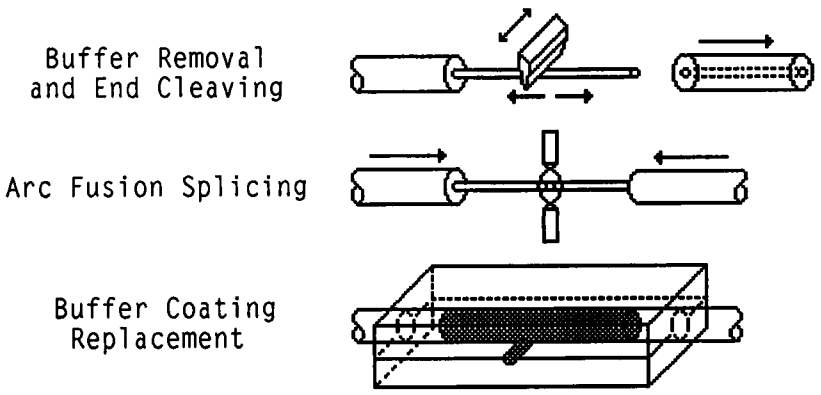

Figure I-3. Fiber Optic Arc Fusion Splicing Operations

Fiber end preparation is important because of the critical influence this region has on the splice properties. It is initiated by removal of the buffer coating from a portion of the glass fiber. This

is followed by a fiber scribing step in which a small mechanical defect is introduced into the surface of the glass filament.

A flat face perpendicular to the fiber's axis is achieved by a cleaving operation. In this operation a stress is placed on the fiber such that the defect introduced by scribing initiates a crack which propagates across the fiber.

It is noted, one step sometimes associated with the fiber end preparation is a slight rounding of the fiber ends such that each face has slight center bulge. This is usually accomplished by heating one fiber face at a time with the electric arc in a prefusion heating step. During the nominal splicing process, fibers are pressed together to insure fusion of the fiber ends. A slight center bulge in the fiber end faces allows a flow of the glass fiber material outward from the central fusion boundary.

Making initial contact at the center of the fiber along with the outward flow of material avoids gas entrapment and contributes to the removal of surface contaminants from the splice fusion region. However, the flow of material often results in a distortion of the index of refraction profile along the core/cladding boundary. In the remainder of this dissertation, perfect flat-faced fiber end faces are assumed to be used in the splicing process.

During a nominal arc fusion splicing operation, cleaned fibers with flat faced ends are clamped in axial alignment between two electrodes perpendicular to the fiber. A current is established between the electrodes by inducing electric breakdown of the air. This breakdown is maintained as an electric glow discharge which is used to

heat the fiber ends up to a temperature where they will fuse if touching.

Generally, the two heated fiber ends are then pressed together by a drive mechanism on one or both of the clamps. This motion is known as a press stroke and is performed to counter the glass's natural tendency to neck down due to surface tension effects. Additional material forced into the splice region by a press stroke has an added benefit of increasing the cross-section of the fiber in the splice region and thereby increasing its ultimate tensile strength.

A sketch showing a typical configuration used to provide fiber clamping and motion relative to the electrical discharge electrodes is shown in Figure I-4.

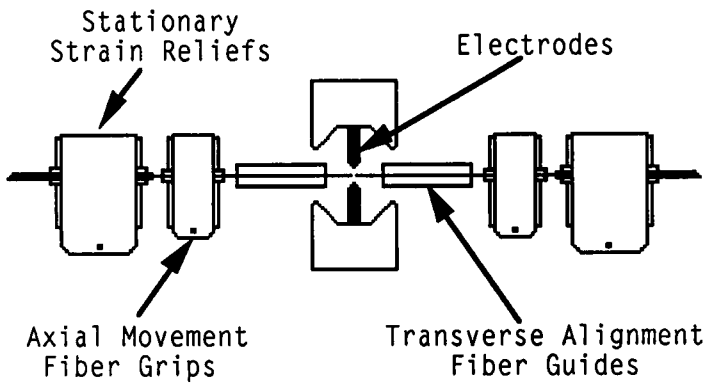

Figure I-4. Typical Fiber Grip and Electrode Configuration

Present day arc fusion splicing is usually achieved through the use of commercially available devices. Recent progress in arc fusion splicing technology has resulted in the development of automatic devices with a high degree of sophistication. Many of these devices feature

microprocessor controlled automatic fiber alignment, arc control, fiber motion, and process monitoring [61-66].

A typical commercially available arc fusion splicer is shown in Figure I-5.[3] This device features microprocessor control of the electric discharge and fiber motion. It includes a microscopic TV camera system to insure proper fiber end preparation and alignment prior to initiation of the arc fusion splicing process. In addition, the monitor provides the operator the capability to evaluating the completed splice.

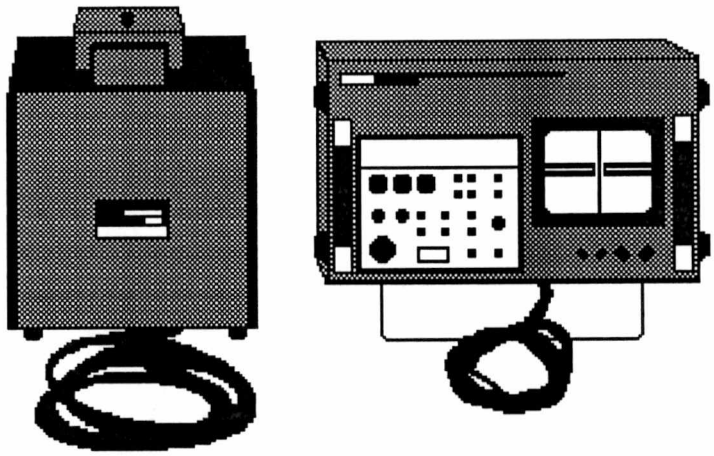

Figure I-5. Modern Commercial Arc Fusion Splicer

Experience using arc fusion splicers has demonstrated that variations in the arc fusion splicing process have a significant impact on the fiber's tensile strength and optical loss. Important factors are the fiber's physical geometry, the degree of fusion between fibers,

3 Model FSM-20 manufactured by Alcoa Fujikura Ltd. Spartanburg, South Carolina.

devitrification into crystalline states, residual thermal stresses, and disruption of the waveguide properties by glass flow [52-60].

Review of Technology Supporting Model Development

No attempt to model the splicing process and analytically study the optimization of splicing parameters has been reported. One reason for this lack of a comprehensive analytical tool for studying the splicing process is the large number of fairly complex individual physical processes which must be simulated in a coupled model.

Thermal energy is provided by an AC glow discharge between closely spaced pointed electrodes in air. Transient heat transfer to, and from, the semi-transparent glass filament occurs by a combination of convection, conduction, and radiation. Under the imposed heating conditions, viscoelastic response of the glass includes free surfaces controlled by surface tension in strong thermal gradients, thermal and viscoelastic strain, and glass fusion of fiber filament faces.

Considerable effort has been expended in characterizing the properties of glass and silica as a function of temperature. Much information on the viscous nature of silicate glass, glass transition effects, and the transfer of heat in semi-transparent material was obtained from efforts supporting the commercial glass industry [66-99]. Recent demands for improved performance of glass materials has resulted in increased material characterizations of high silica glass and quartz including those specifically on fiber filaments [100-109]. Information on silica properties used in this study is given in Appendix A.

Heat transfer and glass flow in forehearths has received considerable attention [110-114]. In these treatments, the glass is

assumed to be optically thick and conducts heat following the Rosseland approximation.

In the Rosseland approximation, an effective thermal conductivity is used which is the sum of the conventional thermal conductivity term and a radiation term which varies with the cube of temperature. The Rosseland approximation was found to be appropriate along the fiber's axis but not transverse to it due to large variations in the radiation path length. This is discussed in detail in Appendix A.

Analysis of glass flow in furnace forehearths universally treats the glass as a fluid using the Navier-Stokes relationship for viscous flow [115-125]. These were found to be inadequate for analysis of the arc fusion splicing process due to the lack of significant material flow and the need to include viscoelastic effects.

Analysis of glass flow in the drawing process used to manufacture fiber optics also treats the glass as a fluid using the viscous Navier-Stokes relationship [126-138]. As in the case of the glass furnace forehearths, glass flow is treated as a steady state problem. Here, the Rosseland approximation is not used because the glass fiber is shown to be optically thin. Heat transfer is modeled as being one dimensional with air quench cooling times found to be on the order of seconds [100, 101, 109, 129, 130]. Surface contours of the fibers are treated as free boundaries dominated by surface tension forces.

Surface tension forces have been shown to be dominant for liquid bridges with a small cross sections such as that of a fiber optic filament [139-160, 199, 200]. In silica glass, as for most materials, these forces are a function of temperature and may result in fluid flow when temperature gradients are present [201, 202].

Heat is provided to the arc fusion splicing process by an AC electric discharge between pointed electrodes in air. Several general reviews of electric discharges provide guidelines which classify the arc fusion splicing discharge as a high pressure glow discharge type [161-165].) Glow discharges are characterized by a relatively constant potential drop between electrodes over a relatively wide range of current values. High pressure discharges are collision dominated and therefore have their component species in local thermal equilibrium.

Measurements on high voltage breakdowns of real gases in uniform electrical fields have shown the breakdown voltage to be linearly related to the separation distance between the electrodes [166-171]. After breakdown, joule heating of conduction electrons in a high pressure discharge is quickly transferred to other species of the gas by both radiation and conduction [172-177]. The heating profiles in these discharges have been shown to exponentially decay with increasing distance from the discharge axis in the steady state case [178-181].

No complete analysis has been reported which treats the specific conditions of an AC glow discharge in air at atmospheric pressure between pointed electrodes as found in the arc fusion splicer. However, experimental measurements have been made on the radiation emitted by such discharges and empirical relationships have been derived which give the discharge's radiant energy as a function of position [8, 9, 10, 46, 47]. This information has been used to derive the heating profile of the fiber as a function of its position in the discharge as described in Chapter II.

Overview of Report

Chapter II of this report gives the development of physical models and assumptions for the arc fusion splicing process, formulation of governing equations along with initial and boundary conditions, numerical algorithms in finite difference form, and the computation methodology used to obtain a solution.

Chapter III gives the results of analytical and experimental tests performed to compare with the predictions of the analytical model. The experiment performed was a modification of the arc fusion splicing process that was adapted to simplify and isolate specific physical mechanisms. Significance of the comparison is described relative to the predicted deformation, stress concentrations, and temperature variations along the fiber optic filament's length. Agreement with various physical effects reported in the open literature and outlined in the previous sections is shown. Weaknesses in the model are identified and methods of alleviating these are identified.

Chapter IV gives the conclusions reached as a result of this study and recommendations for further work to advance this effort.

Physical properties of silica fibers are given in Appendix A. These are developed in a form useful for inclusion into the numerical algorithms and were given as a function of temperature where appropriate.

Calculations and rationale justifying the assumption of negligible gravitational forces are given in Appendix B.

A discussion of the computer program used to solve the numerical algorithms is given in Appendix C. Program structure, control flow and a discussion of the action of individual subroutines are given.

CHAPTER II

GOVERNING EQUATIONS AND NUMERICAL ALGORITHMS

An examination of the arc fusion splicing process for high silica fibers reveals several features which must be incorporated into any model used for analysis. First, the process is inherently transient in nature. It includes glow discharge heating and open air quenching of a semi-transparent material with a filament geometry. This heating and cooling results in changes in material characteristics and molten free surfaces controlled by viscous and surface tension effects. The physical properties of silica are such that viscoelastic responses throughout the glass transition and softening range must be included in the model.

Successful modeling of the arc fusion splicing process requires the development of coupled heat transfer and viscoelastic response models. This coupled model should be capable of accommodating changes in fiber optic properties with temperature resulting in a highly nonlinear system of governing equations. A lack of closed form solutions for these governing equations requires the application of numerical techniques. Validation and calibration of the coupled model with data from the existing experimental data base along with selected additional experiments will then yield a useful analytical tool. These stages of development for the arc fusion splicing analytical tool are shown graphically in Figure II-1.

The following sections discuss the physical models, governing equations, and numerical algorithms used to represent heat transfer, and the stress/strain relationships associated with the viscoelasticity of a

fiber undergoing an arc fusion splicing process. Initial conditions, boundary conditions, and a discussion of computation methodologies used in the analysis are included where appropriate.

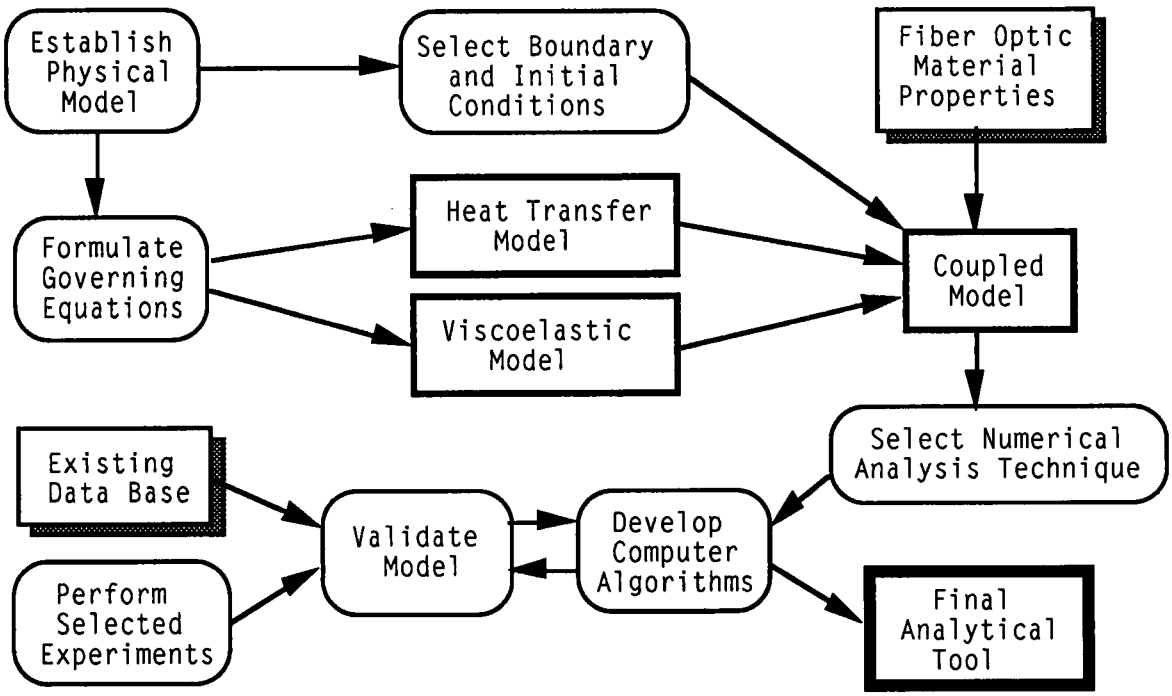

Figure II-1. Development Stages for Arc Fusion Splicing Model

Physical Model of Splicing Process

Analysis of the physical response of the fiber filament to discharge heating and relative motion requires the development of a coupled heat transfer and viscoelastic response model. This coupled model must be capable of simulating each phase of the arc fusion process. Specifically, it must including glow discharge heating, viscoelastic material response, fusion of individual fibers, surface

tension at a free boundary, and air quench cooling. In addition, provision must be made to simulate an initial gap between fiber ends, their relative motion with respect to each other, the electric discharge heat flux, as well as the elastic compression of the fibers due to mechanical motion of fiber grip mechanisms. These interactions are shown schematically in Figure II-2.

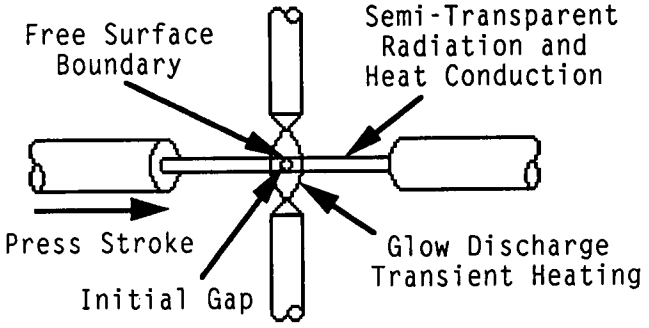

Figure II-2. Interactions in Arc Fusion Splicing

Fibers were assumed to be homogeneous silica cylinders with perfectly prepared end faces. Silica properties were assumed to be functions only of the fiber temperature. This assumption has been found to be acceptable when modeling the physical properties of a wide range of silica glass compositions [110-114].

The fiber is a strongly one dimensional structure, being symmetric about its axis and having relatively minor variations in its radial direction. Minor radial variations are created during manufacturing to control optical waveguide properties. These radial variations are engineered to minimize discontinuities in the physical properties of the fiber. Temperatures in the fiber were assumed to be constant in cross-section with variations only in the axial direction because the fiber

was so thin. This assumption is in keeping with reported models of the fiber drawing process [100, 101, 109].

Conditions of the splice were assumed to be such that the process is axisymmetric. Arc heating is assumed to be evenly distributed radially around the fiber filaments and the cross section of the fiber remains circular. Allowances were made to permit the position of the fiber to vary with regard to its axial position in the electric discharge heat flux because of the manner in which the fiber motion is modeled.

Phases of the arc fusion process which must be simulated include the response of the individual fibers while separated as well as the response of an effectively continuous fiber length after the gap closes. The fiber was allowed to expand or contract into or out of the heat flux distribution with time. Special provision was included in the model to simulate the existence of a gap between fiber end faces and changes during gap closure. Upon closure, transient boundary conditions were employed to simulate compression of the fiber due to the imposed motion of the gripping mechanisms. Boundary condition were also changed to simulate the transition from glow discharge heating to natural convection cooling in air.

Before discussing the individual physical models used in the analysis of the arc fusion splicing, it is useful to consider several features of the process. First, changes in the system typically occur smoothly over a relatively long temporal and spatial period. Examples of this are evidence in previous workers' analysis of glass flow during the drawing of fiber filaments where temperature and material motion tend to be smoothly varying functions [126-138]. Second, melting of

glassy materials occurs over a relatively broad glass transition temperature range in which properties, such as viscosity, change smoothly. This is in contrast to the sharp change in material properties over a narrow temperature range typical of many melting phase transitions.

Overview of Computational Methodology

The methodology used in the analysis is to numerically time-step through the arc fusion splicing process. A heating cycle was initiated by instantaneously imposing the modelled heat flux on the room temperature fiber. During subsequent time steps, a new temperature distribution for the fiber is determined from heat transfer calculations based on the physical geometry and physical properties of the previous time-step. Material properties for the current time-step are determined using this updated temperature distribution. Material responses are calculated using a stress/strain model with the updated material properties. Results of the updated fiber geometry and physical properties are output. The sequence of calculations is indicated in Figure II-3.

Physical processes modeled in the calculation sequence included heat transfer from a glow discharge in air, heat transfer within the semi-transparent fiber material, viscoelastic response of the heated glass, fusion of contacting fiber interfaces, motion of the free boundary under the influence of surface tension, and cooling by quenching in air. Each model is discussed in detail in the following sections. In each, the process has been assumed to be axisymmetric with boundary condition changes applied instantaneously.

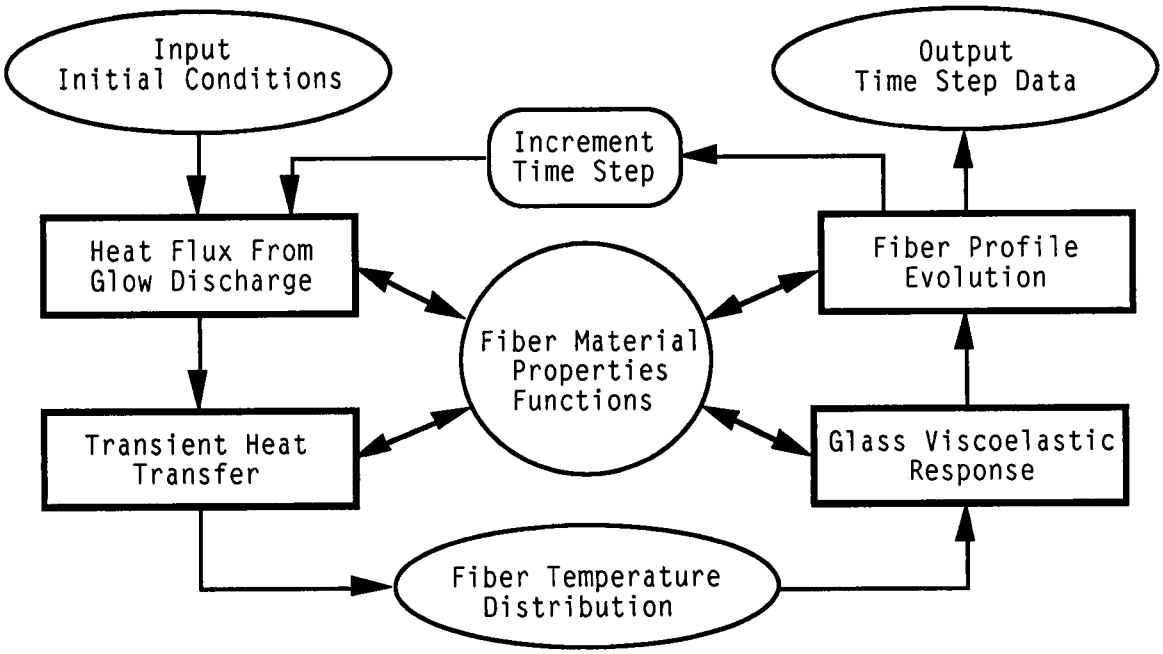

Figure II-3. Sequence of Calculations for Each Time-Step

Numerical Technique

Fiber properties and temperature are assumed to be constant in cross-section. For modeling purposes, the length of fiber between grips is divided into a number of cells along its length. Each cell is assigned a node at its center and an interface boundary between each of its nearest neighbors. Cell interfaces and nodes are numbered starting at the leftmost grip location.

The notation used to track cell nodes and interfaces is depicted in Figure II-4. The origin is taken to be at the leftmost fiber grip/fiber interface boundary. All nodal and interface positions are, therefore, referenced to this location.

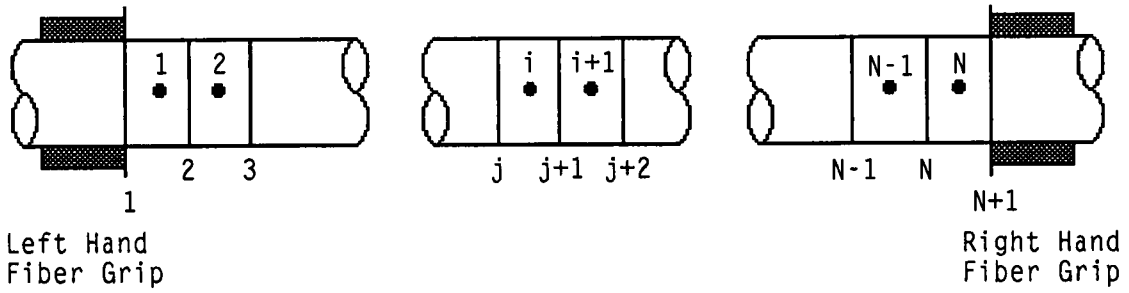

Figure II-4. Notation Used in Numerical Model

Variables used in the numerical algorithms are identified as being evaluated at a fiber cell nodal or interfacial positions in addition to the calculation time step. Variable subscripts, i, designate the value of the parameter at the midpoint of the i^{th} cell. Subscripts, j, designate the j^{th} cell interface. Superscripts, n, designate the n^{th} time step.

Fiber temperature and properties were assumed to be constant throughout the volume of each cell as discussed previously. Temperatures were determined at cell nodal points by direct solution of the governing energy equation. Temperatures at cell interfaces were calculated from a linear interpolation between nodal temperatures as given by:

$$T_j = (T_{i-1} + T_i)/2 \qquad \text{(Eq. II-1)}$$

where T_j is the temperature at the j^{th} interface

T_{i-1} is temperature of previous cell node

T_i is temperature of following cell node

Each cell is initially given the same length of $L/(N + 1)$, where L is the combined fiber length between grips and N is the total number of

nodes, or cells. As the fiber undergoes viscoelastic deformation each fiber cell length is determined from the position of the cell interfaces and is given by:

$$H_i = x_{j+1} - x_j \qquad \text{(Eq. II-2)}$$

where H_i is the length of the i^{th} cell

x_{j+1} is the position of the interface on the right side of the i^{th} cell

x_j is the position of the interface on the left side of the i^{th} cell

An initial gap is located at the cell interface labeled M+1 by modifying the size (length) of the free fiber end cells labeled M and M+1 as shown in Figure II-5.

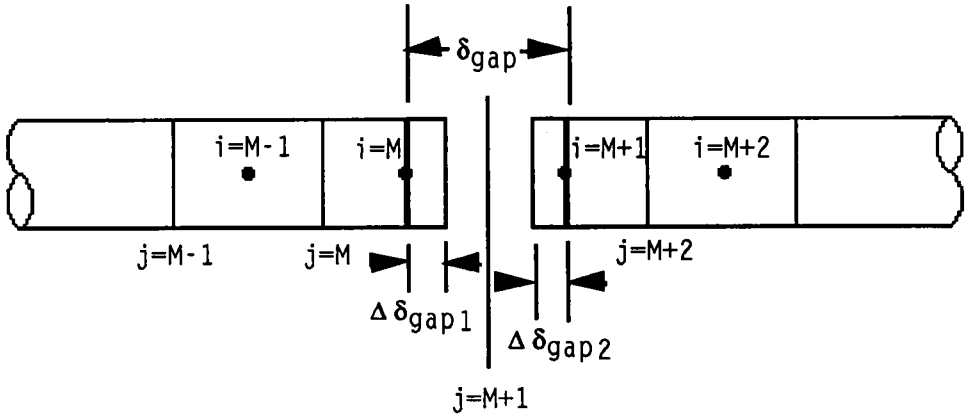

Figure II-5. Notation Used to Model the Gap Region

This notation for the gap region allows for the transition from a condition where the fiber free ends are exposed to glow discharge heated gas to a condition where the fiber ends make contact due to thermal

expansion and the press stroke. The cell interface labeled M+1 was nominally positioned in the middle of the fiber length at the (N/2)+1 interface to model an arc fusion splicing operation and moved near the left fiber grip to model the electric discharge heating of a continuous length of fiber.

Special consideration is given to modeling the gap that initially exists between fibers. The gap was initially assumed to occur in the middle of the length of the fiber filament typical of the gap position in an arc fusion splicing operation. Later the model was modified to allow the gap position to be specified as being anywhere between the fiber grips except for the first or last three cell interfaces. In this manner, the glow discharge heating of a continuous fiber filament with one free end could be modeled.

A finite difference numerical technique was used to solve the governing equations and to track the evolution of individual cells. Heat transfer and stress-strain interactions among fiber cells occured only between nearest neighbors. Radiation heat transfer through the semi-transparent silica fiber material from distant cell neighbors is accounted for in an effective conductivity term. This is discussed in detail in a later section.

Nodes and interfaces were assumed to be fixed with respect to the fibers, in keeping with an Lagrangian viewpoint (i.e., no mass flux across interfaces). Relative movement of the fiber was tracked by computing the central nodal position due to thermal, elastic, and viscous strain as well as any motion imposed by the press stroke during a given time step.

Governing equations were written in implicit form by using values for physical properties and fiber contours calculated from the previous time step. Energy balance equations governing heat transfer were formulated in a tri-diagonal matrix form for ease of computer solution using standard routines [182]. Force balance equations governing viscoelastic response were formulated in a marching solution format. An overview of the computer code generated to solve the governing equations is given in Appendix C. Details of the governing equation formulation are discussed in the following sections.

Heat Transfer in Fiber Filaments

Analysis of heat transfer in the fiber optic filaments was conducted by establishing an energy balance for each finite cell volume. In this analysis, the fiber is treated as a thin cylindrical rod. Heat transfer processes in the fiber are assumed to be symmetric about its central axis. Also, because the rod is very thin, the temperature is assumed uniform over any given cross-section. The fiber is assumed to be heated asymmetrically in the axial direction but symmetrically in the peripheral direction. Heat flux through the surface is permitted to vary with time and axial position. This reduces the problem to that of one-dimensional heat transfer along the fiber.

Thermal energy enters (and leaves) each fiber cell from the discharge gas energy source by radiation and convection heat transfer. In addition, thermal energy enters and leaves each cell through neighboring cells by radiation and conduction. These interactions are shown in Figure II-6.

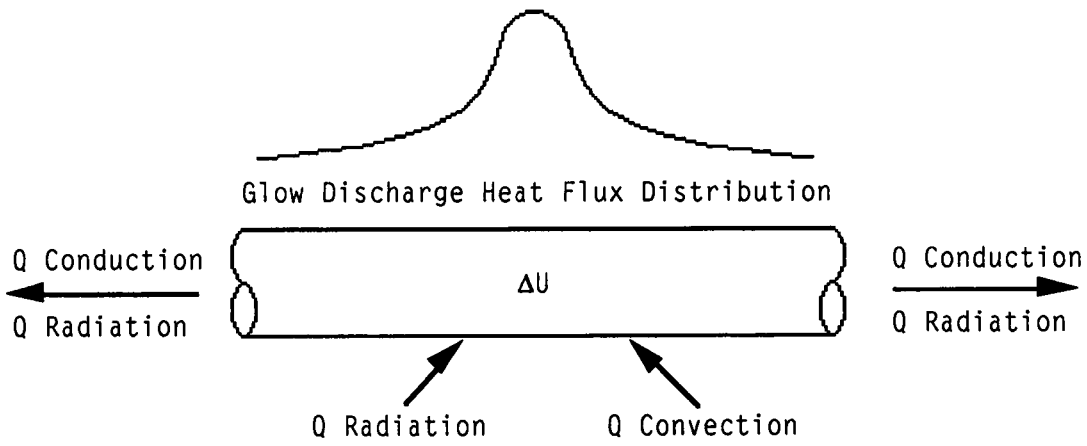

Figure II-6. Elements of Heat Flux in Fiber Cell Energy Balance

An energy balance is formulated for each cell. These equations relate the temperature within each cell to the sum total of all heat transfer into and out of each cell. The energy balance equation for each cell volume is given by:

$$dU/dt = \Delta Q_{conduction} + \Delta Q_{convection} + \Delta Q_{radiation} \quad \text{(Eq. II-3)}$$

where dU/dt is rate of change of internal energy

$\Delta Q_{conduction}$ is the net heat transfer due to conduction

$\Delta Q_{convection}$ is the net heat transfer due to convection

$\Delta Q_{radiation}$ is net heat transfer due to radiation

The temperature of each cell is a function of the thermal energy present. Both the temperature and thermal energy of each cell changes with time as heat is transfered across cell boundarys. The change of thermal energy within each cell volume with respect to time, dU/dt, is given by:

$$dU/dt = \rho(T)C_p(T)V(T)\ d[T]/dt \qquad \text{(Eq. II-4)}$$

where dU/dt is the rate of change of internal energy

$\rho(T)$ is density

$C_p(T)$ is specific heat

$V(T)$ is volume of the cell

$d[\ ]/dt$ is time derivative operator

T is the cell temperature

As shown, material properties of the fiber are considered to be functions of the local temperature from the previous time step. The product of density and cell volume is constant due to conservation of mass considerations. The finite difference form of this equation is given by:

$$(dU/dt)_i^{n+1} = F_i^n T_i^{n+1} - F_i^n T_i^n \qquad \text{(Eq. II-5)}$$

where $(dU/dt)_i^{n+1}$ is rate of energy change in the i^{th} cell at the $n+1^{th}$ time step

T_i^n is temperature at the i^{th} node at the n^{th} time step

T_i^{n+1} is temperature at the i^{th} node at the $n+1^{th}$ time step

The F_i^n term in the above equation is given by:

$$F_i^n = \rho(T_i^n)C_p(T_i^n)V_i^n/\Delta t \qquad \text{(Eq. II-6)}$$

The volume of the i^{th} cell at the n^{th} time step, V_i^n, is taken to be a truncated cone with a value given by:

$$V_i^n = \pi[(R_{j+1}^n)^2 + R_{j+1}^n R_j^n + (R_j^n)^2]H_i^n / 3 \qquad \text{(Eq. II-7)}$$

where V_i^n is volume of the i^{th} cell at the n^{th} time step

R_j^n is radius at the j^{th} interface at the n^{th} time step

H_i^n is axial length of the i^{th} cell at the n^{th} time step

(see Eq. II-2)

Conduction heat transfer between fiber cells is governed by Fourier's heat conduction equation and is given by:

$$q_{cond} = -kAdT/dx \qquad \text{(Eq. II-8)}$$

where q_{cond} is heat flux

k is the thermal conductivity

A is the cross sectional area of the interface

dT/dx is the temperature gradient along the fiber

The finite difference form of the equation for heat conduction to each cell from the neighboring cell to the left is given by:

$$Q_{left}cond_i^{n+1} = k(T_j^n)A_j^n(\Delta T_{left}^{n+1}/\Delta x_{left}^n) \qquad \text{(Eq. II-9)}$$

where $Q_{left}cond_i^{n+1}$ is heat conduction across the j^{th} interface at the $n+1^{th}$ time step

$k(T_j^n)$ is thermal conductivity based on the j^{th} interface temperature at the n^{th} time step

A_j^n is the area of the j^{th} interface at the n^{th} time step

Here, ΔT_{left}^{n+1} is the temperature difference between the midpoints of neighboring cells and is given by:

$$\Delta T_{left}^{n+1} = (T_{i-1}^{n+1} + T_{i-1}^{n})/2 - (T_i^{n+1} + T_i^{n})/2 \qquad \text{(Eq. II-10)}$$

where T_i^n is the temperature at the i^{th} node

following the Crank-Nicholson method of finite differencing [182]. The finite difference form of the distance between midpoints of neighboring cells, Δx_{left}^n, is given by:

$$\Delta x_{left}^n = (H_{i-1}^n + H_i^n)/2 \qquad \text{(Eq. II-11)}$$

where H_i^n is the length of the i^{th} cell (see Eq. II-2)

This can be written in terms of cell interface positions as given by:

$$\Delta x_{left}^n = (x_{j+1}^n - x_{j-1}^n)/2 \qquad \text{(Eq. II-12)}$$

where x_{j+1}^n is the position of the $j+1^{th}$ interface

The finite difference form of the equation for heat conduction to each cell from the neighboring cell to the right is given by:

$$Q_{right\,cond_i}^{n+1} = k(T_{j+1}^n)A_{j+1}^n(\Delta T_{right}^{n+1}/\Delta x_{right}^n) \qquad \text{(Eq. II-13)}$$

where $Q_{right\,cond_i}^{n+1}$ is heat conduction across the $j+1^{th}$ interface at the $n+1^{th}$ time step

$k(T_{j+1}^n)$ is effective thermal conductivity across the $j+1^{th}$ interface at the n^{th} time step

A_{j+1}^n is area of the $j+1^{th}$ interface at the n^{th} time step

Here, ΔT_{right}^{n+1} is given by:

$$\Delta T_{right}^{n+1} = (T_i^{n+1} + T_i^n)/2 - (T_{i+1}^{n+1} + T_{i+1}^n)/2 \quad \text{(Eq. II-14)}$$

where T_i^n is the temperature at the i^{th} node

and Δx_{right}^n is given by:

$$\Delta x_{right}^n = (H_{i+1}^n + H_i^n)/2 = (x_{j+2}^n - x_j^n)/2 \quad \text{(Eq. II-15)}$$

where H_i^n is the length of the i^{th} cell (see Eq. II-2)

x_j^n is the position of the j^{th} interface

By combining the previous equations, the total heat transfer due to conduction for the i^{th} cell is given by:

$$\Delta Qcond_i^{n+1} = K_j^n T_{i-1}^{n+1} - (K_j^n + K_{j+1}^n) T_i^{n+1} + K_{j+1}^n T_{i+1}^{n+1} + K_j^n T_{i-1}^n - (K_j^n + K_{j+1}^n) T_i^n + K_{j+1}^n T_{i+1}^n \quad \text{(Eq. II-16)}$$

Here, K_j^n is given by:

$$K_j^n = k(T_j^n) A_j^n / (H_{i-1}^n + H_i^n) \quad \text{(Eq. II-17)}$$

where $k(T_j^n)$ is effective thermal conductivity across the j^{th} interface

A_j^n is area of the j^{th} interface

H_i^n is the length of the i^{th} cell (see Eq. II-2)

and A_j^n is given by:

$$A_j^n = \pi(R_j^n)^2 \qquad \text{(Eq. II-18)}$$

where R_j^n is the radius of the j^{th} interface

The coefficient of thermal conductivity used in the above equations is an "effective" coefficient which includes contributions from both radiation and conduction from neighboring cells following the Rosseland approximation [69]. In this approximation, radiation heat transfer for transparent materials is treated as conduction heat transfer in the optically thick limit which is assumed to exist for radiation along the fiber.

Using the Rosseland approximation, the coefficient of thermal conductivity due to radiation is added to that for traditional conduction to yield an "effective" coefficient of thermal conductivity. This value is used in place of the coefficient of molecular thermal conductivity in conduction heat transfer equations. The effective thermal conductivity for the transparent silica fiber material is given by:

$$k_{eff} = k_{cond} + 16n_o^2\sigma_{SB}T^3/3\text{å} \qquad \text{(Eq. II-19)}$$

Where k_{eff} is the effective thermal conductivity

k_{cond} is molecular thermal conductivity

n_o is the index of refraction

T is the absolute temperature

σ_{SB} is Stefan-Boltzmann's constant

å is the absorption coefficient

The finite difference form of the equation for the effective thermal conductivity is given by:

$$k(T_j^n) = k_c(T_j^n) + 16n_o^2\sigma_{SB}(T_j^n)^3/3\mathring{a} \qquad \text{(Eq. II-20)}$$

Where $k(T_j^n)$ is the effective thermal conductivity at the j^{th} interface at the n^{th} time step

$k_c(T_j^n)$ is molecular thermal conductivity at the j^{th} interface at the n^{th} time step

T_j^n is temperature of the j^{th} interface at the n^{th} time step

Heat flux in the form of radiation and convection heat transfer enters and leave the exposed surface of the fiber in a radial direction. Heat flux in the form of radiation and conduction heat transfer enters and leaves each fiber cell in an axial direction. Radiation heat flux from the electric discharge heated air is modeled as the heat flux profile along the length of fiber in agreement with the relationships discussed in previous sections.

Convection heat transfer to the surface of the fiber optic filament is given by:

$$q_{conv} = h_c A\Delta T \qquad \text{(Eq. II-21)}$$

where q_{conv} is the heat flux

h_c is convection heat transfer coefficient

A is the surface area

ΔT is difference in effective gas temperature and the fiber surface temperature

The finite difference form of the equation for convection heat transfer of the i^{th} cell is given by:

$$\Delta Qconv_i^{n+1} = h_{Ci} A_i^n \Delta T_i^{n+1} \qquad \text{(Eq. II-22)}$$

where $\Delta Qconv_i^{n+1}$ is convection heat transfer at the i^{th} cell at the $n+1^{th}$ time step

h_{Ci} is the convection heat transfer coefficient

A_i^n is the surface area of the i^{th} cell at the n^{th} time step

The temperature difference, ΔT_i^{n+1}, between the fiber and gas at the surface of the i^{th} cell is given by:

$$\Delta T_i^{n+1} = T_{gasi}^n - (T_i^{n+1} + T_i^n)/2 \qquad \text{(Eq. II-23)}$$

Where T_{gasi}^n is an effective temperature for convection of the gas at the i^{th} cell during the n^{th} time step

Eq. II-8 can, therefore, be written as:

$$\Delta Qconv_i^{n+1} = C_i^n(2T_{gasi}^n - T_i^n) - C_i^n T_i^{n+1} \qquad \text{(Eq. II-24)}$$

where $C_i^n = (h_{Ci} A_i^n)/2$

The surface area of the cell is modeled by assuming each cell has the shape of a truncated cone. The lateral surface of a truncated cone is given by:

$$A_S = \pi(r_1 + r_2)\sqrt{[H^2 + (r_2 - r_1)^2]} \qquad \text{(Eq. II-25)}$$

where A_S is surface area

r_1 and r_2 are the cell end radii

$\sqrt{[\ ]}$ is square root operator

H is cell length

Therefore, the finite difference form for the surface area, A_i^n, is given by:

$$A_i^n = \pi(R_{j+1}^n + R_j^n)[(R_{j+1}^n) - R_j^n)^2 + (H_i^n)^2]^{1/2} \qquad \text{(Eq. II-26)}$$

where A_i^n is surface area of the i^{th} cell at the n^{th} time step

R_{j+1}^n is $j+1^{th}$ interface radius at the n^{th} time step

R_j^n is j^{th} interface radius at the n^{th} time step

H_i^n is length of the i^{th} cell at the n^{th} time step

The coefficient of heat transfer is sensitive to glow discharge gas properties, fiber geometry, surface roughness, and fluid flow conditions. It will, in general, be a function of relative gas motion which varies along the fiber in the electric discharge heat zone. Furthermore, the temperature of the gas changes from that of the electric discharge heated air to that of room temperature air as the arc fusion process changes from the electric discharge heating phase to the air quench cooling phase.

Values of the convection heat transfer coefficient for a fiber in a glow discharge are not readily available. Further study is required to establish its functional dependence on position in the discharge and the thermal properties of the discharge plasma itself. Therefore,

although the model has the capability of specifying the coefficient of convection heat transfer as a function of position along the fiber, for the purposes of this analysis, it was taken as being constant during both the heating and cooling phases of the arc fusion splicing process. Magnitudes were estimated from values reported for horizontal cylinders undergoing natural convection.

Heat transfer to and from each fiber cell due to radiative exchange with the surrounding glow plasma for each fiber cell is given by:

$$\Delta Q_{radiation} = Q_{in}{}_{rad} - Q_{out}{}_{rad} \qquad \text{(Eq. II-27)}$$

where $\Delta Q_{radiation}$ is effective radiation heat transfer

$Q_{in}{}_{rad}$ is the radiation energy absorbed by the cell

$Q_{out}{}_{rad}$ is the radiation energy emitted by the cell

Radiation energy absorbed by each fiber cell is a function of the cell surface area and is given by:

$$Q_{in}{}_{rad} = \alpha B_{gas} A \qquad \text{(Eq. II-28)}$$

where $Q_{in}{}_{rad}$ is radiation heat transfer from the gas

α is fiber absorptivity

B_{gas} is irradiation impinging on the surface of the fiber

A is the surface area of the fiber

Radiation heat transfer from each fiber cell is a function of both the cell surface area and its temperature and is given by:

$$Q_{out}rad = \varepsilon_{rad}\sigma_{SB}T^4A \qquad \text{(Eq. II-29)}$$

where $Q_{out}rad$ is radiation emitted from the fiber

ε_{rad} is fiber emissivity

σ_{SB} is Stefan-Boltzmann's constant

T is temperature of the fiber

A is the cell surface area

Both heat transfer equations for radiation into and from the i^{th} cell of the fiber can be combined into a single finite difference form given by:

$$Qrad_i^{n+1} = I_i^n - E_i^nT_i^{n+1} \qquad \text{(Eq. II-30)}$$

where $I_i^n = \text{å}(T_i^n)B_iA_i^n$

$E_i^n = \varepsilon(T_i^n)\sigma_{SB}(T_i^n)^3A_i^n$

$\alpha(T_i^n)$ is fiber absorptivity

$\varepsilon(T_i^n)$ is fiber emissivity

B_i is irradiation on surface of cell from gas

A_i^n is surface area of cell (see Eq. II-26)

σ_{SB} is Stefan-Boltzmann's constant

The fiber was assumed to absorb and emit radiation as a gray-body. In this case the absorptivity is equal to the emissivity for all radiation wavelengths and all fiber temperatures. It is noted that variations in both of these is significant if the thickness of the silica is less than 0.2 cm. For the case of a 125 μm fiber filament they have been estimated as having a constant value of 0.1 [136]. This value is used for both the absorptivity and emissivity in the analytical

model. It should be noted that a more complex function can be input to the model if determined necessary.

The first and last nodes require boundary conditions and those at the gap region require special treatment in the equations for axial conduction heat transfer. The gap in a nominal splicing operation is near the midpoint of the electric discharge where the heating is relatively symmetric. In this case the differences between the gap interface temperatures raised to the fourth power will, in general, be small. Therefore, the major mechanism of heat transfer across the gap region is assumed to be simply that of conduction through the air in the gap.

The location of the last fiber cell node prior to the gap is identified as node M. The gap interface is therefore identified as M+1. As previously discussed this interface is assumed to lie initially between the end faces of each fiber section and become the same interface when fiber contact is made. Both the M and M+1 fiber cells are initially set at half the axial length of the other cells. Their nodes, therefore, are at the initial free end surfaces of these cells.

The finite difference formulation of conduction heat transfer across the gap region (see Figure II-5 on the notation used to model the gap region) is approximated by:

$$\Delta Qcond_i = k_{gap}(T_{j=M+1}^{n})A_{j=M+1}^{n}\Delta T/\delta^{n} \qquad \text{(Eq. II-31)}$$

where $\Delta T = (T_{i=M}^{n+1} + T_{i=M}^{n})/2 - (T_{i=M+1}^{n+1} + T_{i=M+1}^{n})/2$

$A_{j=M+1}^{n} = \pi\{[(R_{j=M+1}^{n})left + (R_{j=M+1}^{n})right]/2\}^2$

$k_{gap}(T_{j=M+1}^{n})$ is thermal conductivity across the gap

When the gap is large, the conduction heat transfer coefficient is primarily that of the gas which is between the fiber end faces. When the gap is closed, the conduction heat transfer coefficient is primarily the "effective" thermal conductivity previously discussed. The transition between conduction heat transfer coefficients is modeled as a sum of each contribution and is given by:

$$k_{gap} = k_{gas}(\delta_{gap} - \Delta\delta_{gap})/\delta_{gap} + k_{eff}(\Delta\delta_{gap}/\delta_{gap}) \qquad \text{(Eq. II-32)}$$

where k_{gap} is the effective thermal conductivity for the gap region

k_{gas} is thermal conductivity of the gas in the gap

k_{eff} is the effective thermal conductivity of the fiber

δ_{gap} is distance across the gap

$\Delta\delta_{gap}$ is the fraction of the original gap containing fiber which has moved into the gap region due to thermal expansion and the press stroke

The gripped areas of fiber are assumed to remain at room temperature throughout the arc fusion splicing process. This assumption is justified because of the large distance between the grips and the electric discharge heating zone in addition to their relatively large mass and good thermal conduction path with other parts of the arc fusion splicer. Due to this, the conduction heat flux contribution to the energy balance from the gripped fiber sections to the two fiber cells nearest the grips (i.e., the first and the N^{th}) is given by:

$$\Delta Qcond_i = (kA/\Delta X)[T_0 - (T_i^{n+1} + T_i^n)/2] \quad \text{(Eq. II-33)}$$

where k is thermal conductivity at interface

A is fiber cross sectional area at the cell interface

ΔX is cell length

T_0 is fiber temperature at grip

$(T_i^{n+1} + T_i^n)/2$ is time averaged temperature of the adjacent i^{th} cell (i = 1 or N)

The finite difference form for conduction heat flux from the gripped fiber sections across the j=1 interface is given by:

$$\Delta Qcond_1 = 2K_{j=1}^n T_0 - (K_{j=1}^n + K_{j=2}^n)T_{i=1}^{n+1} + K_{j=2}^n T_{i=2}^{n+1} - (K_{j=1}^n + K_{j=2}^n)T_{i=1}^n + K_{j=2}^n T_{i=2}^n \quad \text{(Eq. II-34)}$$

where $K_{j=1}^n = k(T_{j=1}^n)A_{j=1}^n/(2H_{i=1}^n)$

$A_{j=1} = \pi(R_0)^2$

R_0 is initial fiber radius

The finite difference form for conduction heat flux from the gripped fiber sections across the j=N interface is given by:

$$\Delta Qcond_{N+1} = K_{j=N}^n T_{i=N-1}^{n+1} - (K_{j=N}^n + K_{j=N+1}^n)T_{i=N}^{n+1} + 2K_{j=N+1}^n T_0 + K_{j=N}^n T_{i=N-1}^n - (K_{j=N}^n + K_{j=N+1}^n)T_{i=N}^n \quad \text{(Eq. II-35)}$$

where $K_{j=N+1}^n = k(T_{j=N+1}^n)A_{j=N+1}^n/(2H_{i=N}^n)$

$A_{j=N+1} = \pi(R_0)^2$

R_0 is initial fiber radius

The complete set of finite difference equations for heat transfer to and from all fiber cells constitute N equations with N unknowns. These equations for the new time step fiber cell temperatures can be represented in a matrix formulation given by:

$$[a_{l,m}][T_{i=m}^{n+1}] = [d_l] \qquad \text{(Eq. II-36)}$$

where $l = 1$ to N

$m = 1$ to N

Here, it is noted that the elements of the matrix $[d_l]$ are computed from the cell temperatures of the previous time step. The resulting $[a_{l,m}]$ matrix is tri-diagonal.

Coefficients for the first row where $l = 1$ are given by:

$$a_{1,1} = F_{i=1}^{n} + (K_{j=1}^{n} + K_{j=2}^{n}) + C_{i=1}^{n} + E_{i=1}^{n}$$

and (Eq. II-37)

$$a_{1,2} = - K_{j=2}^{n}$$

The corresponding $[d_1]$ matrix term is given by:

$$d_1 = (F_{i=1}^{n} - K_{j=1}^{n} - K_{j=2}^{n} - C_{i=1}^{n})_{i=1}^{n} + (K_{j=2}^{n})T_{i=2}^{n} + \\ + K_{j=1}^{n}(2T_0) + C_{i=1}^{n}(2Tgas_{i=1}^{n}) + I_{i=1}^{n} \qquad \text{(Eq. II-38)}$$

It is noted that the gas temperatures, $Tgas_i^n$, do not change with each time step. These values only change when the electric discharge is turned on and off during each heating cycle. The magnitude of the gas temperature during the heating phase is determined from the glow

discharge model as described in following sections. The gas temperature during the cooling phase is assumed to be that of room temperature.

Coefficients for rows $l = 2$ to $N-1$ are given by:

$$a_{l,m-1} = -K_{j=l}^{n}$$
$$a_{l,m} = F_{i=m}^{n} + (K_{j=l}^{n} + K_{j=l+1}^{n}) + C_{i=m}^{n} + E_{i=m}^{n} \qquad \text{(Eq. II-39)}$$
$$a_{l,m+1} = -K_{j=l+1}^{n}$$

The corresponding $[d_l]$ matrix terms are given by:

$$d_l = (K_{j=l}^{n})T_{i=m-1}^{n} + (F_{i=m}^{n} - K_{j=l}^{n} - K_{j=l+1}^{n} - C_{i=m}^{n})T_{i=m}^{n}$$
$$+ (K_{j=l+1}^{n})T_{i=m+1}^{n} + C_{i=m}^{n}(2Tgas_{i=m}^{n}) + I_{i=m}^{n} \qquad \text{(Eq. II-40)}$$

Coefficients for the last row where $l = N$ are given by:

$$a_{N,N-1} = -K_{j=N}^{n}$$

and (Eq. II-41)

$$a_{N,N} = F_{i=N}^{n} + (K_{j=N}^{n} + k_{j=N+1}^{n}) + C_{i=N}^{n} + E_{i=N}^{n}$$

The corresponding $[d_N]$ matrix term is given by:

$$d_N = (K_{j=N}^{n})T_{i=N-1}^{n} + (F_{i=N}^{n} - K_{j=N}^{n} - K_{j=N+1}^{n} - C_{i=N}^{n})T_{i=N}^{n} +$$
$$+ K_{j=N+1}^{n}(2T_0) + C_{i=N}^{n}(2Tgas_{i=N}^{n}) + I_{i=N}^{n} \qquad \text{(Eq. II-42)}$$

The above set of equations are solved each time-step for the temperatures, T_i^{n+1}, along the fiber.

Initial Conditions on Temperature

The splicing process is modeled by assuming the fiber is at an initial condition of room temperature, T_0. A heating cycle consists of a heating phase and a cooling phase. At the beginning of a heating cycle, the electric discharge heat flux described in the following section is considered to be suddenly imposed along with an effective gas temperature profile along the fiber. At a prescribed time the electric discharge heat flux is considered to be turned off. Transition between the heating conditions and the cooling condition is taken as a discrete change in the heat flux to zero and the electric discharge gas temperature to T_0.

The convection heat transfer coefficient also changes from a constant value initially selected to represent nominal conditions in the electric discharge to a constant value initially selected to represent nominal conditions in the natural convection cooling of a horizontal fiber in air. These values were later adjusted by iteration to yield temperature distributions in the fiber which were in better agreement with those reported in the literature [4-56].

Cooling time-steps are continued until the maximum temperature of the fiber drops to within 100 °K of room temperature. At this point the cooling phase is considered complete and the process is halted.

Glow Discharge Heating

Heating for the arc fusion process is supplied by immersing the fiber ends in an AC glow discharge in air. The use of discharge currents on the order of milliamperes (12 - 21 mA) indicates that the label of "arc" fusion splicer is actually a misnomer. Discharges at

this current level are properly classified as "glow" discharges. Voltage and current characteristics of classical discharge types are shown in Figure II-7.

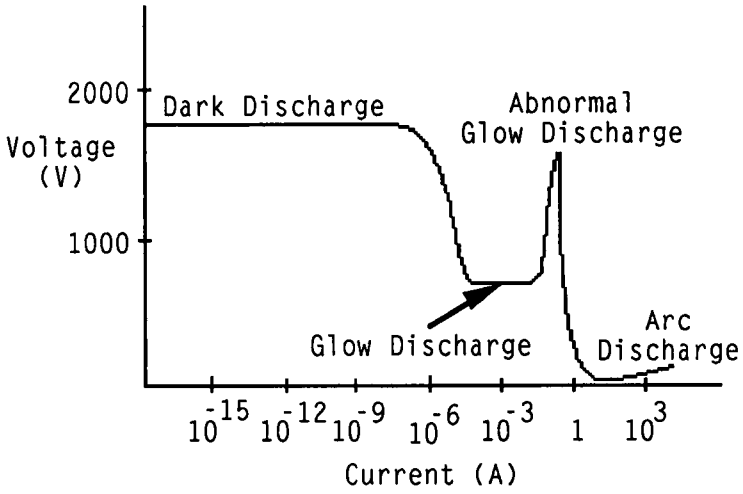

Figure II-7. Voltage and Current Characteristics of Discharge Types

Arc fusion splicing glow discharges are maintained in open air at one atmosphere of pressure and are, therefore, classified as high pressure discharges. High pressure discharges are typically characterized as maintaining local thermodynamic equilibrium conditions. This implies that all species in the discharge are at the same local equilibrium temperature. Further, it has been shown, for air discharges with a diameter on the order of a centimeter or less at pressures less than 30 atmospheres, the discharge may be considered as being optically thin such that self-absorption of radiation may be neglected [183].

Electrical power for a typical arc fusion splicer discharge is supplied by a current limited 20 kHz AC power supply. A 4 kV DC spike voltage is applied to each half cycle of the electrical field to induce breakdown to a glow discharge condition.

Previous experimental research has shown that after discharge breakdown has been initiated in air between tungsten electrodes with a 30° apex angle and electrode gap lengths in the range 0.5 mm to 2.0 mm, AC glow discharge voltage is given by the equation [10]:

$$Vg = 365 + 115(L) \qquad \text{(Eq. II-43)}$$

where Vg is glow discharge voltage

L is electrode gap length in mm

This equation yields a glow discharge voltage of 537.5 Volts for a 1.5 mm electrode gap length resulting in an effective voltage drop of 358.3 Volts/mm. This agrees very well with manufacturing specifications for arc fusion splicers [66]. It is noted that voltage between electrodes remains relatively stable over a wide range of discharge current values. This characteristic is typical of glow discharge phenomenon and has been used to produce constant voltage power supplies. It has been shown that the potential between electrodes required to maintain various currents in nitrogen at constant pressure is the same over a range of currents from 1 to 120 mA and frequencies from 0.5 to 7 MHz [184].

An AC glow discharge between pointed electrodes is axisymmetric with an additional symmetry about a central plane. Regions on each side of the central plane are like point-to-plane discharge regions where the electric field intensity increases as the electrode is approached. Typical pointed tungsten electrodes used in arc fusion splicers have electrode tip radius of 20 μm and electrode separation distances of 1.5 mm. The fiber optic filament diameter of 125 μm is less than one tenth

of the AC glow discharge region. A fiber immersed in the central region of the discharge is, therefore, far from the electrode points.

The region of the glow discharge of primary interest in this effort is the central region in which the fiber is immersed. A simplifying assumption is made that the thermal profile of the discharge is represented by black-body type emission from the heated air molecules. For black-body radiation, the temperature distribution is proportional to the 4^{th} root of the total radiation energy distribution.

Experimental measurements of broad band optical radiation from AC arc fusion splicer discharges have been converted by inverse Abel transforms into a radiation strength distribution [8]. Typical experimental optical intensity distributions are shown in Figure II-8.

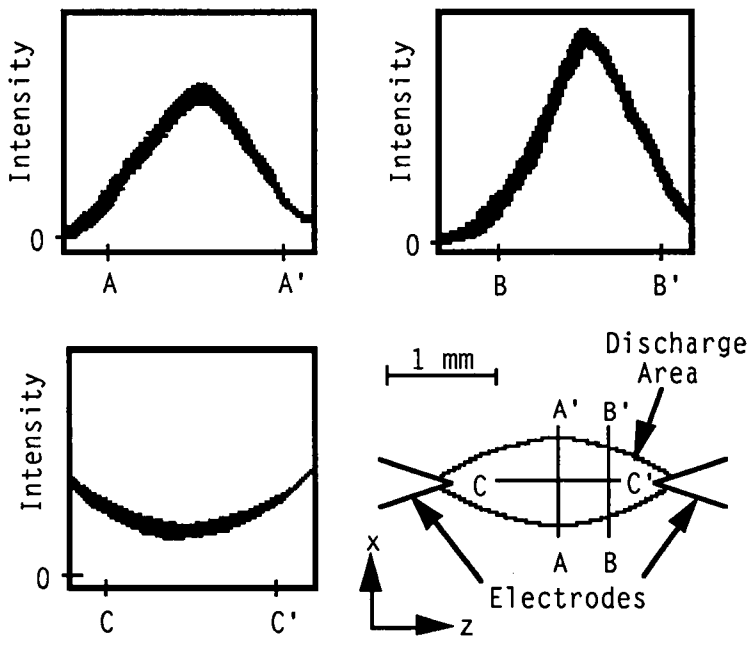

Figure II-8. Glow Discharge Optical Intensity Distributions

The optical intensity distribution is approximated well by a Gaussian distribution in the X-Y plane perpendicular to the electrode axis. Following Tachikura [8], the radiation strength from the glow discharge between electrodes is given by:

$$p(x,y,z) \propto \{1/[2\pi\sigma_p(z)^4]\}\exp\{-(x^2 + y^2)/2\sigma_p(z)^2\} \qquad \text{(Eq. II-44)}$$

where the x-y plane is perpendicular to the discharge axis

$p(x,y,z)$ is radiation strength emitted at point (x,y,z)

x,y,z is distance from center of discharge in mm

$\sigma_p(z)$ (in mm) is standard deviation of the radiation strength in the x-y plane located at z

The radiation strength was found to follow a power law relationship in the axial direction with a maximum near each electrode. Increases near each electrode are due to the increased current density and Joule heating in these regions. The standard deviation of the radiation strength as a function of z was shown to be given by [8]:

$$\sigma_p(z) = \sigma_p(0)[f(z)]^{-1/3} \qquad \text{(Eq. II-45)}$$

where $\sigma_p(z)$ is standard deviation of the radiation strength as a function of z

$\sigma_p(0)$ is $\sigma_p(z)$ at $z = 0$

$f(z)$ is variation of the radiation strength along the z axis

Under the guidance of Fujikura Ltd. (manufacturer of the arc fusion splicer used as a standard in this effort), profiles of 20 kHz

discharges were derived from reported experimental measurements [9,186]. The results are values of 1.22 mm half-width radius for the glow discharge and 1.017 mm standard deviation for the radiation strength profile in the z=0 plane. The variation of radiation strength along the z axis was approximated by a curve fit of the experimental data and is given by:

$$f(z) = 1 + 0.9345([z]_{abs})^{2.61} \qquad \text{(Eq. II-46)}$$

where $f(z)$ is variation of radiation strength along the z axis

$[\ ]_{abs}$ indicates the absolute value

z is limited between ± 0.75 mm

The proportionality constant in Eq. II-3, is related to the conversion of electrical energy into radiation and can be evaluated by considering the total power dissipated in the electrical discharge. Total electrical power dissipated in the glow discharge as radiant energy is given by:

$$P_e = V_d I_d \qquad \text{(Eq. II-47)}$$

where P_e is glow discharge electrical power

V_d is glow discharge voltage

I_d is root-mean-square (RMS) glow discharge current

The above calculation yields a value of 9.675 watts for the discharge power with a glow discharge voltage of 537.5 Volts and a RMS discharge current of 18×10^{-3} amperes. This value of discharge current

is typical of nominal arc fusion splicing conditions. Therefore, the total electrical power in the discharge is given by:

$$P_e = A \iiint p(x,y,z)\, dV \qquad \text{(Eq. II-48)}$$

where P_e is glow discharge electrical power

A is a proportionality constant

dV is differential volume element

p(x,y,z) is radiant energy released at point (x,y,z)

Numerically integrating the above equation and substituting the empirical value of 9.675 watts for the total discharge power, P_e, yields a value for A given by:

$$A = 0.6147 P_e \sigma_p(0)^4 \qquad \text{(Eq. II-49)}$$

where A is the constant of proportionality in Eq. II-48

P_e is total power in discharge (9.675 Watts)

$\sigma_p(0)$ is radiation standard deviation at z = 0 (1.017 mm)

This equation yields a value of 6.362 Watts-mm^4 for A. The radiation strength is therefore known as a function of position in the electric discharge. This value of A is for a specific electric discharge condition, in particular, specific values of the discharge geometry and power dissipation characteristics.

Normalizing the magnitude of A by the value of the electrical power yields a dimensionless heat flux distribution for the discharge. This has the advantage that the electrical voltage and current can be

input to the analytic model as variable parameters provided large excursions form the nominal values are not made. Large variations in the current and voltage characteristic of the discharge are expected to affect the discharge distribution and therefore the heat flux distribution as well as its magnitude.

It is noted that the discharge voltage has been shown to be primarily a function of the electrode separation distance. Therefore, the power dissipation characteristics of the discharge are influenced primarily by the operator's choice of discharge current and the electrode spacing fixed by the arc fusion splicer manufacturer.

Radiation from each volume element in the electric discharge to a specific fiber cell was found by computing the radiation strength from a volume element in the direction of the fiber cell, and contained in the solid angle subtended by the "visible" surface of the cell. The radiation from each volume element of the electric discharge was assumed to be isotropic. As a result, the radiation flux impinging on the surface of a cell is given by:

$$dq/dA = p(x,y,z)dVd\omega/4\pi \qquad \text{(Eq. II-50)}$$

where dq/dA is the radiation heat flux on a fiber cell surface

$p(x,y,z)$ is the radiant energy emitted by the discharge volume element

dV is the discharge differential volume

$d\omega/4\pi$ is the solid angle subtended by the exposed fiber surface

This equation is integrated over the discharge volume for each fiber cell to determine the radiation heat flux to the cell as a function of position along the x axis of the fiber. The relative geometry between an arbitrary emitting volume element in the glow discharge and an arbitrary cell of the fiber optic filament is shown in Figure II-9.

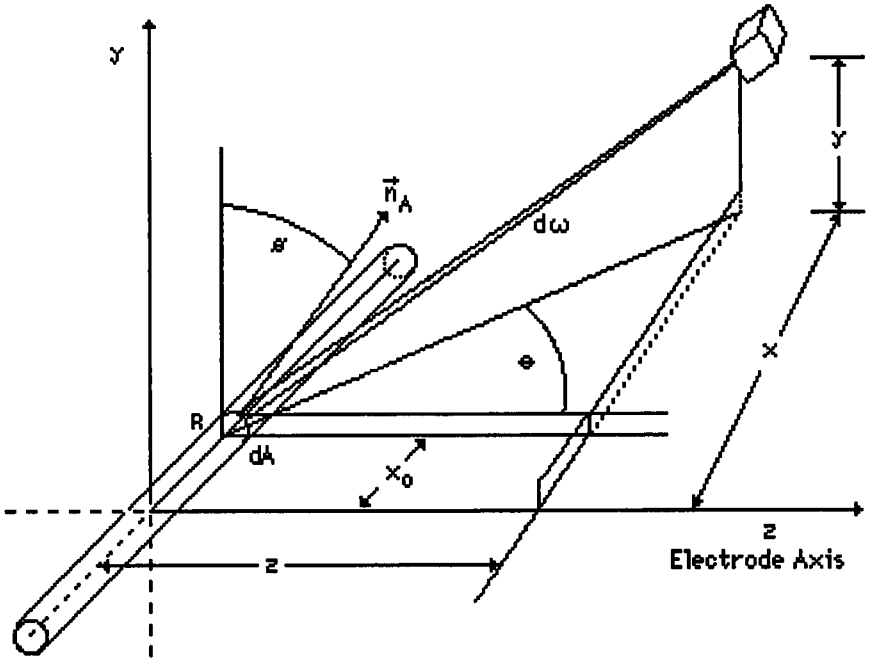

Figure II-9. Glow Discharge and Fiber Optic Filament Geometry

It is noted that the heat flux is fixed in the electric discharge coordinate system. This heat flux acts at different fiber locations as the fiber moves relative to the electric discharge during the splicing operation.

Heat flux from the electric discharge is transformed into a function of the arc fusion splicer discharge voltage and current by normalizing the radiant energy distribution by the total discharge

electrical power. This is effectively accomplished by factoring out the value of the total electrical power in the discharge from the equation for the constant of proportionality given in Eq. II-49. In this manner, the operator control variable of glow discharge current is made an input parameter of the model.

It is noted that only the discharge current is an operator-selectable variable in most commercial arc fusion splicers. The discharge voltage is related to the electrode separation distance as previously discussed. The electrode separation distance is normally fixed at the time of arc fusion splicer manufacture and is not adjustable.

The incorporation of the electrical discharge current as a parameter into the model enables this important variable to be included in parametric studies of the splicing process. It is noted, however, that this technique requires the additional assumption that the heat flux distribution in the electric discharge does not change its dimensions nor its distribution significantly as a function of electric discharge power.

The radiation flux from the glow discharge was used in the determination of an effective gas temperature used in the calculation of the heat flux due to convection heat transfer. The effective gas temperature at each fiber location was taken to be that of a black-body radiator which would produce a radiation flux equivalent to that calculated to be incident on each fiber element. The temperature distribution is, therefore, equal to the 4^{th} root of the total radiation on each fiber element divided by Stefan-Boltzmann's constant (5.67×10^{-12} watt/cm^2-°K^4).

Overview of Stress-Strain Formulation

During the arc fusion splicing process, fibers will undergo thermal, elastic, and viscous strain in response to stresses. The total strain is taken as the sum of these individual strains which is valid for small perturbations [209]. The total strain is, therefore, given by:

$$\varepsilon_T = \varepsilon_{Th} + \varepsilon_E + \varepsilon_V \qquad \text{(Eq. II-51)}$$

where ε_T is total strain

ε_{Th} is thermal strain

ε_E is the elastic strain

ε_V is viscous strain

Prior to gap closure, linear thermal expansion results in a strain characterized by fiber elongation in both the axial and radial directions. As in the case of an unrestrained press stroke, this results in movement of the fiber relative to the fixed electric discharge heat zone. After gap closure, the free expansion of the fiber is restrained in the axial direction resulting in the value of the total elongation of the fiber being equal to the initial fiber length minus the total distance of the press stroke which has occurred up to each time step. This will be discussed further in the following sections on boundary conditions. Thermal strain in the radial direction is not mechanically resisted and is treated as a free expansion.

The thermal strain is given by:

$$\varepsilon_{Th} = \alpha_{Th}\Delta T \qquad \text{(Eq. II-52)}$$

where ε_{Th} is thermal strain

α_{Th} is thermal coefficient of expansion

ΔT is the temperature change

As discussed, this thermal strain has both an axial and a radial component. The finite difference form of the axial thermal strain computed at the midpoint of the cell and is given by:

$$\varepsilon_{Thxi}^{n+1} = \alpha_{Th}(T_i^n)(T_i^{n+1} - T_i^n) \qquad \text{(Eq. II-53)}$$

where ε_{Thxi}^{n+1} is the axial thermal strain at the i^{th} node

$\alpha_{Th}(T_i^n)$ is thermal coefficient of expansion

T_i^{n+1} is temperature at the i^{th} node at the $n+1^{th}$ time step

T_i^n is temperature at the i^{th} node at the n^{th} time step

The corresponding finite difference equation for the finite difference form of the radial thermal strain is computed at the cell interface and is given by:

$$\varepsilon_{Thrj}^{n+1} = \alpha_{Th}(T_j^n)(T_j^{n+1} - T_j^n) \qquad \text{(Eq. II-54)}$$

where ε_{Thrj}^{n+1} is the radial thermal strain at the j^{th} interface

$\alpha_{Th}(T_j^n)$ is thermal coefficient of expansion

T_j^{n+1} is temperature of the j^{th} interface at $n+1^{th}$ time step

T_j^n is temperature of the j^{th} interface at n^{th} time step

When an elastic material is distorted by an applied mechanical stress, there is a coupling between strains produced in the direction of

the applied stress and strains induced in perpendicular directions. Longitudinal strains in an elastic material produce lateral strains and lateral strains produce longitudinal strains. The ratio between lateral and longitudinal strains is a constant property of the material known as its Poisson's ratio. Elastic strain contributions due to this cross coupling is given by:

$$\varepsilon_{tr} = \eta\varepsilon_{ap} \qquad \text{(Eq. II-55)}$$

where ε_{tr} is an induced strain in a direction transverse to the applied stress

ε_{ap} is the strain in the direction of applied stress

η is Poisson's ratio

Contributions from these cross coupling strains and their associated stresses must be included in calculations of elastic deformations for each fiber cell. These cross coupling stresses always resist the deformation and are therefore negative. The resulting equation for the strain in the axial direction has contributions from stresses in both the radial and tangential directions and is given by:

$$\varepsilon_X = [S_X - \eta(S_r + S_t)]/E \qquad \text{(Eq. II-56)}$$

where ε_X is the coupled axial strain

S_X is the axial stress

S_r is the radial stress

S_t is the tangential stress

η is Poisson's ratio

E is Young's elastic modulus

The tangential stress is unknown. However, the relationship between the tangential stress and the radial stress can be estimated. Because of cylindrical symmetry, the tangential strain can be expressed as:

$$\varepsilon_t = \phi dr/\phi r \qquad \text{(Eq. II-57)}$$

where ε_t is the tangential strain

$\phi dr/\phi r = dr/r = \varepsilon_r$

ε_r is the radial strain

Therefore, it is reasonable to assume that the tangential stress is proportional to the radial stress. In this case, the strain in the axial direction is given by:

$$\varepsilon_X = [S_X - \eta(1 + B)S_r]/E \qquad \text{(Eq. II-58)}$$

where ε_X is the coupled axial strain

S_X is the axial stress

S_r is the radial stress

B is the ratio between tangential and radial stress

η is Poisson's ratio

E is Young's elastic modulus

This coupled axial strain should be used for the elastic strain contribution to the total strain previously discussed. As a result the finite difference formulation of the axial elastic strain term is given by:

$$\varepsilon_{Exi}^{n+1} = [(S_{xj}^{n+1} + S_{xj+1}^{n+1})/2 - (1 + B)\eta(T_i^n)S_{ri}^{n+1}]/E(T_i^n) \qquad \text{(Eq. II-59)}$$

where ε_{Exi}^{n+1} is axial elastic strain at the i^{th} node

S_{xj}^{n+1} is axial stress at the j^{th} interface

S_{ri}^{n+1} is radial stress at the i^{th} node

B is the ratio between tangential and radial stress

$\eta(T_i^n)$ is Poisson's ratio at the i^{th} node

$E(T_i^n)$ is Young's elastic modulus at the i^{th} node

Here, it is noted that axial stress is computed at the cell interface and the radial stress is computed at the midpoint of the cell. The corresponding equation for the coupled strain in the radial direction is given by:

$$\varepsilon_r = [S_r - \eta(S_x + S_t)]/E \qquad \text{(Eq. II-60)}$$

where ε_r is the coupled radial strain

S_r is the radial stress

S_x is the axial stress

S_t is the tangential stress

η is Poisson's ratio

E is Young's elastic modulus

Expressing the tangential stress in terms of the radial stress, the finite difference formulation of the radial elastic strain term is given by:

$$\varepsilon_{Erj}^{n+1} = \{[1-B\eta(T_i^n)](S_{ri-1}^{n+1} + S_{ri}^{n+1})/2 - \eta(T_j^n)S_{xj}^{n+1}\}/E(T_i^n) \qquad \text{(Eq. II-61)}$$

where ε_{Erj}^{n+1} is the radial elastic strain at the j^{th} interface

S_{ri}^{n+1} is the radial stress at the i^{th} node

S_{xj}^{n+1} is the axial stress at the j^{th} interface

B is the ratio between tangential and radial stress

$\eta(T_i^n)$ is Poisson's ratio at the i^{th} node

$E(T_i^n)$ is Young's elastic modulus at the i^{th} node

The tangential stresses were assumed to be equal to the radial stresses, therefore, B in the above equations was set equal to 1. Stresses are discussed in the following sections on force balance considerations for fiber cells.

Stress Relationships

Stresses on the fiber result from forces due to atmospheric pressure, surface tension, and the splicing press stroke. Gravitational forces are assumed to be negligible relative to the surface tension forces as shown in Appendix B. Inertial forces are assumed negligible due to the slow flow rates [208, 209]. Key elements of stress on the fiber cells are shown in Figure II-10.

Force balances were established for the stresses in the fiber in the axial and radial directions. Axial stresses were considered uniform across each fiber cross sectional area. Radial stresses were considered uniform about each fiber cell assuming cylindrical symmetry. Values of physical properties were determined as a function of the interface

temperatures. These temperatures were linearly interpolated from temperatures calculated for the nodal positions of neighboring cells.

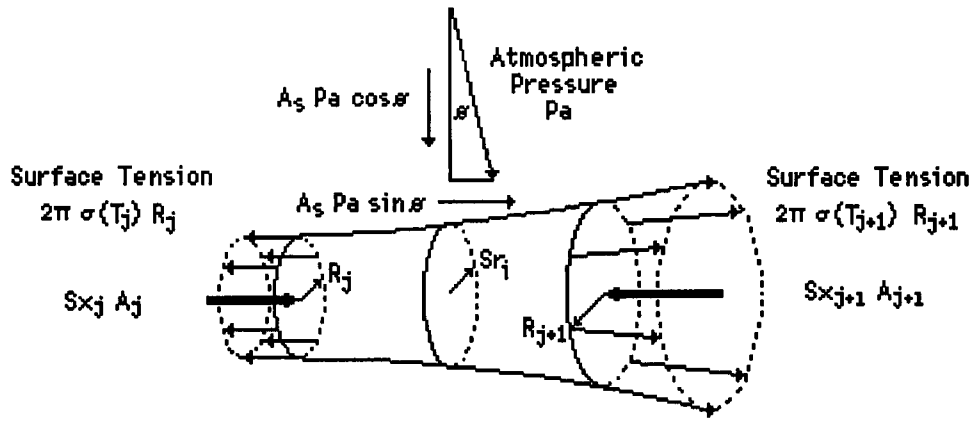

Figure II-10. Elements of Stress in Fiber Cell Force Balance

The relationship for stresses in the axial direction is developed first, then the relationship for stresses in the radial direction is developed.

Atmospheric pressure acts normal to the surface of each fiber cell. The total force due to atmospheric pressure is the result of integrating over the exposed surface area of the fiber cell. It has both an axial component and a radial component. Under conditions of cylindrical symmetry, the axial component of this force is given by:

$$Fa_X = 2\pi\int(Pa)(\sin\varnothing)r\,dx \qquad \text{(Eq. II-62)}$$

where Fa_X is the axial force due to atmospheric pressure

Pa is the ambient atmospheric pressure normal to the surface

$\varnothing = \tan^{-1} dr/dx$

This force is assumed to be applied uniformly to the area of the cell interface in the axial direction. Each cell is assumed to have a surface area approximated by that of a truncated cone as previously discussed.

The finite difference formulation for the axial component of the force due to atmospheric pressure acting on the outer surface of the cell is given by:

$$Fa_{xj+1}^{n} = PaA_i^{n}(\sin\phi_i^{n}) \qquad \text{(Eq. II-63)}$$

where Fa_{xj+1}^{n} is the axial force on the $j+1^{th}$ interface due to atmospheric pressure on the outer cell surface

Pa is the ambient atmospheric pressure normal to the surface

A_i^{n} is surface area of the i^{th} cell (see Eq. II-26)

$\phi_i^{n} = \tan^{-1} dR_i^{n}(x)/dx$

$dR_i^{n}(x)/dx$ is slope of the i^{th} cell surface

Here, the slope of the surface of the i^{th} cell, $dR_i^{n}(x)/dx$, is computed from a three point numerical differentiation formulation [182].

Surface tension generates forces along the surface of the fiber element. The axial components of these forces are directed outward from each cell and are assumed to be evenly applied at each cell interface area. This force, is directed along the surface and is, therefore, a function of the slope of the fiber surface with respect to the fiber axis.

The axial component of the force due to surface tension is given by:

$$Fs_x = 2\pi\sigma R\cos\phi \qquad \text{(Eq. II-64)}$$

where Fs_x is the axial force due to surface tension

σ is the surface tension

R is the radius of the fiber

$\phi = \tan^{-1} dR/dx$

The sign of this force is determined by the fact that it is directed outward from each end of the cell. The force outward at the left cell interface is negative and the force outward at the right cell interface is positive.

The finite difference formulation for the axial component of the force due to surface tension acting on each cell interface is, therefore, given by:

$$Fs_j = 2\pi\sigma(T_j^n)R_j^n\cos(\phi_j^n) \qquad \text{(Eq. II-65)}$$

where Fs_j is the surface tension stress at the j^{th} interface

$\sigma(T_j^n)$ is the surface tension at the j^{th} interface

R_j^n is the radius at the j^{th} interface

$\phi = \tan^{-1} dR/dx$

A balance of forces must be maintained in both the axial and radial directions. These forces can be formulated in terms of the stresses using the equations given above. When this is done, the finite difference formulation for the axial forces on each cell in terms of stresses is given by:

$$Sx_{j+1}^{n+1} = AR_j^n(Sx_j^{n+1}) - SL_{STj}^n + SR_{STj+1}^n + PA_i^n \quad \text{(Eq. II-66)}$$

where Sx_{j+1}^{n+1} is the axial stress on the $j+1^{th}$ interface

$AR_j^n = A_j^n/A_{j+1}^n$

$SL_{STj}^n = [2\pi\sigma(T_j^n)R_j^n\cos(\phi_j^n)]/A_{j+1}^n$

$SR_{STj+1}^n = [2\pi\sigma(T_{j+1}^n)R_{j+1}^n\cos(\phi_{j+1}^n)]/A_{j+1}^n$

$PA_i^n = (Pa)\sin(\phi_i^n)A_i^n/A_{j+1}^n$

$\phi_j^n = \tan^{-1} dR_j^n(x)/dx$

$dR_j^n(x)/dx$ is slope of the cell surface at the j^{th} interface

Pa is the ambient atmospheric pressure normal to the surface

$\sigma(T_j^n)$ is the surface tension at the j^{th} interface

R_j^n is the radius at the j^{th} interface

A_i^n is surface area of the i^{th} cell (see Eq. II-26)

A_{j+1}^n is the area of the $j+1^{th}$ cell interface

The relationship for stresses in the radial direction is developed in a similar manner by considering contributions from atmospheric pressure and surface tension. The radial component of the force due to atmospheric pressure acting inward on the outer surface of cell is given by:

$$Fa_r = 2\pi\int(Pa)(\cos\phi)r\,dx \quad \text{(Eq. II-67)}$$

where Fa_r is radial force due to atmospheric pressure

Pa is ambient atmospheric pressure

$\phi = \tan^{-1} dr/dx$

Again, assuming cylindrical symmetry and approximating the surface area of the cell as that of a truncated cone, the finite difference

formulation for the radial component of the force due to atmospheric pressure is approximated by:

$$Fa_{ri}^{n} = PaA_i^{n}(\cos\phi_i^{n}) \qquad \text{(Eq. II-68)}$$

where Fa_{ri}^{n} is the force inward on the i^{th} cell surface

Pa is ambient atmospheric pressure

A_i^{n} is surface area of the i^{th} cell (see Eq. II-26)

$\phi_i^{n} = \tan^{-1} dR_i^{n}(x)/dx$

$dR_i^{n}(x)/dx$ is slope of the i^{th} cell surface

Here, it is noted that the radial forces are computed for the midpoints of the cells. This makes the determination of radial forces per unit area simply a matter of dividing by each cell surface area. This results in a radial force per unit area on the cell surface area given by:

$$Fa_{ri}^{n} = Pa(\cos\phi_i^{n}) \qquad \text{(Eq. II-69)}$$

where Fa_{ri}^{n} is the radial force per unit area on the i^{th} cell surface

Pa is ambient atmospheric pressure

$\phi_i^{n} = \tan^{-1} dR_i^{n}(x)/dx$

$dR_i^{n}(x)/dx$ is slope of the i^{th} cell surface

The radial component of the force due to surface tension is the result of forces at the fiber surface which are directed about its circumference. The result of this surface force is that it tends to

constrict or "pinch" the fiber with an inward directed effective radial force per unit area [214].

The sign on the radial force due to surface tension is positive for concave surfaces and negative for convex surfaces. The radial force per unit area due to surface tension is given by:

$$Fs_r = \sigma[(1/R_x) - (1/R_r)] \qquad \text{(Eq. II-70)}$$

where Fs_r is the radial force per unit area due to surface tension

σ is the coefficient of surface tension

R_x is the surface curvature in the x-r plane

R_r is the surface curvature in the r-ø plane

The finite difference formulation for radial force per unit area due to surface tension is given by:

$$Fs_{ri}^{n} = \sigma(T_i^n)[(1/R_{xi}^n) - (1/R_{ri}^n)] \qquad \text{(Eq. II-71)}$$

where Fs_{ri}^{n} is the radial force per unit area due to surface tension at i^{th} cell surface

$\sigma(T_i^n)$ is the coefficient of surface tension

R_{xi}^n is the radius of surface curvature in the x-r plane

R_{ri}^n is the radius of surface curvature in the r-ø plane

A balance of forces in the radial direction can be formulated in terms of forces per unit area and opposing radial stresses that is given by:

$$S_{ri}^{n+1} = Fa_{ri}^{n} + Fs_{ri}^{n} \qquad \text{(Eq. II-72)}$$

where S_{ri}^{n+1} is the radial stress on the i^{th} cell

Fa_{ri}^{n} is the force per unit area due to atmospheric pressure on the i^{th} cell surface (see Eq. II-69)

Fs_{ri}^{n} is the force per unit area due to surface tension at i^{th} cell surface (see Eq. II-71)

Boundary Conditions on Stress Terms

Governing equations for the viscoelastic response of the fiber are formulated in terms of stresses and form a set of equations which can be solved as a function of time. Boundary conditions for these equations undergo transitions when the gap closes during the arc fusion splicing process. These transitions include those associated with atmospheric pressure on the fiber free ends, surface tension after fusion, and mechanical forces which are transferred from one fiber section to the other during the press stroke.

Prior to gap closure, axial forces on the end of the fiber are due to atmospheric pressure, unbalanced surface tension, and axial stress in the fiber as shown in Figure II-11.

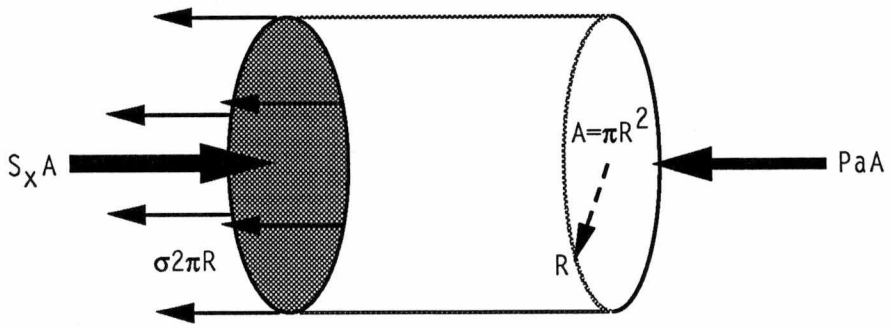

Figure II-11. Forces on Fiber Free End at Gap

A force balance at the free end of the fiber in terms of axial stress is given by:

$$S_x = - 2\sigma(\sin\phi)/R - Pa \qquad \text{(Eq. II-73)}$$

where S_x is the axial stress

σ is the coefficient of surface tension

R is the radius of the fiber end face

Pa is the ambient atmospheric pressure

Here, the cross-sectional area of the fiber end face has been divided out of both sides of the equation. This relationship is based on a force balance on an infinitesimal length at the free ends of the fibers. Therefore, the finite difference formulation for the axial stress at the gap interface is given by:

$$Sx_{j=M+1}^{n+1} = - 2\sigma(T_{i=M}^{n})(\sin\phi_{i=M}^{n})/R_{j=M+1}^{n} - Pa \qquad \text{(Eq. II-74)}$$

where $Sx_{j=M+1}^{n+1}$ is the axial stress at gap end face

$\sigma(T_{i=M}^{n})$ is the coefficient of surface tension

$\phi_{i=M}^{n} = \tan^{-1} dR_{i=M}^{n}(x)/dx$

$dR_{i=M}^{n}(x)/dx$ is slope of the M^{th} cell surface

$R_{j=M+1}^{n}$ is radius at the $M+1^{th}$ (gap) interface

Pa is ambient atmospheric pressure

The stress at all other fiber cells is determined by marching backward along the left-hand fiber section and forward along the right-hand fiber section toward the fiber grips.

After gap closure, the axial stress is due to mechanical forces which result from the press stroke. Inertial forces are assumed negligible due to the slow rates of deformation which occur. This force is transmitted along the fiber to each successive neighboring cell.

The stress in the fiber is initialized prior to beginning the stress/strain analysis. The initial axial stress is assumed constant along the fiber with a value given by Eq. II-74 evaluated with initial values of temperature, radius, and cell surface slopes of zero. The initial value of radial stress is computed from:

$$Sr_{init} = - \sigma(T_0)/R_0 - Pa \qquad \text{(Eq. II-75)}$$

where Sr_{init} is the initial radial stress

$\sigma(T_0)$ is the initial surface tension

R_0 is the initial fiber radius

Pa is the ambient atmospheric pressure

Upon gap closure the axial stress undergoes a transition characterized by free thermal and viscoelastic expansion to conditions of a known length given by the total distance between the fiber grips (L_0 - Vt). Individual fiber cells may deform according to stresses resulting on them but the sum elongation of all cells is constrained to the total length of the fiber between the two clamped ends. This length is fixed or decreases at a rate determined by the press stroke.

The press stroke performed during the arc fusion splicing operation is a constant velocity process where the starting and stopping times are adjustable parameters. The press stroke distance is equal to

the press stroke velocity times the time elapsed since the stroke movement started.

The constraint condition results in an additional equation which must be satisfied by the solution set. This constraint on the total fiber length is given by:

$$\int_0^L H_i(x)dx - v(\Delta t) = 0 \text{ (zero)} \qquad \text{(Eq. II-76)}$$

where $H_i(x)$ is the total elongated cell length

v is the press stroke velocity

Δt is the time lapsed since gap closure

L is length of fiber between clamps

Here the total axial strain includes that due to thermal, viscous, and elastic interactions including Poisson coupling terms. The finite difference formulation of the boundary condition upon gap closure is given by:

$$\Sigma_{i=1}^{N} [\varepsilon_{Thxi}^{n+1} + (\varepsilon_{Exi}^{n+1} - \varepsilon_{Exi}^{n}) + (\varepsilon_{Vxi}^{n+1} - \varepsilon_{Vxi}^{n})]H_i^n - v(t - t_0) = 0 \qquad \text{(Eq. II-77)}$$

where ε_{Thxi}^{n+1} is the axial thermal strain at the $n+1^{th}$ time step

ε_{Exi}^{n+1} is the axial elastic strain at the $n+1^{th}$ time step

ε_{Exi}^{n} is the axial elastic strain at the n^{th} time step

ε_{Vxi}^{n+1} is total axial viscous strain at the $n+1^{th}$ time step

ε_{Vxi}^{n} is total axial viscous strain at the n^{th} time step

H_i^n is length of the i^{th} cell at the n^{th} time step

v is the press stroke velocity

$(t - t_0)$ is time since gap closure

In the equation given above, elastic and viscous strains for the n^{th} time step must be subtracted because these strains are determined from absolute values and not just the change in their values since the last time step. Axial thermal strain for the n^{th} time step is not subtracted in the equation due to the manner in which thermal strains are calculated. Thermal strains at each time step are calculated from the temperature change since the last time step instead of absolute temperatures.

Viscoelastic Response of Fused Silica

Modeling of the viscoelastic characteristics of fused silica fiber material must properly simulate its elastic response to physical stress at low temperatures in addition to its viscous flow at elevated temperatures. At low temperatures, silica behaves like a nearly perfect elastic material. At temperatures above the glass transition temperature, silica behaves like a viscous Newtonian fluid. As the temperature of silica increases, its characteristics undergo a smooth transition from one type of behavior to the other. A Maxwell viscoelastic model was used to simulate both of these characteristics as a series combination of an elastic spring element and a viscous dashpot element [82].

The Maxwell model of viscoelastic response is shown in Figure II-12. Here, the elastic spring element is treated as a purely elastic Hookean material with no permanent deformation and the viscous dashpot element is treated as an incompressible viscous Newtonian fluid. This

arrangement is commonly used to represent glassy material such as fused silica [82].

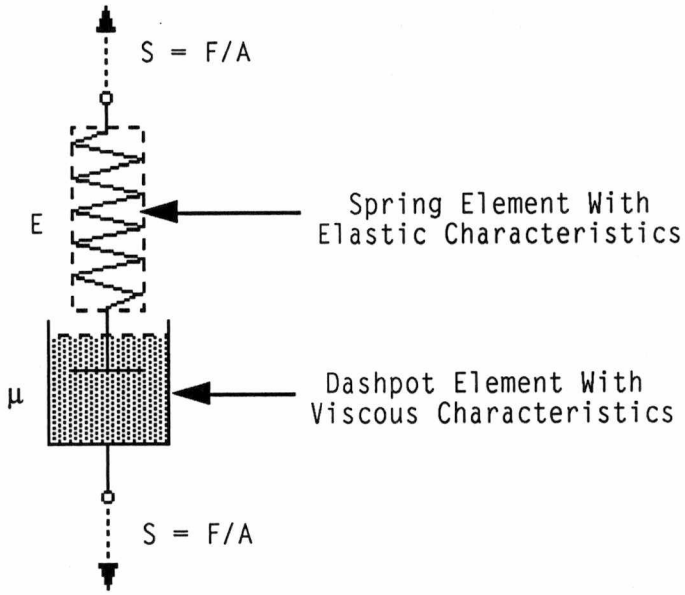

Figure II-12. Maxwell Model of Viscoelastic Response

In the Maxwell model, both elements are subjected to the same stress as given by:

$$S = F/A \qquad \text{(Eq. II-78)}$$

where S is the applied stress

F is the applied force

A is the area over which the force is applied

The characteristic response to stress of a material represented by a Maxwell model is shown graphically in Figure II-13. Here, thermal strain is absent.

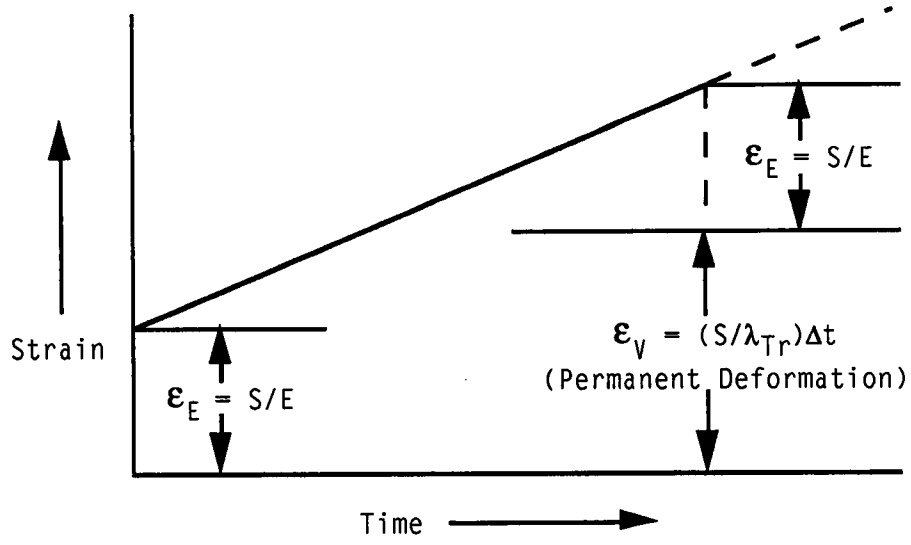

Figure II-13. Strain-Time Diagram of a Maxwell Model

The elastic strain of the elastic spring element is given by:

$$\varepsilon_E = S/E \qquad \text{(Eq. II-79)}$$

where ε_E is the elastic strain

S is the applied stress

E is Young's elastic modulus

For continuous deformation under tensile or compressive stresses, the viscous strain rate is proportional to the applied stress as given by:

$$d\varepsilon_V/dt = S/\lambda_{tr} \qquad \text{(Eq. II-80)}$$

where $d\varepsilon_V/dt$ is the rate of strain

S is the applied stress

λ_{tr} is Trouton's coefficient of viscous traction

Flow occurs in the direction of applied stress. For incompressible materials, flow also occurs in the two directions perpendicular to the axis of applied stress. Resistance to flow in each of these three directions is determined by the viscosity of the material.

The total resistance to flow is characterized by Trouton's coefficient of viscous traction, λ_{tr}. Following the above discussion, the value of Trouton's coefficient of viscous traction is typically taken to be roughly three times the value of viscosity for the material and is given by:

$$\lambda_{tr} = 3\mu \qquad \text{(Eq. II-81)}$$

where λ_{tr} is Trouton's coefficient of viscous traction

μ is the coefficient of viscosity

The total viscoelastic strain for each fiber cell is, therefore, given by:

$$\varepsilon_T = \varepsilon_{Th} + S/E + \int(S/3\mu)dt \qquad \text{(Eq. II-82)}$$

where ε_T is total strain

ε_{Th} is thermal strain

S is the applied stress

E is Young's elastic modulus

μ is the coefficient of viscosity

The terms on the right represent the thermal strain, ε_{Th}, the elastic strain, ε_E, and the viscous strain, ε_V, respectively. Where thermal strain is present, it must be added to the elastic and viscous strains to obtain the total strain.

The finite difference formulation for the axial component of the viscous strain is given by:

$$\varepsilon_{Vx_i}^{n+1} = \varepsilon_{Vx_i}^{n} + [(S_{xj}^{n+1} + S_{xj+1}^{n+1})/2][\Delta t/3\mu(T_i^n)] \quad \text{(Eq. II-83)}$$

where $\varepsilon_{Vx_i}^{n}$ is the axial viscous strain of the i^{th} cell

S_{xj}^{n} is the axial stress at the j^{th} interface

Δt is time step size

$\mu(T_i^n)$ is the coefficient of viscosity at the i^{th} node

The finite difference formulation for the radial component of the viscous strain is given by:

$$\varepsilon_{Vr_j}^{n+1} = \varepsilon_{Vr_j}^{n} + [(S_{ri}^{n+1} + S_{ri-1}^{n+1})/2][\Delta t/3\mu(T_j^n)] \quad \text{(Eq. II-84)}$$

where $\varepsilon_{Vr_j}^{n}$ is radial viscous strain at the j^{th} interface

S_{ri}^{n} is radial stress at the i^{th} node

$\mu(T_j^n)$ is the coefficient of viscosity at the j^{th} interface

Δt is time step size

Viscoelastic Strains in Terms of Stresses

The viscoelastic strains for the fiber cells can now be formulated in terms of stresses using the equations given above. The equations must be given in terms of the total of all the stresses for each cell in the fiber length between the fiber grips as given in Eq. II-77.

Introducing individual components of the total axial strain in terms of their respective stresses into this equation gives:

$$\Sigma_{j=1}^{N} \{[(S_{xj}^{n+1} + S_{xj+1}^{n+1}) - 2\eta(T_j^n)(S_{rj}^{n+1} + S_{rj+1}^{n+1})]/2E(T_j^n)$$
$$- [(S_{xj}^{n} + S_{xj+1}^{n}) - 2\eta(T_j^n)(S_{rj}^{n} + S_{rj+1}^{n})]/2E(T_j^n)$$
$$+\alpha_{Th}(T_j^n)(T_j^{n+1} - T_j^n)$$
$$+ (S_{xj}^{n+1} + S_{xj}^{n+1})\Delta t/6\mu(T_j^n)\}H_j^n$$
$$- V[(n+1)\Delta t - t_0] = 0 \text{ (zero)} \quad \text{(Eq. II-85)}$$

where S_{xj}^{n+1} is axial stress at the j^{th} interface

S_{rj}^{n+1} is radial stress at the j^{th} interface

$\eta(T_j^n)$ is Poisson's ratio

$E(T_j^n)$ is Young's elastic modulus

$\alpha_{Th}(T_j^n)$ is the thermal coefficient of expansion

$\mu(T_j^n)$ is the coefficient of viscosity

T_j^n is temperature at the j^{th} interface

H_i^n is length of the i^{th} cell

V is press stroke velocity

Δt is time step increment

t_0 is time of gap closure

Here, it is noted that the summation is over all the i^{th} cells and the use of the subscript j is for convenience in incorporating strains at the interfaces.

The above equation can be written in a somewhat simpler form by defininig a few new terms. The simplified form of this equations is given by:

$$\Sigma_{j=1}^{N} (\Gamma_j^{n+1} S_{xj}^{n+1} + \Gamma_{j+1}^{n+1} S_{xj+1}^{n+1}) H_{i=j}^{n} =$$

$$\Sigma_{j=1}^{N} [(\Psi_j^n S_{xj}^n + \Psi_{j+1}^n S_{xj+1}^n)$$

$$+ (\Omega_j^{n+1} S_{rj}^{n+1} + \Omega_j^{n+1} S_{rj+1}^{n+1}) - (\Omega_j^n S_{rj}^n + \Omega_j^n S_{rj+1}^n)$$

$$+ \Theta_j^{n+1}] H_{i=j}^n + \Lambda^{n+1} \qquad \text{(Eq. II-86)}$$

where $\Psi_j^n = 1/2E(T_j^n)$

$\Phi_j^n = \Delta t/6\mu(T_j^n)$

$\Omega_j^{n+1} = \eta(T_j^n)/E(T_j^n)$

$\Theta_j^{n+1} = \alpha_{Th}(T_j^n)(T_j^{n+1} - T_j^n)$

$\Lambda^{n+1} = [(n+1)\Delta t - t_0]$

$\Gamma_j^{n+1} = \Psi_j^n + \Phi_j^n$

and

S_{xj}^{n+1} is axial stress at the j^{th} interface

S_{rj}^{n+1} is radial stress at the j^{th} interface

$\eta(T_j^n)$ is Poisson's ratio

$E(T_j^n)$ is Young's elastic modulus

$\alpha_{Th}(T_j^n)$ is the thermal coefficient of expansion

$\mu(T_j^n)$ is the coefficient of viscosity

T_j^n is temperature at the j^{th} interface

H_i^n is length of the i^{th} cell (see Eq. II-2)

V is press stroke velocity

Δt is time step increment

t_0 is time of gap closure

The left-hand side of this equation contains the unknown stresses at each new time step. The right-hand side of the equation contains old time step values and new time step values such as those for radial strains which can be calculated independently. This equation is solved

along with the set of N force balance equations (see Eq. II-66) which must be satisfied at each cell interface.

These combined system of equations form a linear set of N+1 equations with N+1 unknowns. They may be formulated in a matrix form given by:

$$[a_{l,m}][Sx_{j=m}^{n+1}] = [B_l] \qquad \text{(Eq. II-87)}$$

where $l = 1$ to $N+1$

$m = 1$ to $N+1$

The $[a_{l,m}]$ coefficient matrix is a modified tri-diagonal matrix with a special first row. In addition, one of each of the tri-diagonal elements is always zero for the remaining rows.

The general form of the coefficient matrix with the special first row and modified tri-diagonal matrix is given by:

$$\begin{array}{cccccc}
a_{1,1} & a_{1,2} & a_{1,3} & - & a_{1,N} & a_{1,N+1} \\
a_{2,1} & a_{2,2} & 0 & - & 0 & 0 \\
0 & a_{3,2} & a_{3,3} & - & 0 & 0 \\
0 & 0 & a_{4,3} & - & 0 & 0 \\
0 & 0 & 0 & - & 0 & 0 \\
- & - & - & - & - & - \\
- & 0 & a_{N-1,N-2} & a_{N-1,N-1} & 0 & 0 \\
- & 0 & 0 & a_{N,N-1} & a_{N,N} & 0 \\
- & 0 & 0 & 0 & a_{N+1,N} & a_{N+1,N+1}
\end{array} \qquad \text{(Eq.II-88)}$$

Individual elements for the first row of the coefficient matrix, where $l = 1$, are given by:

$$a_{1,1} = \Gamma_{j=1}^{n+1} H_{i=1}^{n}$$

$$a_{1,m} = \Gamma_{j=m}^{n+1} H_{i=m-1}^{n} + \Gamma_{j=m}^{n+1} H_{i=m}^{n} \qquad \text{(Eq. II-89)}$$

$$a_{1,N+1} = \Gamma_{j=N+1}^{n+1} H_{i=N}^{n}$$

Corresponding $[B_1]$ term for the first row of the coefficient matrix is given by:

$$B_1 = \Sigma_{j=1}^{N} \{ [(\Psi_j^n S_{xj}^n + \Psi_{j+1}^n S_{xj+1}^n) + (\Omega_j^{n+1} S_{rj}^{n+1} + \Omega_j^{n+1} S_{rj+1}^{n+1}) - (\Omega_j^n S_{rj}^n + \Omega_j^n S_{rj+1}^n) + \Theta_j^{n+1}] H_{i=j}^n \} + \Lambda^{n+1} \qquad \text{(Eq. II-90)}$$

Individual elements for rows $l = 2$ to $N+1$ of the coefficient matrix are given by:

$$a_{l,l-1} = - A_{j=l-1}^n / A_{j=l}^n$$

and $\qquad \text{(Eq. II-91)}$

$$a_{l,l} = 1$$

In the above equations, individual elements of the coefficient matrix not specifically assigned a value are understood to be zero. The corresponding $[B_l]$ matrix terms for rows $l = 2$ to $N+1$ of the coefficient matrix are given by:

$$B_1 = - SL_{STj=1-1}^{n} + SR_{STj=1}^{n} + PA_{i=1-1}^{n} \qquad \text{(Eq. II-92)}$$

where $SL_{STj=1-1}^{n} = [2\pi\sigma(T_{j=1-1}^{n})R_{j=1-1}^{n}\cos(\phi_{j=1-1}^{n})]/A_{j=1}^{n}$

$SR_{STj=1}^{n} = [2\pi\sigma(T_{j=1}^{n})R_{j=1}^{n}\cos(\phi_{j=1}^{n})]/A_{j=1}^{n}$

$PA_{i=1-1}^{n} = (Pa)\sin(\phi_{i=1-1}^{n})A_{i=1-1}^{n}/A_{j=1}^{n}$

$\phi_{j=1}^{n} = \tan^{-1} dR_{j=1}^{n}(x)/dx$

$dR_j^n(x)/dx$ is slope of the cell surface at the j^{th} interface

Pa is the ambient atmospheric pressure normal to the surface

$\sigma(T_j^n)$ is the surface tension at the j^{th} interface

R_j^n is the radius at the j^{th} interface

A_i^n is surface area of the i^{th} cell (see Eq. II-26)

A_j^n is the area of the j^{th} cell interface

$i = j = 1$

The above set of equations are solved after each time-step for the stresses, Sx_j^{n+1}, at the interfaces between fiber cells. Initially the Sx_j^n stresses are taken to be equal to zero.

Allowances for axial and radial residual stresses in the fiber cells due to manufacturing processes or post manufacturing treatments may be accounted for by adding the appropriate stresses to the initial values. It is noted, however, that these parameters are generally not known.

Computation of Deformation

Changes in the fiber cell dimensions are determined from the cumulative axial and radial strains which it experiences during each time step. These strains can be determined by:

$$\Delta L = (\varepsilon_T)L \qquad \text{(Eq. II-93)}$$

where ΔL is the change in length

ε_T is the total strain

L is the previous length

The length at a new time step is, therefore, given by:

$$L^{n+1} = (1 + \varepsilon_T{}^{n+1})L^n \qquad \text{(Eq. II-94)}$$

where L^{n+1} is new length

L^n is old length

$\varepsilon_T{}^{n+1}$ is total strain

This yields a finite difference formulation for the axial length of the fiber cell that is given by:

$$H_i{}^{n+1} = H_i{}^n[1 + \varepsilon_{Thxi}{}^{n+1} + (\varepsilon_{Exi}{}^{n+1} - \varepsilon_{Exi}{}^n) + (\varepsilon_{Vxi}{}^{n+1} - \varepsilon_{Vxi}{}^n)] \qquad \text{(Eq. II-95)}$$

where $H_i{}^{n+1}$ is new axial length of the i^{th} cell

$\varepsilon_{Exi}{}^{n+1}$ is axial elastic strain of the i^{th} cell

$\varepsilon_{Thxi}{}^{n+1}$ is axial thermal strain of the i^{th} cell

$\varepsilon_{Vxi}{}^{n+1}$ is axial viscous strain of the i^{th} cell

Axial thermal strain for the n^{th} time step is not subtracted in the equation given above. As discussed for Eq. II-77, thermal strains are calculated from the temperature change since the last time step instead of absolute temperatures. Elastic and viscous strains for the $n+1^{th}$ time step are calculated from absolute stresses instead of the

change in stresses since the last time step. As a result, strain values for the nth time step must be subtracted to yield strain contributions which occurred during the $n+1^{th}$ time step.

The corresponding finite difference formulation for the radial length of the fiber cell is given by:

$$R_j^{n+1} = R_j^n[1 + \varepsilon_{Thri}^{n+1} + (\varepsilon_{Eri}^{n+1} - \varepsilon_{Eri}^{n}) + (\varepsilon_{Vri}^{n+1} - \varepsilon_{Vri}^{n})] \qquad \text{(Eq. II-96)}$$

where R_j^{n+1} is the new radius at the j^{th} interface

ε_{Eri}^{n+1} is radial elastic strain of the i^{th} cell

ε_{Thri}^{n+1} is radial thermal strain of the i^{th} cell

ε_{Vri}^{n+1} is radial viscous strain of the i^{th} cell

The above equations permit the determination of the length and radius of a fiber cell in a relatively independent manner. This method does not guarantee conservation of mass for each element. To maintain each volume element at a constant mass, a proportional adjustment is made to the lengths and radii of each cell to conserve mass.

Computational Procedure

The computational procedure follows the methodology previously discussed. The volume elements and node positions are initially defined. Axial and radial stress values are initialized as given by Eq. II-74 and Eq. II-75, respectively. The heat flux is instantaneously applied at t = 0 and calculations proceed in time increments of typically 0.01 seconds. The values of temperature at the i^{th} nodes are computed from Eq. II-36. Interface temperatures are next computed from

Eq. II-1. Axial and radial thermal strains are then determined from Eq. II-53 and Eq. II-54, respectively. Radial stresses are determined from Eq. II-72. Axial stresses are determined from Eq. II-66 before the gap closes and Eq. II-88 after the gap closes. The axial and radial stresses are then used to calculate the axial and radial elastic strains from Eq. II-59 and Eq. II-61, respectively. Axial and radial viscoelastic strains are then calculated from Eq. II-83 and Eq. II-84, respectively. These are then added to the thermal strains to arrive at the total axial and radial strains as indicated by Eq. II-82. Finally, the axial and radial fiber deformation is computed from Eq. II-95 and Eq. II-96, respectively. The process is then repeated for the next time step.

CHAPTER III

EXPERIMENTAL RESULTS AND MODEL PREDICTIONS

No analytical solutions nor experimental results for silica filaments undergoing arc fusion splicing have been reported which can be used to directly compare with predictions of the analytical model. Therefore, several experiments were performed to obtain the necessary data to provide a bases for validating the viscoelastic response predicted by the computer code.

The fiber surface contour was selected as the parameter of comparison between experimental results and model predictions. This parameter is sensitive to both thermal and viscoelastic flow characteristics in addition to the functions selected to represent the material properties. This selection was also influenced by the ability to measure the surface profile in situ with high experimental accuracy. The experiments performed and the model predictions, along with a discussion of both results, are presented in the following section.

Experimental Procedure of Continuous Fiber Tests

In the baseline experiment, an unbroken fiber was placed in the arc fusion splicer and repeatedly exposed to heating by electric discharges. Elimination of the junction region of a conventional splice simplified heat transfer and surface tension interactions. Only one gripping clamp (on the right) was used to hold the fiber. In this manner, the fiber was free to expand (toward the left) thermally without constraint. These conditions represented a case which allowed important mechanisms of thermal viscoelastic behavior to be studied without

complications of the complete gap fusion interactions and the mechanical stresses due to a press stroke. In this manner the basis of comparison between experimental and calculated results was simplified.

Under a normal arc fusion splicing operation, the surface of a fiber undergoes very little deviation from that of an unbroken fiber. Indeed, the quality of the final splice is judged relative to the lack of surface distortion. Therefore, the experiments deviated from normal splicing operations in the repeated heating of the fibers until a significant distortion of its surface resulted. The repeated heating enabled a series of photographic measurements to be taken on a sequential heating operation. This represented a technique for comparing intermediate experimental and calculated results. In addition, this technique allowed the experimental testing to continue without the fear of loss of useful data.

During the baseline experiment, a continuous fiber filament was cyclically heated with electric discharge times of 6 seconds followed by a 5 minute cooling period. The 6 second heating period is twice that of a nominal splicing operation. It was chosen after initial tests indicated that surface deformations with three second electric discharges were insignificant and therefore represented a significant source of experimental measurement inaccuracy. The 6 second electric discharge was found to be a good compromise between the desire to approximate conventional splicing conditions and the need to achieve measurable surface deformations.

The 5 minute cooling period between discharges was sufficient to insure that the fiber had returned to room temperature between each heating cycle. Experiments and analyses of the cooling rates of fiber

filaments in the fiber drawing process during manufacture indicates that the cooling time for fibers of 125 μm diameter is on the order of tens of seconds. The 5 minute cooling time insured that each fiber cooled to room temperature between each discharge. During the cooling period a 1X Polaroid photograph was taken of the fiber profile which was displayed as a 200X enlargement on the splicer TV monitor.

Electric discharge heating and ambient air cooling was repeated for the baseline case until fiber separation occurred. During the entire process the fiber remained undisturbed in the arc fusion splicer apparatus.

Apparatus and Set-Up of Fiber Distortion Experiments

All electric discharge heating experiments were performed using a Model FSM-20 arc fusion splicer manufactured by Fujikura, Ltd. This splicer is a commercial unit with an AC electric discharge created between 30 degree pointed tungsten electrodes having 20 μm radius and a 1.5 mm separation distance. All phases of the arc fusion splicing operation were performed under the control of a microprocessor to eliminate operator variations. The FSM-20 has a TV camera mounted to a 200 power microscope which monitors the fiber during electric discharge heating. The camera lens is mounted such that the view of the fiber filament was upwards at a 45 degree angle. This enabled photographic measurements to be made of the fiber by means of an oscilloscope camera after each heating cycle without removing it from the unit.

The thermal expansion (and contraction) of fused silica is on the order of 5.5×10^{-7} /C. During the cooling process from approximately 1800 C to 25 C, the heated fiber diameter of 125 μm will contract less

than 1/10 of a percent. As this is on the order of the accuracy with which the photographs were measured, these photographs which were taken at room temperature after each complete heating cycle, also tend to represent the evolution of a fiber undergoing one long continuous heating cycle.

The fiber optic filaments used in the experiments were high silica multimode fibers with a 125 μm diameter manufactured by International Telephone and Telegraph (IT&T) under their high strength military fiber program. An electric discharge RMS current value of 18 mA was selected because it represents a nominal value used during a typical arc fusion splicing operation and that for which the electric discharge heating distribution had been modeled [25, 186].

Fiber optic filaments are held in place by a combination of "V" blocks, centering wedges, and gripping clamps on the arc fusion splicer. Each "V" block maintains axial alignment of the fiber relative to the electric discharge electrodes and with the other "V" block. The "V" blocks are located a distance of 3.25 mm from the electrode axis. Each centering wedge is arranged such that it insures the fiber remains securely seated in the trough of its "V" block without constraining its axial movement. They are located a distance of 6.5 mm from the electrode axis. Axial fiber motion relative to the "V" blocks is prevented by the gripping clamps located 14.25 mm from the electrode axis.

Results of Continuous Fiber Tests

Experimental results for the continuous fiber experiment are shown as a series of figures. These figures are derived from photographs

which show the progressive deformation of the continuous fiber over 10 consecutive 3 second heating and 5 minute cooling cycles. Each photograph was processed by line scanning the image into a computer data base and performing image processing to adjust the brightness and contrast.

A typical image is shown in Figure III-1 with labels added to indicate various features. The outer edge of the dark bands represents the physical boundary of the fiber profile. The line drawn vertically through the center of the figure represents the electrode axis and the center of the electric discharge heating zone. A bright band is typically seen in the center of each fiber. This band is a result of light refraction through the fiber and does not represent any physical boundary nor does it indicate the exact location of the fiber core.

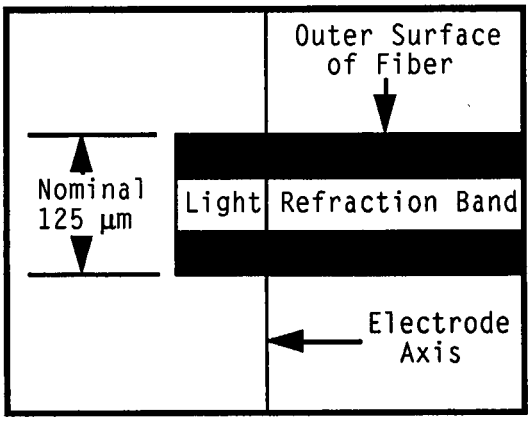

Figure II-1. Features of Experimental Results

Experimental results for the continuous fiber experiment are shown in Figure III-2 through Figure III-11.

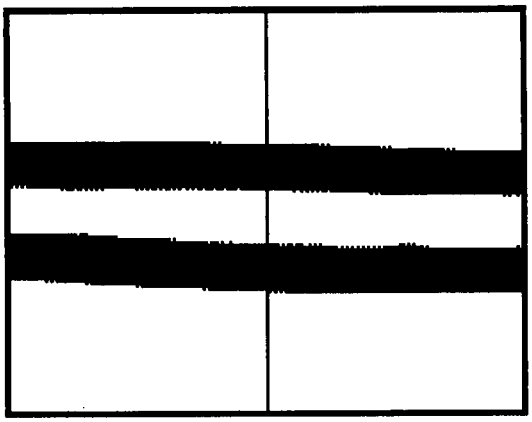

Figure III-2. Continuous Fiber Profile After 1 Heating Cycle

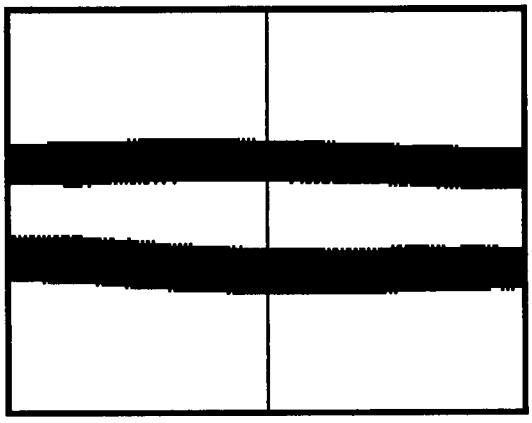

Figure III-3. Continuous Fiber Profile After 2 Heating Cycles

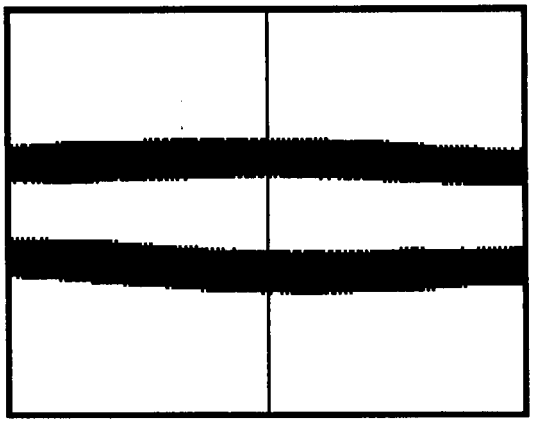

Figure III-4. Continuous Fiber Profile After 3 Heating Cycles

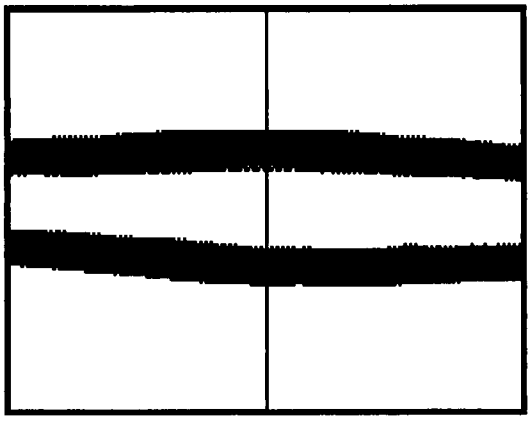

Figure III-5. Continuous Fiber Profile After 4 Heating Cycles

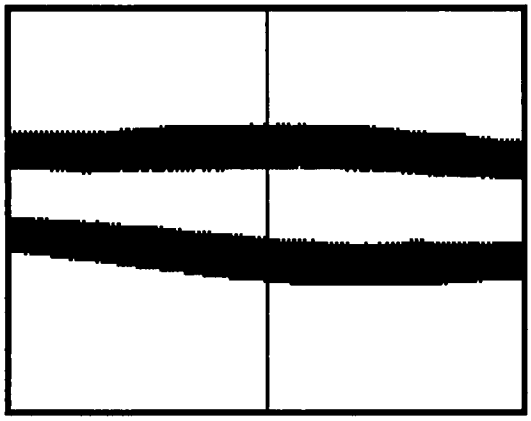

Figure III-6. Continuous Fiber Profile After 5 Heating Cycles

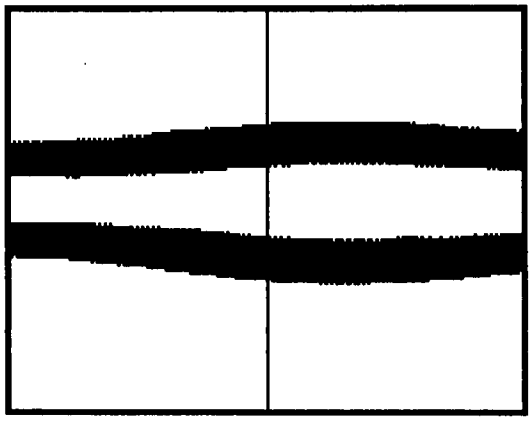

Figure III-7. Continuous Fiber Profile After 6 Heating Cycles

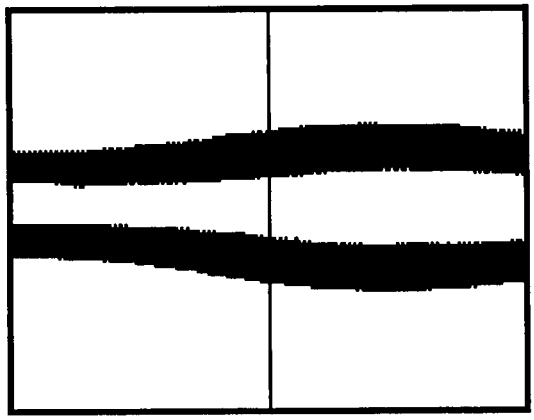

Figure III-8. Continuous Fiber Profile After 7 Heating Cycles

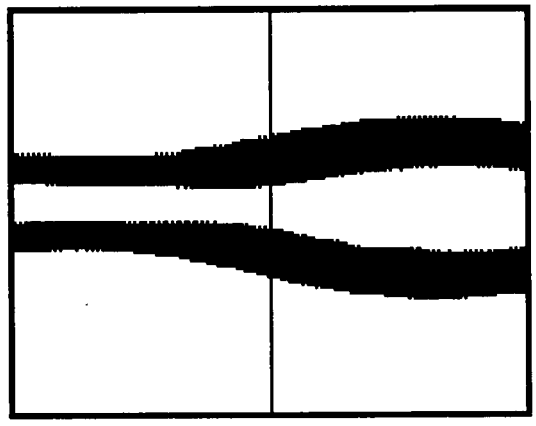

Figure III-9. Continuous Fiber Profile After 8 Heating Cycles

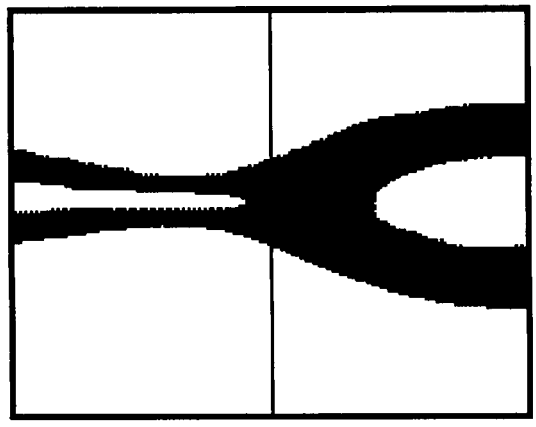

Figure III-10. Continuous Fiber Profile After 9 Heating Cycles

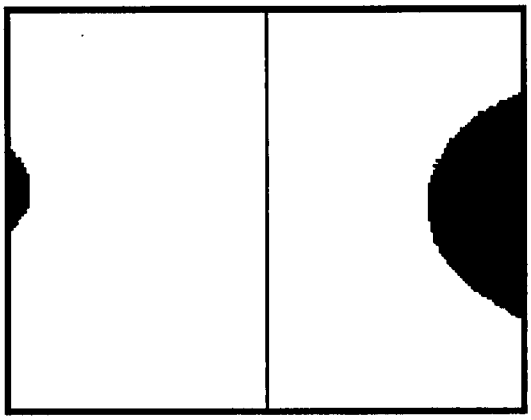

Figure III-11. Continuous Fiber Profile After 10 Heating Cycles

In Figure III-2 through Figure III-5, the fiber can be seen to be slightly bulging near the center of the discharge. Not visible to the unaided eye but measurable under magnification, the left side of the fiber has a slight necking down region. In Figure III-6 through Figure III-8, the shrinking of the left-hand side of the fiber becomes much more pronounced. Also shown in these figures, the center bulge continues to grow with the high point shifting toward the right-hand side of the fiber. In Figure III-9 and Figure III-10, a very strong necking down of the fiber occurs approximately one fiber diameter from the center of the discharge. Finally, in Figure III-11, the fiber separates and the two molten ends are rapidly pulled away from the center of the discharge by surface tension and/or internal stresses.

Several features of the evolution of the fiber surface during electric discharge heating can be observed by an examination of the figures. The fiber surface distortion is symmetrical with respect to its center-line. No effects of gravity (for example, fiber drooping) are apparent. Spot checks of the distortion in an orthogonal plane

confirmed that the surface distortion was axisymmetric with no gravitational effects apparent.

In Figure III-12 and Figure III-13, the final profiles of the of the separated fiber ends are shown. The left-hand side, shown in Figure III-12, has a symmetric rounding of the end with no pronounced growth in its diameter. The right-hand side, shown in Figure III-13, has a pronounced, almost elliptic bulge on its end.

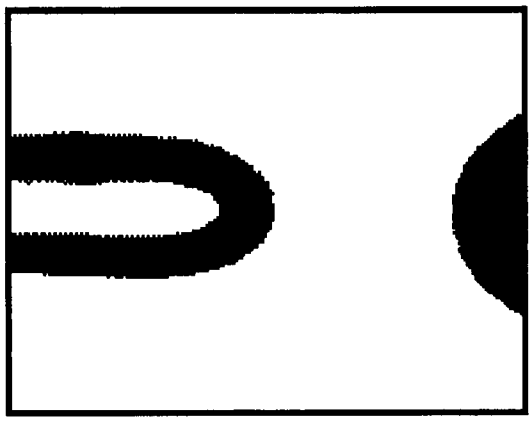

Figure III-12. Final Left Fiber End Profile After Separation

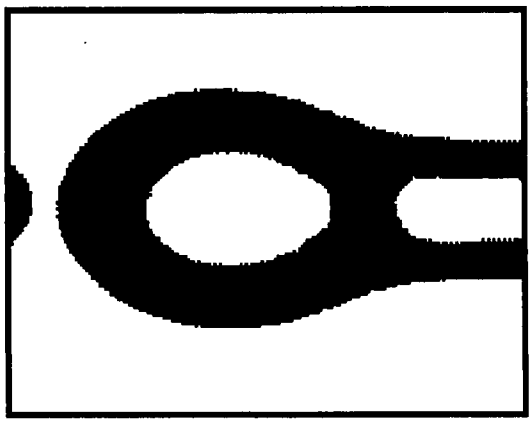

Figure III-13. Final Right Fiber End Profile After Separation

It is apparent from the figures that the fiber surface evolves unsymmetrically with respect to the electrode axis and the center of the discharge heating. This was confirmed over several trials and at different arc fusion splicer parameter settings. Not only was the shape similar in each case, but the orientation with regard to left and right was the same. That is, the right side of the heated region always increased in diameter while the left side decreased. It is noted that, the right side of the fiber filament is held fixed relative to the splicer while the left side of the fiber is unclamped and, therefore, free to move in the axial direction.

It is believed that the initial disturbance of the fiber surface is such that the left-right preference of resulting shape results. The fiber expands slightly to the left as it is heated because of the constraint placed on motion by the clamp located on the right side. This relative motion is equivalent to sweeping the heating zone over the fiber from left to right. A result of the relative motion is that a larger section of the fiber to the right of the heating zone expands into the higher temperature central region than the fiber to the left of the zone. This higher temperature affects the fiber material properties, in particular, the surface tension and viscosity.

A dominant force on the fiber material is its surface tension which for silica decreases slightly with increasing temperature. During a heating cycle, the temperature in the fiber increases and the surface tension decreases. A decrease in the surface tension results in a shift in the relative magnitudes of radial and axial stresses governing viscoelastic flow. If the axial stresses exceeds the radial stresses, the fiber will tend to bulge under strong viscous strain. On the other

hand, if the radial stresses dominate the axial stresses, pronounced necking down during the viscous deformation will occur.

As the fiber expands toward the left and the higher temperature region shifts toward the right, the radial stresses due to surface tension are less on the right side than on the left side. The observable effect of this interaction is a necking down of fiber material on the left side and a bulging of fiber material on the right side.

As shown in the figures, the degree of surface distortion due to each subsequent heating cycle increases in a uniform manner. No oscillations in the surface geometry were ever seen. There was a dramatic increase in the rate of the surface distortion with each subsequent discharge heating cycle.

Repeated experiments gave similar results as can be seen in Figure III-14. The evolution of the surface always followed the same pattern. Only the stage of evolution "captured" in each photograph was different in the trials. The surface contour has been shown to evolve into an unsymmetrical surface similar to those reported for free surface cylindrically symmetrical fluids [200]. In these studies, the time to breakage has been shown to be very sensitive to the magnitude of the initial perturbation. In addition, during the later stages of evolution toward breakage, the surface changes very rapidly. It is believed that, in the experiments, initial perturbations and experimental variations were sufficiently different to account for the differences seen in the surface profiles frozen when the discharge heating was stopped.

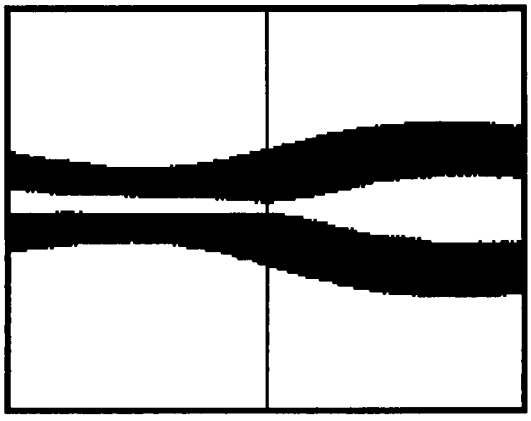

Figure III-14. Repeat Experimental Results for 6 Second Heating Cycles

Model Predictions and Comparison with Experimental Results

The analytical model of the arc fusion splicing process was run for conditions of the continuous fiber experiment. Application of the model to the experimental conditions of the continuous fiber experiment was made by positioning the gap region outside the heating zone and assuming a large value for the gap to allow the fiber to expand without restriction. A no press-stroke condition was input to the model. In this manner, the experimental conditions of a continuous fiber free to expand on one end was simulated.

Initial predictions of the arc fusion splicing analytical model using the model previously described above for the electric discharge heating yielded unacceptable results. The resulting fiber temperatures did not have distributions in agreement with reported temperature profiles and did not appear to correspond to the experimental results. Because of this, the electric discharge model was replaced with a Gaussian distribution for convenience.

The parameters of the Gaussian distribution were chosen such that the heat flux along the fiber follows that of the optical intensity distributions of Figure II-8. The conversion of total electrical power into thermal power has been estimated to be 10 percent efficient [10]. This heat flux distribution yielded satisfactory results.

It is believed that the primary discrepancy in the electric discharge heating model is related to the assumption of it being a black-body radiator with no allowance made for selective band radiations. Moreover it is assumed that the total input power is completely converted to thermal radiation which is not likely. This model is believed to be physically correct but additional research is required to fully determine the correct values of the parameters entered into the model. In addition, the assumption of a constant value for the convection heat transfer in the discharge is suspect but no functional dependence on position has been reported for the conditions at the fiber surface in an electric glow discharge.

A predicted profile corresponding to each photograph of the experimental results shown previously in Figure III-2 through Figure III-11 was obtained with the model. Comparisons between the analytical model predictions and the experimental results of the fiber surface evolution were made using measurements directly from the original photographs. The analytical data were compared with the experimental data by scaling the results and preparing overlying plots. This is shown in Figure III-15 and Figure III-16 for the results obtained after 3 and 5 heating and cooling cycles, respectively. As shown, the analytical model predicts the fiber deformation shape very well including its asymmetric nature but tends to over predict the magnitude.

Quantitative data was obtained from each experimental photograph by tracing along its upper surface using a graphic digitizing pad. The digitized data consisted of values of the fiber radius at given positions along the fiber length. The X axis of the digitized data coordinate system was located along the center-line of the fiber and the Y axis was located along the center-line of the electric discharge electrodes.

The center-line of the fiber from which the radius was measured was scaled with a vernier caliper and manually marked on each photograph. The center-line was measured at several locations along the fibers length. No asymmetry was detected in the fiber profile, therefore only the upper radius was digitized. The center-line of the electric discharge electrodes was determined by manually adjusting the TV camera until the electrodes were visible and marking the center-line on the monitor screen. This center-line was marked on the TV screen and was present in the upper portion of each photograph taken. A scale factor for the data was determined by using the unheated fiber 125 μm diameter as a calibration reference.

Analytical results obtained for later stages of the fiber profile evolution as it approached separation did not agree very well with the experimental results. It is believed that the deviations are cumulative in subsequent cycles and tend to increase in the degree of deviation with each heating cycle as the rate of changes increase. Several parameters whose values are not known with accuracy were examined in a sensitivity analysis to determine their potential impact on the results.

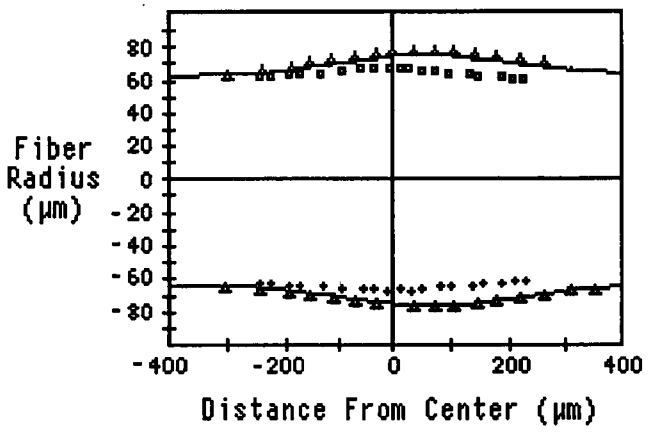

Figure III-15. Analytical and Experimental Results for 3 Heating Cycles

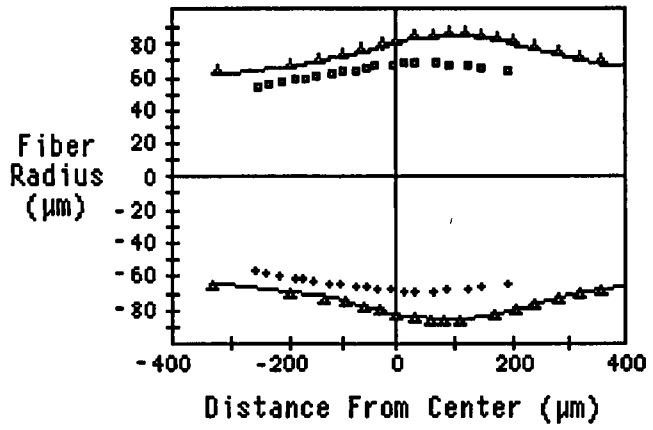

Figure III-16. Analytical and Experimental Results for 5 Heating Cycles

It was found that the computed magnitude of the deformation and maximum fiber temperatures are very sensitive to the magnitude of the heat transfer coefficient between the electrically heated air and the fiber surface. For the results shown in Figure III-15 and Figure III-16, the heat transfer coefficient is h = 3.575 X 10^{-2} Watts/cm^2 (100 Btu/hr ft^2). In Figure III-17, a sequence of 6 fiber profiles are shown for analytical calculations corresponding to heating and cooling cycles

with a heat transfer coefficient of h = 7.15 X 10^{-2} Watts/cm^2 (200 Btu/hr ft^2).

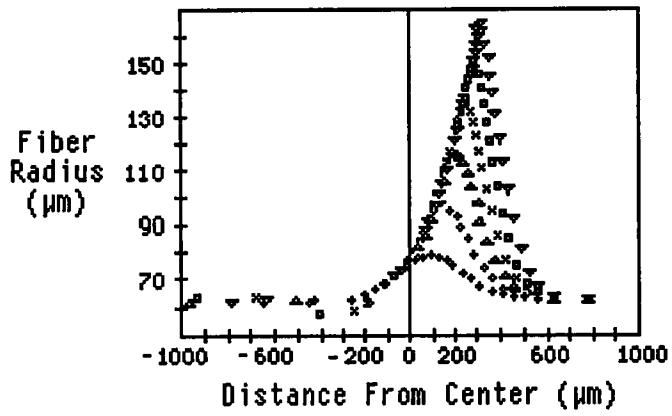

Figure III-17. Profile with an Increased Heat Transfer Coefficient

When compared to experimental results, the fiber profiles in Figure III-17 shows the necking down characteristic similar to that shown to occur experimentally. Magnitudes of the necking down region on the left-hand side is under-predicted in these calculations and the magnitude of the bulge on the right-hand side is over-predicted. In addition, the curvature of the bulge peak is calculated to be greater than that found experimentally.

An important result of the analysis is that the primary heating mechanism has been shown to be convective heat transfer. In addition, the peak temperatures at the fiber bulge were found to increase in magnitude by 22 °C with each sequential heating and cooling cycle. It is believed that the phenomenon of a sequential increase in the fiber temperature profile is also related to an increase in the heat transfer due to a sequential increases in the fiber surface area with each heating cycle. This creates a larger surface area for convective heat

transfer to take place. The temperature difference between sequential peak temperatures is not sufficient to indicate fundamental differences in the deformation process.

Another potential explanation for the differences shown between the analytical and experimental results can be found in the assumption that one end of the fiber was free to move without resistance. This was relatively easy to simulate in the model but may not have been entirely implemented experimentally due to frictional forces. One end of the fiber lay freely in V alignment grooves held only by its own weight. There was, therefore, a small axial frictional force resisting the movement of the fiber.

The model shows that surface tension forces in the discharge heating zone tends to move fiber material toward the cooler regions on the side of the gripped fiber end. With no resistance to axial motion assumed, the model allowed cool fiber material on the free end of the heating zone to move freely with the heated material in the heating zone. As a result the model shows less necking down on the free end side of the heating zone and a larger radial growth toward the gripped end than found experimentally. It is noted, that in a conventional arc fusion splicing process, both ends of the fiber are gripped and it is not important to allow for frictional effects.

Additional Experimental Results and Model Predictions

The dominant effect of the surface tension on the evolution of the fiber profile was demonstrated by a couple of additional experiments performed. The first additional experiment consisted of heating a single cleaved fiber end in the electric discharge heat zone. In this

experiment, the flat face of the fiber end was aligned with the axis of the electrodes as shown in Figure III-18. As can be seen, the fiber end face was cleaved perpendicular to the its axis.

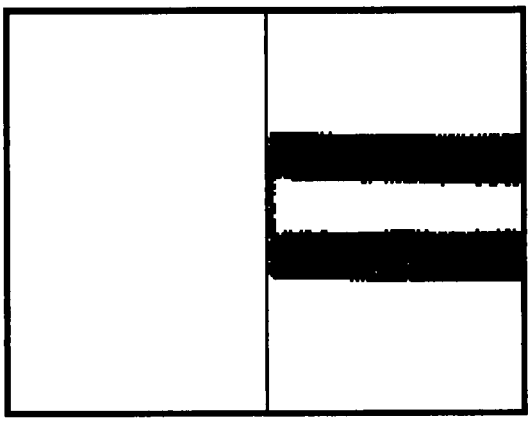

Figure III-18. Free End Alignment Prior to Discharge Heating

When heated with a three second discharge, the fiber was found to respond immediately. A three second electric discharge resulted in the formation of a rounded bead on the fiber free end and a flowing of molten material back along the fiber axis until it moved out of the center of the heat zone. This retraction placed the end of the fiber (the furthermost projection of the formed bead) near the edge of the TV monitor screen. The profile of the bead on the free end was photographed by manually moving the fiber end back into view. The profile of the free end in position for a repeat discharge is shown in Figure III-19

As an extension of this experiment, the widest portion of the bead on the end of the fiber was manually realigned with the electrode axis and an additional three second electric discharge applied. The cooling time between discharges was approximately 5 minutes. Again, the

response was an immediate retraction of the end of the fiber along with a simultaneous growth in the size of the bead on the end of the fiber. The resulting fiber profile following two sequential heating cycles is shown in Figure III-20. The corresponding profile following three sequential heating cycles is shown in Figure III-21. In each of these figures, the bead has been recentered with the electrode axis.

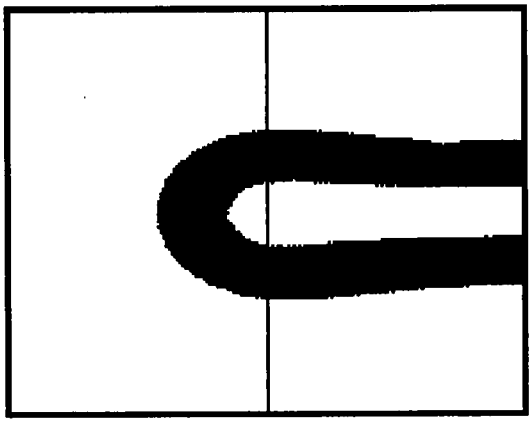

Figure III-19. Free End Profile After 1 Heating Cycle

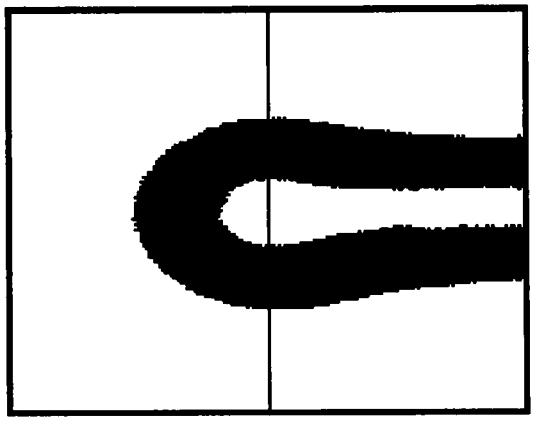

Figure III-20. Free End Profile After 2 Heating Cycles

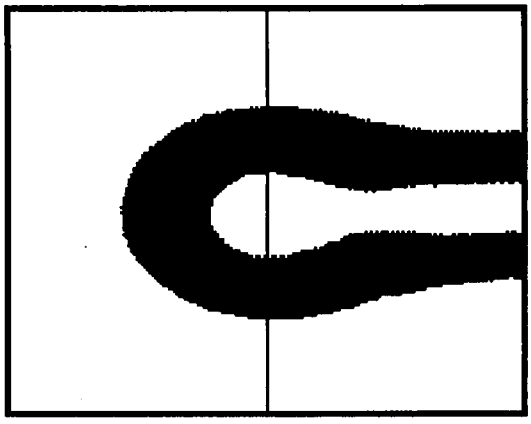

Figure III-21. Free End Profile After 3 Heating Cycles

As shown, the end of the fiber assumes a near elliptical profile similar to that found in the continuous fiber experiment after fiber separation occurred. As the size of the bead size grew with each additional heating cycle, the retraction of material along the axis of the fiber became less dramatic. This is shown in Figure III-22 which shows the location of the bead following the fourth heating cycle.

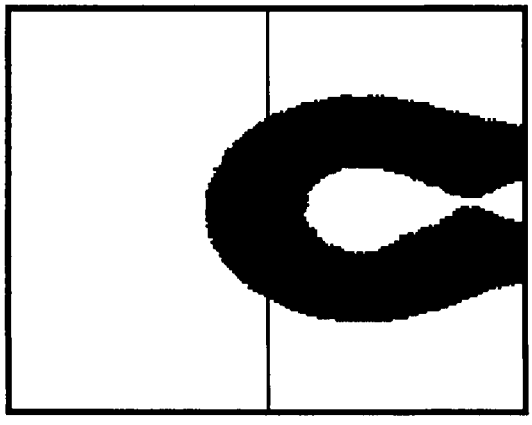

Figure III-22. Free End Profile After 4 Heating Cycles

The process of recentering the bead on the end of the fiber with the electrode axis was repeated for a total of ten, 3 second heating cycles with a 5 minute cooling period between each cycle. Figure III-23 shows the final results. The series of heating cycles was halted after the tenth cycle because it was believed that the width of the bead had grown to the point that it was interacting with the electrodes. Later inspection showed that an apparent defect in the surface of the bead region was in fact an illusion resulting from refraction of illuminating light into the camera lens.

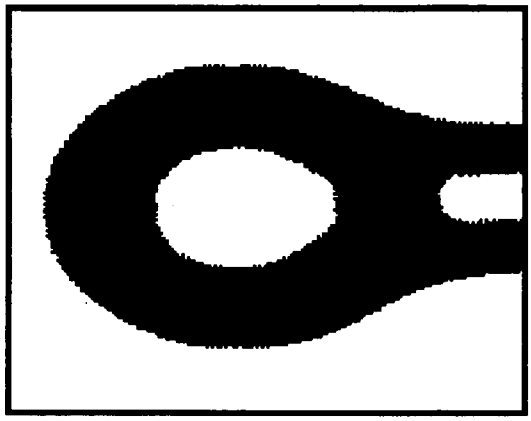

Figure III-23. Free End Profile After 10 Heating Cycles

Of all the experiments performed, only extremely large beads of silica formed after many heating cycles gave any evidence of gravitational effects. The center of the bead shown in Figure III-23 which was formed after 10 heating cycles is just slightly below the center-line of the fiber.

The analytical model of the arc fusion splicing process was run for conditions of the free end fiber experiment. Application of the model to the experimental conditions of the continuous fiber experiment

was made by positioning a large gap inside the heating zone but offset slightly to one side. This offset initially positioned the fiber free end at the center of the heating zone. As in the case of the continuous fiber analysis, a no press-stroke condition was input to the model. Here the heating cycle was reduced to 3 seconds to correspond with the experimental conditions. At the end of each heating cycle the free end of the fiber was analytically repositioned in the center of the heating zone.

A fiber profile for the free end case following two heating cycles was predicted with the model. The analytical data is shown in Figure III-24.

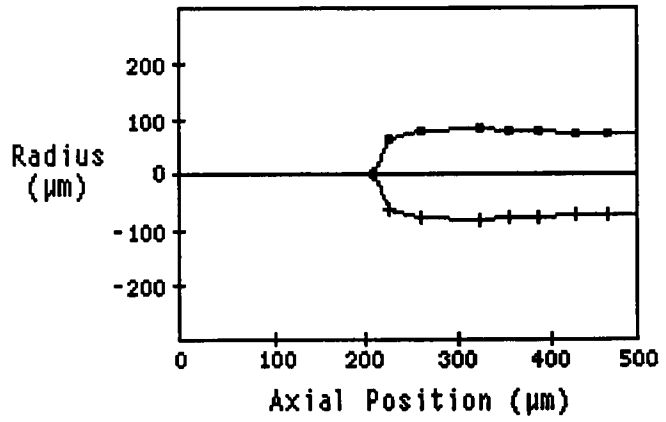

Figure III-24. Free End Analytical Results

As shown, the analytical model predicts the rounding of the fiber end and its increase in size but tends to under-predict its magnitude. It is believed that the experimental conditions for this case did not truly have frictionless axial movement and is believed partly responsible for the magnitude differences observed. Another factor is

the presence of an initial sharp corner on the cleaved fiber which leads to very large surface tension forces in that area. One possible solution for this is to decrease the grid spacing used to model the end region. Another possible solution is to expand the model into a two dimensional treatment to allow the fluid flow to be different across the fiber end face.

Because of the rapid retraction found in the free end experiment, a second additional experiment was performed to determine the impact that the free end exposure has on the heat transfer to the fiber and on its profile evolution. This experiment used the procedure and set-up of the continuous fiber baseline experiment except that a cleaved fiber was used. Two fibers with perpendicular faces were butted together at the center-line of the electrode axis as shown in Figure III-25.

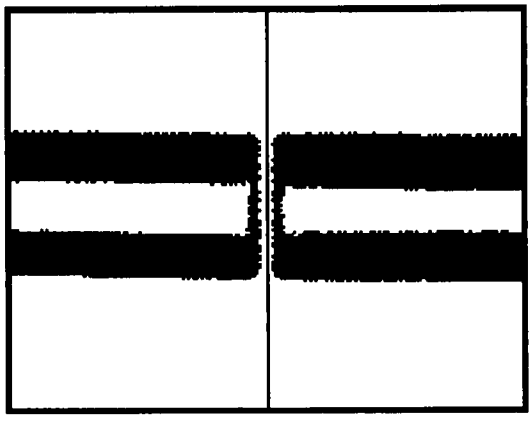

Figure III-25. Position of Fibers in Experiment With No Press Stroke

Each fiber initially shielded the other fiber end face from direct exposure to the electric discharge radiation and from convection heat transfer with heated gas. Being located at a point of symmetry in the

heat zone allowed conduction heat transfer along the fiber axis to be ignored. The experimental results are shown in Figure III-26.

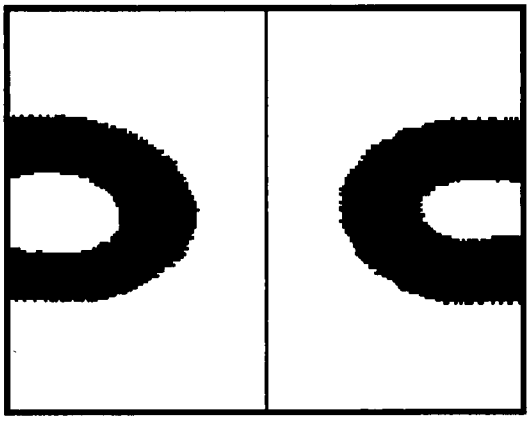

Figure III-26. Results of Heating Two Fibers With No Press Stroke

As in the case for the free end experiments, even when the discharge time was reduced to three seconds, the fiber responds to discharge heating was immediate separation of the ends by the formation of an enlarged bead on the fiber ends. This demonstrates that the results obtained with the free end experiment are not primarily the result of heat transfer differences between the experiments.

It is believed that the experimental results for the case of two fiber ends butted together but with no press stroke can be explained by a consideration of the surface tension forces. At a free end the primary surface tension forces are directed toward one side along the fiber axis. Additional surface tension forces are present in the fiber end face which are perpendicular to the fiber axis. During viscoelastic flow at a fiber end face, the combined effect of these surface tension forces tends to result in the rounding of the fiber end face.

It is noted that the results obtained with no press stroke illustrate the importance of this step in performing a conventional arc fusion splicing operation. The press stroke is necessary to insure fusion of the end faces during the melting process and assist in the formation of surface tension forces bridging the interface region.

CHAPTER IV

DISCUSSION OF RESULTS

Results from both laboratory experiments and analytical model calculations provide insight on the fidelity of the model and its utility in analyzing the arc fusion splicing process. These results along with their implications are discussed in the following sections.

Fidelity of Analytical Model

The analytical model has been shown to correctly describe the primary physical process taking place in arc fusion splicing of high silica fiber optic filaments. For a continuous section of fiber heated cyclically in a conventional arc fusion splicer, the analytical model shows the bulging and necking down of the fiber element as observed experimentally. It also correctly displays the general viscoelastic flow characteristics experimentally observed in the fiber surface contour evolution for a continuous fiber when heated until separation occurs. This agreement with experimental results includes the development of an asymmetry in the surface contour.

The model accurately predicted the evolution of the fiber surface into an asymmetric form. Results of the continuous fiber experiments showed a consistency in the orientation of the necked down region toward the left side of the discharge heated zone.

Analysis of the necking down phenomenon using the model as a basis has helped in providing an explanation for the consistency in the orientation of the necked down region. The left side of the fiber was not gripped during the experiment. As a result, the fiber was free to

expand toward the left side during thermal expansion. Expansion of the fiber toward the left had the effect of sweeping the heat zone from the left to the right as the fiber temperature increased. This in turn provided a situation in which fiber material to the left was at a slightly higher temperature than fiber material toward the right at any instant in the expansion process. A result of this was that the surface tension was slightly less on the left side of the heat zone which resulted in moving the fiber material toward the right inducing a necking down region toward the left side.

The existence of a necking down tendency clearly explains the experimentally observed requirement for a press stroke to insure good fiber fusion with a minimum loss of physical and optical properties. The press stroke adds material to the region and counters the necking down tendency. This in turn, maintains the cross-sectional area of the fiber and, thereby, avoids a loss in its ultimate strength.

Because the tensile strength of the fiber is typically calculated based on the a nominal cross-sectional area and not on an actual cross-sectional area, the decrease in ultimate strength is interpreted as a lowering of tensile strength. The experimentally observed phenomenon in which arc fusion splicing lowers the tensile strength of fibers may partially be explained in this manner.

A similar argument can be made for optical loss considerations. A small bulge in the optical waveguide is not sufficient in physical extent to permit optical mode mixing and therefore the light effectively "shoots across" the bulge region. A necking down in the waveguide, on the other hand, immediately degrades the optical path. A result is that optical considerations favor a bulge over a necking down region. This

helps explain the experimentally observed phenomenon in which optical losses tend to be less with the use of a press stoke during arc fusion splicing.

It is noted that an optimum press stroke from ultimate strength considerations may not be the same as that optimized from optical loss considerations. In fact, a trade-off is anticipated.

In the present version of the model, magnitudes of profile distortion are not predicted with great accuracy. In addition, model predictions for the later stages of profile development, near the time of fiber separation, deviate from experimental results. These inaccuracies are believed to be related to the following: 1) uncertainty in the heat flux model and heat transfer coefficient along the fiber immersed in a glow discharge, 2) resolution of the numerical algorithm due to the use of a one dimensional finite differencing grid along the fiber axis, 3) lack of accurate physical property data as a function of temperature, and 4) the fact that silica fiber optic filaments contain radial gradients of index of refraction dopants and have significant nonuniform residual stresses due to their draw tower air-quench manufacturing process.

A detailed knowledge of the exact glow discharge heat flux profile for the experimental arc fusion splicer is not known. This information was derived form information which has been published in the open literature and is based on generic arc fusion splicer measurements. As a result the accuracy with which the model predicts specific arc fusion splicer results appears to be limited to the degree that the actual glow discharge heat source complies with the published information.

Analysis of results of the analytical model shows the sensitivity to details of the heating conditions which exist within the glow discharge. In particular, the magnitude of the heat transfer coefficient has been shown to have a profound effect on the evolution of the fiber surface deformation. This suggests that, in addition to the geometrical relationship between the heat profile of the glow discharge and the fiber, gas composition, its circulation within the discharge, and ambient conditions such as atmospheric pressure, and humidity may be important variables in the arc fusion process.

A comparison of experimental and analytical results show the greatest discrepancy occurs when the curvature of the fiber surface is great. This is the case for the free end experiments and when the continuous fiber experiment approached fiber separation. This suggests that stress gradients across the fiber cross-sectional areas may become significant. Accurately modeling this situation requires expansion of the finite differencing grid used in the model to two dimensions. This would enable the simulation of the viscoelastic response within a cross-sectional area of the fiber to be treated as non-uniform.

A wide range of temperatures are experienced by a fiber during arc fusion splicing. These temperature variations have a significant effect on the physical properties of the fiber material. Most of the physical properties as a function of temperature were available in the open literature although they were often only specified over a narrow range of temperature values which required the somewhat risky technique of extrapolation to cover the complete range of interest. In addition, it is noted that in almost all cases, the individual data points represented equilibrium data which is subject to question when applied

to a transient case such as that found in the arc fusion splicing process.

Surface tension data as a function of temperature is very scarce. In fact, conflicting data exists for the slope of the function at high temperatures in the case of very pure single oxide ceramics such as silica. Most material has a decrease in the surface tension as the temperature increases. This tendency is also reported for silica and is used in the present analytical model. It is noted, however, that a positive slope has also been reported for very pure silica [192].

It is noted that the manufacturing process for high silica optical fibers produces an outer surface consisting of very pure silica material. It is possible that, for this case, a positive slope is accurate. The situation is further complicated by the possibility that during the arc fusion heating process contaminants such as dust particles in the discharge heated air or dopant material from the interior of the fiber filament mixes with the silica on the surface and alters the surface tension in a complex manner.

The density of silica is assumed to be that of fused silica in the calculations contained in the analytical model. Figure IV-1 illustrates how the density of glassy materials such as fused silica typically varies with temperature [83].

As shown, the density varies essentially linearly with a moderate slope, to a critical temperature, and then changes to a much steeper slope in the glass transition region. It is noted, however, that glass is a super-cooled liquid and may exhibit a hysteresis effect due to nonequilibrium conditions which typically exist. When temperatures are high enough to enable significant kinetic rates but low enough to favor

higher density phases of materials, the density of a glassy material may change by a discrete step. This process is accompanied by the formation of a crystalline phase in a process called devitrification.

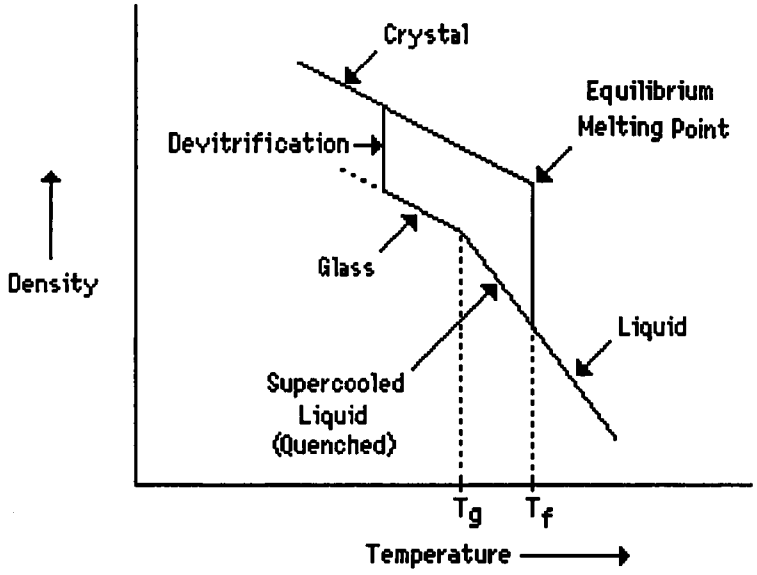

Figure IV-1. Glass Density as a Function of Temperature

Devitrification effects are not included in the present model but may contribute to the results observed experimentally. It has been noted that when a spliced region fails in tension, the break almost always occurs to one side of the splice location but within the heat affected zone [54, 55]. Suggestions have been made that this is due to thermal stresses which are created upon air quenching, that it is due to an alteration of the residual stresses which are used to strengthen the fiber during manufacture, that it is due to contamination which is attracted to the viscous surface during the splicing process, or that it is due to internal stresses which are created when a small region of the fiber material undergoes devitrification.

If devitrification occurs, the sharp increase in density will alter stresses in nearby regions toward those of tension which would account for the drop in ultimate strength observed. It also indicates the possibility that the simple homogeneous stresses assumed in the analytical model are inadequate to model this phenomenon.

The analytical model clearly demonstrates that residual internal stress present from the fiber filament manufacturing process can be a significant factor in the arc fusion splicing process. Details of this impact have not been fully investigated, but it is clear from the present analysis that the balance between the residual axial stress and the residual radial stress is critical to the formation of a bulging and necking-down region in the heating process.

As mentioned previously, present-day high strength fibers often are manufactured with the outer surface under residual axial compressive stresses to improve its resistance to tensile failure. This is typically achieved by placing the inner core region of the fiber under residual tensile stress during the fiber quenching process. The accurate simulation of these fibers with the analytical model may require the input of these residual stress profiles as initial stress data. These effects are presently under investigation.

It is noted, that the deviations between model predictions and experimentally obtained results near the time of fiber separation may not have great significance in the analysis of actual arc fusion splicing processes. The early stages of the fiber surface evolution have a greater similarity to conditions experienced during the arc fusion splicing of two fibers.

Utility in Analyzing Arc Fusion Splicing Process

Arc fusion splicing alters the physical and optical properties of optical filaments being joined. The selection of process control parameters is typically the result of one or more trade-offs in reaching an optimum solution which is practical to implement. These trade-offs are often unique for each specific fiber and end application under consideration. Obtaining sufficient experimental data necessary to support a sensitivity analysis can be time consuming and subject to added experimental uncertainty.

The primary application of the analytical model is in aiding in the understanding of the physical processes involved and in establishing priorities for experimental investigation. It also appears to have considerable potential for "testing" proposed hardware changes without physically modifying the equipment. At this time,however, the fidelity of the model appears to be inadequate to support the selection of optimum process control settings independent of experimental measurements.

Necking down of a fiber optic filament has serious consequences for both the light carrying ability of a fiber and its load carrying ability. A reduction of the outer dimensions of a fiber filament typically corresponds to a proportional reduction in the internal waveguide dimensions as typical of the fiber draw manufacturing process. This reduction in waveguide dimensions will reduce the light carrying ability of the fiber and affect its waveguide cutoff frequency.

In addition to changes in the light carrying ability of the fiber, necking down reduces the load carrying cross-sectional area and, therefore, results in a reduction in the ultimate strength of the fiber.

Most tensile tests of fibers do not account for changes in the cross-sectional area of the fiber under test and report the results as tensile strength based on a nominal cross sectional area. In a similar manner, increasing the cross sectional area of a fiber by the use of a press stroke may allow an increase in the ultimate strength of a splice region and overcome any otherwise inherent weakening processes.

The use of a press stroke has the effect of overcoming the necking down tendency but risks perturbing the optical waveguide and affecting the light conducting properties of the fiber. The results of these experiments and analysis indicate that a properly applied press stroke will involve a trade-off between optical and physical properties in an optimized arc fusion splicing process.

The model has provided evidence that the necking down of the splicing region is associated with the asymmetry which develops in the fiber surface contour. This asymmetry appears to be associated with the slenderness of the fluid region between solid fiber material. In particular, there is reason to believe that a reduction in the size of the heating zone will result in a decrease in the slenderness of the fluid region and may provide a stable symmetric fiber surface contour. This would effectively eliminate the necking down region and allow a reduction or elimination of the press stroke and any accompanying optical waveguide distortions.

As previously discussed, it has been often noted that tensile fracture of fiber splice regions devoid of obvious physical defects always occurs near but not at the fusion point of the splice region. This has been suggested as being a result of devitrification, possibly enhanced by surface contamination of the fibers. The rate of

devitrification for fused silica has been reported to reach a maximum near 1250 °C. This suggest that the heating zone gradient and heating period are relatively critical if one is to avoid devitrification of vitreous silica during the arc fusion splicing process.

It is desirable to reduce the total amount of material as well as the time which any particular volume is exposed to the 1250 °C temperature zone. This will result in a reduction in the total amount of devitrification which occurs in the fiber silica material. It, therefore, appears to be advantageous to have a sharper temperature gradient about the 1250 °C temperature point to reduce the volume of material exposed to these temperatures. It also appears to be advantageous to perform the arc fusion splicing rapidly to decrease the total time to which each fiber volume is exposed to these temperatures.

The analytical model has demonstrated an ability to generate data useful for analyzing stresses and strains generated by the arc fusion splicing process. Examples of axial strains predicted by the model for a fiber undergoing a glow discharge heating cycle are shown in Figure IV-2, Figure IV-3, and Figure IV-4.

These results readily explain the nature of fiber deformation from a physical point of view. During the initial heating shown in Figure IV-2, thermal strain dominates and results in fiber elongation. As heating continues, the fiber softens and viscous strains begin to dominate as shown in Figure IV-3. Surface tension forces result in a fiber surface deformation which in turn results in a reduction of the fiber radius at one location, and growth of the fiber radius at another location. The combined effect of the bulging and necking down is that of an effective growth in the fiber radius. This results in a

contraction in the axial direction due to conservation of mass considerations. As the necking down process continues, surface tension forces dominate over axial forces and increases the axial strains as shown in Figure IV-4.

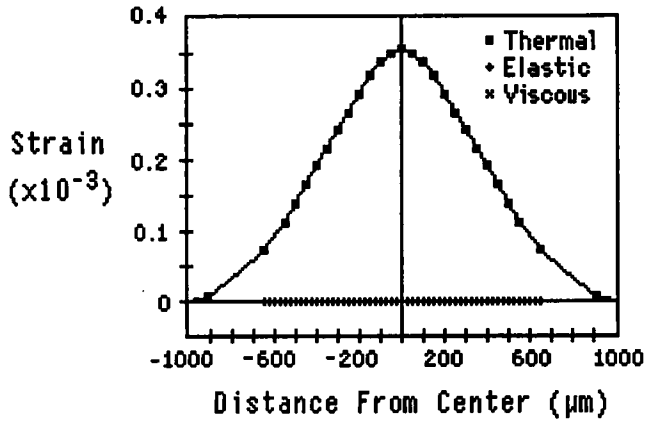

Figure IV-2. Axial Strain After 0.01 Seconds of Heating

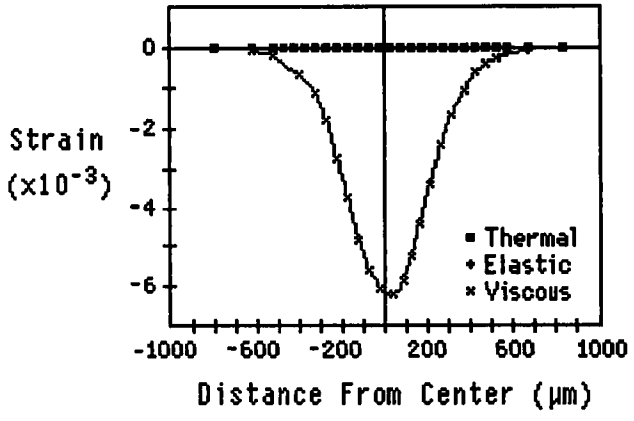

Figure IV-3. Axial Strain After 3.01 Seconds of Heating

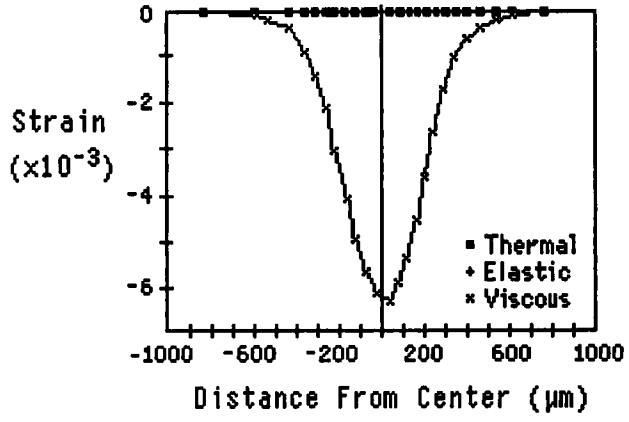

Figure IV-4. Axial Strain After 5.99 Seconds of Heating

Prediction of residual stresses which remain in the fiber after a series of glow discharge heating and air quench cooling cycles are shown in Figure IV-5 and Figure IV-6.

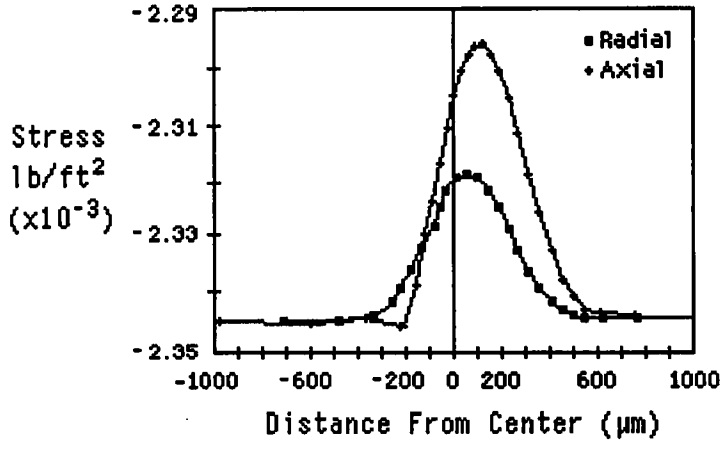

Figure IV-5. Residual Stresses After 3 Heating Cycles

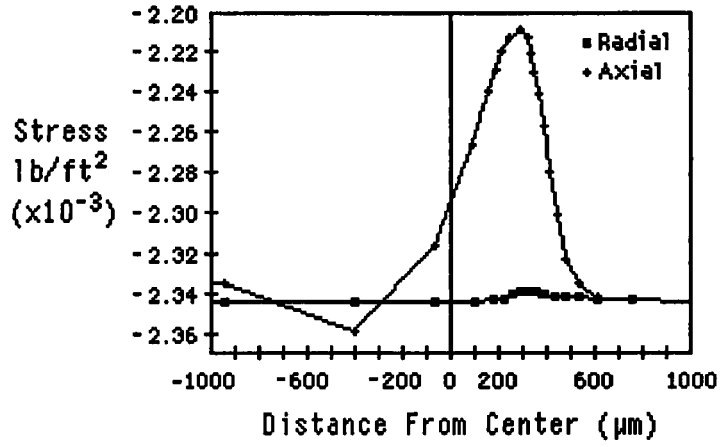

Figure IV-6. Residual Stresses After 5 Heating Cycles

It is anticipated that the magnitudes of residual stresses may not be accurate but it is believed that their distribution along the fibers length is realistic.

It is anticipated that the model may prove to be quite useful in predicting the results of arc fusion splicing for situations where very little experimental is available. It can serve a very useful role in such cases as splicing dissimilar fibers or polarization preserving fibers where internal stress members are present. In addition, it has the potential for analyzing the performance of fiber designs which have not been actually manufactured or determining the sensitivity of the splicing process to manufacturing variables.

Another role not yet explored is the possibility of using the basic heat transfer and viscoelastic response aspects of the model in roles not related to arc fusion splicing. Areas where this might be attractive are in analyzing the fiber drawing process used for fiber manufacture, post draw heat treatments for modification of properties,

or in analyzing the effects of existing processes such as the application of buffer coating material where heat and strain are present.

Other areas where the basic physical interaction modeling might have potential application is in the analysis of micro-bending stresses, stress corrosion cracking, environmental cycling of fiber, and in the manufacture of unique fiber optic components such as tapers and splitters.

CHAPTER V

RECOMMENDATIONS

The computer based analytical model developed as a result of this study has been shown to represent reality with a fidelity that is useful in performing a variety of studies on the arc fusion splicing process. It is apparent, however, that the present model lacks accuracy in predicting magnitudes of deformations for a sequence of heating and cooling cycles. In addition, several physical phenomenon and splicing conditions of secondary interest in the arc fusion splicing process cannot be adequately investigated with the existing model.

Recommendations for continued efforts to improve the utility of the analytical model are given in the following sections. These include recommendations to improve the quality of data used by the model and recommendations to expand the scope of the existing model. Each of these are further classified as a high or a low priority recommendation.

As previously discussed, many of the glow discharge heating parameters and fiber optic material properties are not known with accuracy over the complete range of interest. Any inaccuracies in this data are translated into inaccuracies in model predictions. In addition, the inaccuracy will be propagated throughout the life of the model and any future enhancements. Therefore, a high priority should be given to improving this data.

Glow discharge heating data can be obtained from reported experimental results, from predictions using an analytical model of the glow discharge electro-thermal properties, or from experiments performed

using a specific arc fusion splicer. Each of these sources has advantages and disadvantages.

Reported experimental results were used in this effort as a good source of data generic to a class of arc fusion splicers but suffers from an uncertainty in the appropriateness of fit when predicting the experimental results obtained with a specific arc fusion splicer. Data predicted analytically provides more insight into the physical processes involved, flexibility in extracting data, and the potential for interfacing with the arc fusion splicing model but requires a dedicated development effort. Another advantage to developing an analytical model of glow discharge heat zone is the ability to include discharge current and electrode spacing in the arc fusion splicing parameters which could be investigated with the model.

A high priority should be given to performing experimental measurements on the coefficient of heat transfer for a fiber undergoing glow discharge heating in an arc fusion splicer. No good information on this important parameter was found in the open literature.

Every effort should be expended to insure the quality and accuracy of the algorithms used for the properties of silica as a function of temperature. This should be given a high priority due to its relative importance to the predictive accuracy of the model. Material properties where the most uncertainty presently exists and which have the greatest impact on predicted results are the surface tension and non-linear density changes.

A lower priority recommendation is to incorporate the ability to simulate modifications to the material property of silica as a function of dopant present in the material. This may be more important when

heavily doped silica fibers are being investigated or where the exposed end of a fiber allows the dopant to mix with the surface layers of pure silica.

Analysis with the existing model has shown the results to be sensitive to initial stresses present in the fiber. These stresses are often intentionally induced during fiber manufacture to enhance the strength characteristics of fibers or for controlling their polarization characteristics. A high priority should be given to obtain stress profile information for fibers being simulated. This information is presently treated as proprietary by most fiber manufacturers but is becoming available in the open literature as research into this area continues [107, 109].

Optical absorption and emission characteristics for silica are not constants for all spectral wavelengths being emitted by the glow discharge as assumed in the model. The rationale for using constant values can be found in Appendix A discussing the material properties of silica. It is anticipated, however, that some improvement in the accuracy of the model can be made by incorporating the spectral characteristics of the fiber as a function of wavelength. In addition, the glow discharge is not strictly a black-body emitter as assumed but rather exhibits a wavelength dependence due to the spectral emission of species which make up the air in the discharge volume. Again, it is anticipated that some improvement in the accuracy of the model predictions can be made by incorporating the true spectral characteristics of the glow discharge radiant energy emission.

A high priority recommended modification to the model is its expansion to simulate the heat transfer and viscoelastic response of the

fiber as a function of radius. Because energy transfer is dominated by convection heat transfer, the fiber heats up and cools down from the outer surface inward. This phenomenon can result in stresses which are a function of fiber radius.

CHAPTER VI

CONCLUSIONS

An analytical model for analyzing arc fusion splicing of fiber optic filaments has been developed. The model has been programmed in BASIC and a preliminary analysis have been carried out for high silica fibers. This preliminary analysis has demonstrated substantial agreement with the physical processes observed experimentally.

For a continuous section of fiber heated cyclically in the heat zone of a conventional arc fusion splicer, the analytical model shows the bulging and necking down of the fiber element as observed experimentally. The magnitude of the deformation, however, is not produced in the model with repeated heating cycles as is observed in the experiment. This is attributed to a number of factors related to the quality of input data.

Analysis of results of the analytical model shows the sensitivity to details of the heating conditions which exist within the glow discharge. In particular, the magnitude of the heat transfer coefficient has been shown to have a profound effect on the evolution of the fiber surface deformation. This suggest that, in addition to the geometrical relationship between the heat profile of the glow discharge and the fiber, gas composition, its circulation within the discharge, and ambient conditions such as atmospheric pressure, and humidity may be important variables in the arc fusion process.

The analytical model clearly demonstrates that residual internal stress present from the fiber filament manufacturing process can be a significant factor in the arc fusion splicing process. It is clear from

the present analysis that the balance between the residual axial stress and the residual radial stress is critical to the formation of a bulging and necking-down region in the heating process.

BIBLIOGRAPHY

BIBLIOGRAPHY

1. Kao, C., Bickel, G., "Fiber Connectors, Splices and Couplers," in Fiber Optics Advances in Research and Development, edited by Bernard Bendow and Shashanka S. Mitra, pp. 437-494, Plenum Press, New York, 1979.

2. Drake, M. D., "A Critical Review of Fiber Optic Connectors," SPIE Vol. 512, Fiber Optic Communication Technology, pp.57-69, 1984.

3. Long, C. Wayne, "Fiber Optic Splicing Test Plan," BDM Technical Report No. HTV-85-1064-TR, Contract No. DAAH01-84-D-A006, December 13, 1985.

4. Wheeler, P. C., Kapounek, F. A., "Design Aspects of a D-C Arc Fusion Splicer," Proceedings of the Sixth International Fiber Optics and Communications Exposition, pp. 157-159, September 15-17, 1982.

5. Kato, Yasuyuki, Seikai, Shigeyuki, Shibata, Nori, Tachigami, Shigeru, Toda, Yuichi, Watanabe, Okosu, "Arc-Fusion Splicing of Single-Mode Fibers. 2: A Practical Splice Machine," Applied Optics, Vol. 21, No.11, pp. 1916-1921, June 1, 1982.

6. Kato, Yasuyuki, Seikai, Shigeyuki, Tanifuji, Tadatoshi, "Arc-Fusion Splicing of Single-Mode Fibers: An Apparatus with an Automatic Core-Axis Alignment Mechanism and Its Field Trial Results," Journal of Lightwave Technology, Vol. LT-2, No. 4, pp. 442-447, August 1984.

7. Khoe, K. D., "Practical Machine for Electric Arc Splicing of Optical Fibres in the Field," Electronics Letters, Vol. 15, No. 5, pp. 152-153, March 1, 1979.

8. Tachikura, Masao, "Fusion Mass-Splicing for Optical Fibers Using Electric Discharges Between Two Pairs of Electrodes," Applied Optics, Vol. 23, No. 3, pp. 492-498, 1 February, 1984.

9. Tachikura, Masao, Kashima, Norio, "Fusion Mass-Splices for Optical Fibers Using High-Frequency Discharge," Journal of Lightwave Technology, Vol. LT-2, No. 1, pp. 25-31, February 1984.

10. Hatakeyama, Iwao, Tsuchiya, Haruhiko, "Fusion Splices for Optical Fibers by Discharge Heating," Applied Optics, Vol. 17, No. 12, pp. 1959-1964, 15 June 1978.

11. Khoe, K. D., "Practical Machine for Electric Arc Splicing of Optical Fibres in the Field," Electronics Letters, Vol. 15, No. 5, pp. 152-153, March 1, 1979.

12. Goss, Willis C., "Optical-Fiber-Welding Machine," NASA Tech Briefs, pp.553-554, Summer 1984.

13. Sammueller, Rudolf, "New Generation of Semi-Automatic Glass Fiber Fusion Splicers for Use in the Field," SPIE Vol. 374, Proceedings of Fibre Optics '83, London, England, pp. 7-12, April 19-21, 1983.

14. Tanifuji, Tadatoshi, Kato, Yasuyuki, "Realization of a Low-Loss Splice for Single-Mode Fibers in the Field Using an Automatic Arc-Fusion Splicing Machine," OSA/IEEE Sixth Topical Meeting on Optical Fiber Communication, New Orleans, La, pp. 14-15, 28 February - 2 March 1983.

15. Pacey, G. K., Scott J. R., "A Splicing System for Optical Fiber Cables," Proceedings of 30th International Wire and Cable Symposium, Cherry Hill, N.J., pp. 362-370, November 17-19, 1981.

16. Kawata, Osamu, Hoshino, Kouichi, Ishihara, Koushi, "Core-Axis-Alignment Method to Achieve Ultra-Low-Loss Fusion Splicing for Single-Mode Optical Fibers," Optics Letters, Vol. 9, No. 6, pp. 255-256, June 1984.

17. Kawata, Osamu, Hoshino, Kouichi, Miyajima, Yoshiaki, Ohnishi, Masatoshi, Ishihara, Koushi, "A Splicing and Inspection Technique for Single-Mode Fibers Using Direct Core Monitoring," Journal of Lightwave Technology, Vol. LT-2, No. 2, pp. 185-191, April 1984.

18. Katagiri, Toshiaki, Tachikura, Masao, Sankawa, Izumi, "Optical Microscope Observation Method of a Single-Mode Optical-Fiber Core for Precise Core-Axis Alignment," Journal of Lightwave Technology, Vol. LT-2, No. 3, pp. 277-283, June 1984.

19. Kato, Y., Tanifuji, T., Tokuda, M., Uchida, N., "New Optical Monitoring Method for Arc-Fusion Splice of Single-Mode Fibres and High Precision Estimation of Splice Loss," Electronics Letters Vol. 18, No. 22, pp. 972-973, October 28, 1982.

20. Tardy, A., Jurczyczyn, M., Jeunhomme, L., Carratt, M., Hakoun, R., Mignien, M., Trezeguet, J. P., "Automatic Single Mode Fibre Splicing Machine Without Power Monitoring," pp. 113-116, Ninth European Conference on Optical communication, Geneva, Switzerland, 23-26 October, 1983, Optical Communication, Edited by H. Melchior and A. Sollberger, North-Holland, New York, 1983.

21. Suzuki, M., Kikuchi, Y., Yamada, T., Watanabe, O., "Arc Fusion Splicing Machine for Single Polarization Single Mode Optical Fibers," pp. 117-120, Ninth European Conference on Optical communication, Geneva, Switzerland, 23-26 October, 1983, Optical Communication, Edited by H. Melchior and A. Sollberger, North-Holland, New York, 1983.

22. Krause, John T., Reed W. A., Walker, K. L., "Splice Loss of Single-Mode Fiber as Related to Fusion Time, Temperature, and Index Profile Alteration," Journal of Lightwave Technology, Vol. LT-4, No. 7, July 1986.

23. Misra, P. K., "Practical Experiences in Fiber Optic Splicing," Proceedings of Fiber Optics and Communications (FOC 80), September 1980.

24. "Optical Fiber Splicing," Technical Report No. TD-84009 B, The Furukawa Electric Company, Ltd., May 1984.

25. FSM-20 Arc Fusion Splicer Manual, Fujikura, Ltd.

26. Instruction Manual for Model PFS-200 Series Optical Fiber Splicer, Power Technology, Inc.

27. Pacey, G. K., Dalgleish, J. F., "Fusion Splicing of Optical Fibres," Electronics Letters, Vol. 15, No. 1, pp. 32-34, January 4, 1979.

28. Kato, Yasuyuki, Seikai, Shigeyuki, Tateda, Mitsuhiro, "Arc-Fusion Splicing of Single-Mode Fibers. 1: Optimum Splice Conditions," Applied Optics, Vol. 21, No.7, pp. 1332-1336, April 1, 1982.

29. Kato, Yasuyuki, Tanifuji, Tadatoshi, Kashima, Norio, Arioka, Ryosuke, "Arc-Fusion Splicing of Single-Mode Fibers. 3: A Highly Efficient Splicing Technique," Applied Optics, Vol. 23, No.15, pp. 2654-2659, August 1, 1984.

30. Nelson, M. D., Fearnehough, H. T., Goldstein, R., Goss W. C., "Single Mode Glass Fiber Welding," Proceedings of the Technical Program, Electro-Optics/Laser 79 Conference and Exposition, Anaheim, California, pp. 18-22, October 23-25, 1979.

31. Bisbee, D. L., "Splicing Silica Fibers with an Electric Arc," Applied Optics Vol. 15, No. 3, pp. 796-798, March 1976.

32. Inada, Koichi, "Low-Loss Single-Mode Fiber and Its Splicing," pp. 195-207, Optical Devices and Fibers, edited by Y. Suematsu, North-Holland, New York, 1984.

33. Andrews, Patrick V., Owens, David, "Precision Cleaving and Fusion Welding of Single Mode Fibres," SPIE Vol. 522, Proceedings of Fibre Optics '85 (Sira), pp. 18-24, 1985.

34. "Alternative Method to Fusion Splice Optical Fiber," Technical Bulletin No. 1, Power Technology, Inc., October 1984.

35. Kozikowski, Carrie, "Optical Fiber Arc Fusion Splice Course," Briefing notes presented at ITT, Roanoke, Virginia, January, 1985.

36. Kohanzadeh, Y., "Hot Splices of Optical Waveguide Fibers," Applied Optics, Vol. 15, No. 3, March 1976.

37. Das, A. K., Bhattacharyya, S., "Optimum Conditions for Fusion Splicing of Optical Fiber," Proceedings of the IEEE, Vol. 72, No. 7, pp. 983-984, July 1984.

38. Hatakeyama, Iwao, Tsuchiya, Haruhiko, "Fusion Splices for Single-Mode Optical Fibers," IEEE Journal of Quantum Electronics, Vol. QE-14, No. 8, pp. 614-619, August 1978.

39. Tanifuji, Tadatoshi, Kato, Yasuyuki, "Realization of a Low-Loss Splice for Single-Mode Fibers in the Field Using an Automatic Arc-Fusion Splicing Machine," Sixth Topical Meeting on Optical Fiber Communication, New Orleans, pp. 14, 28 February - 2 March, 1983.

40. Leach, J. S., Robertson, A. J., "High Reliability Splicing of Single-Mode Optical Fibers," Electrical Communication, Vol. 59, No. 4, pp. 401-407, 1985.

41. Ravagalia, R., "Field Experience with Installing and Splicing Multimode and Single-Mode Optical Fiber Cables," Electrical Communication, Vol. 59, No. 4, pp. 408-412, 1985.

42. Ogai, M., Toda, Y., Wantanabe, O., Kato, Y., Tsuchiya, H., "Fusion Splicing of Single-Mode Optical Fibers," Proceedings of Fiber Optics and Communications (FOC 80), September 1980.

43. Miller, Calvin, "Single-Mode Fiber Splicing," 7th Conference on Optical Fiber Communication, New Orleans, pp. 70, February 28 - 25, 1984.

44. Arai, T., Watanabe, O., Inada, K., Katsuyama, Y., "Arc Fusion Splice of Low-Loss Single-Mode Fiber," pp. 6.2-1 - 6.2-4, Proceedings of European Conference on Optical Communication, Amsterdam, September 17-19, 1979.

45. Asano, Yasuo, Suzuki, Shuzo, Yokota, Hiroshi, Tanaka, Gotaro, "Splicing of Silica Core Single-Mode Fibers," pp. 74, Optical Fiber Communication Conference Technical Digest, 1986.

46. Ishikura, Akihiko, Kato, Yasuyuki, Abe, Tetsuji, Miyauchi, Mitsuru, "Optimum Fusion Splice Method for Polarization-Preserving Fibers," Applied Optics, Vol. 25, No. 19, pp. 3455-3459, October 1, 1986.

47. Hatakeyama, Iwao, Tsuchiya, Haruhiko, "Fusion Splices for Single-Mode Optical Fibers by Discharge Heating," Review of the Electrical Communication Laboratories, Vol. 27, No. 7-8, pp. 532-542, July-August 1979.

48. Egashira, K., Kobayshi, M., "Optical Fiber Splicing with a Low-Power CO_2 Laser," Applied Optics, Vol. 16, No. 6, pp. 1636-1638, June 1977.

49. Fujita, Hiroyuki, Suzaki, Yasuzi, Tachibana, Atsushi, "Optical Fiber Splicing Technique with a CO_2 Laser," Applied Optics, Vol. 15, No. 2, pp. 320-321, February 1976.

50. Pellaux, J. P., Zurcher, J. F., "Fusion Splices for Multimode Optical Fibre Using a Gas Flame Heat Source," EFOC 80, Proceedings of the First European Fiber Optics and Communications Exposition, Paris, France, pp. 101-103, July 1-3, 1980.

51. Decker, G. A., Giangrossi, R. V., "High Strength Low Loss Flame Fusion Splicing of Singlemode Fibers for Undersea Cable," SPIE Vol. 479, Fiber Optic Couplers, Connectors, and Splice Technology, 1984.

52. Krause, J. T., Kurkjian, C. R., Paek, U. C., "Tensile Strength of 4 Gpa for Lightguide Fusion Splices," Electronics Letters, Vol. 17, No. 21, October 15, 1981.

53. Miyajima, Yoshiaki, Furukawa, Shinichi, Kawata, Osamu, "Submarine Optical Fiber Cable Containing High-Strength Splices," Journal of Lightwave Technology, Vol. LT-1, No. 1, March 1983.

54. Tachikura, Masao, Haibara, Tadashi, "Devitrification Effect on Optical-Fiber Strength Reduction by Fusion Splicing," Journal of Lightwave Technology, Vol. LT-3, No. 3, pp. 662-668, June 1985.

55. Das, A. K., Roy, M. M., "Some New Results on Disordered Zone Around Splicing Region of Optical Fiber," Proceedings of the Canadian Communications and Energy Conference, pp. 317-319, October 13-15, 1982.

56. Briggs, D. R., Jayne, L. M., "Splice Loss and Tensile Strength of Thermally Fused Optical Waveguide Fibers," Proceedings of the Technical Program, Electro-Optics/Laser 78 Conference and Exposition, Boston, Massachusetts, pp. 251-258, September 19-21, 1978.

57. Briggs, D. R., Jayne, L. M., "Splice Losses in Fusion-Spliced Optical Waveguide Fibers with Different Core Diameters and Numerical Apertures," Proceedings of 27th International Wire and Cable Symposium, Fort Monmouth, N. J., pp. 356-361, Cherry Hill, N. J., November 14-16, 1978.

58. Hevey, L. M., Saikkonen, S. L., Taylor, D. H., "Theoretical Splice Loss Study of Single-Mode Fibers," SPIE Vol. 479, Fiber Optic Couplers, Connectors, and Splice Technology, 1984.

59. Krause, J. T., Kurkjian, C. R., Paek, U. C., "Strength of Fusion Splices for Fiber Lightguides," Electronics Letters, Vol. 17, No. 6, March 19, 1981.

60. Das, A. K., Bhattacharyya, S., "Loss and Mechanical Strength of Splices," Electronics Letters, Vol. 21, No. 2, pp. 81-83, January 17, 1985.

61. Data Sheet on Model SUMIOFCAS Type-34 Optical Fiber Fusion Splicer, Sumitomo Electric.

62. Data Sheet on Model S-172 Fusion Splicing System, Furukawa Electric.

63. Data Sheet on Model FW-304A Fusion Splicer, Orionics.

64. Data Sheet on Model PFS-300 Optical Fiber Splicer, Power Technology, Inc.

65. Data Sheet on Model NT7L30 Automated Fusion Set, Northern Telecom.

66. Data Sheet on Model FSM-20 Fiber Fusion Splicer, Fujikura, Ltd.

67. Doremus, Robert H., Glass Science, John Wiley and Sons, Inc., New York, 1973.

68. Fontana, E. H., Plummer, W. A., "A Study of Viscosity-Temperature Relationships in the GeO_2 and SiO_2 Systems," Physics and Chemistry of Glasses, Vol. 7, No. 4, pp. 139-146, August 1966.

69. Condon, Edward U., "Radiative Transport in Hot Glass," Journal of Quantum Spectroscopic Radiation Transfer, Vol. 8, pp. 369-385, 1968.

70. Anderson, E. E., Viskanta, R., "Effective Conductivity for Conduction-Radiation by Taylor Series Expansion," Journal of Basic Engineering, pp. 1216-1220, September 1968.

71. Appleton, A., Chiranjivi, T., Jataripour-Ghazvini, M., "The Absorption and Photoconductivity Spectra of Vitreous SiO_2," pp. 94-98, The Physics of SiO_2 and its Interfaces, Edited by Sokrates T. Pantelides, Pergamon Press, Inc., New York, 1978.

72. Spinner, Sam, "Elastic Moduli of Glasses at Elevated Temperatures by a Dynamic Method," Journal of The American Ceramic Society, Vol. 39, No. 3, pp. 113-118, March 1956.

73. Kozlovskaya, E. I., "Elastic Properties of Glass in Relation to Temperature," pp. 344-347, The Structure of Glass, Vol. 2, Translated from Russian Proceedings of the Third All-Union Conference on the Glassy State, Leningrad, November 16-20, 1959, Consultants Bureau, New York, 1960.

74. Rawson, H., Inorganic Glass-Forming Systems, Academic Press, Inc., New York, 1967.

75. Synthetic Fused Silica, Catalog 302-M, Dynasil Corporation of America

76. Isard, J. O., "The Emission of Thermal Radiation from Hot Glass. Part 1. Emissivity of Sheets, Spheres, Cylinders, and Tubes," Glass Technology, Vol. 27, No. 1, pp. 24-31, February 1986.

77. Anderson, Edward E., Viskanta, Raymond, "Effective Thermal Conductivity for Heat Transfer Through Semitransparent Solids," Journal of the American Ceramic Society, Vol. 56, No. 10, pp. 541-546, October 1973.

78. Moynihan, Cornelius T., Eastel, Allan J., Wilder, James, "Dependence of the Glass Transition Temperature on Heating and Cooling Rate," The Journal of Physical Chemistry, Vol. 78, No. 26, pp. 2673-2677, 1974.

79. Cooper, A. R., Jr., "A Dimensionless Parameter to Characterize the Glass Transition," Physics and Chemistry of Glasses, Vol. 23, No. 1, pp. 44-45, February 1982.

80. Pantelides, Sokrates T., "The Optical Absorption Spectrum of SiO_2," pp. 80-84, The Physics of SiO_2 and its Interfaces, Edited by Sokrates T. Pantelides, Pergamon Press, Inc., New York, 1978.

81. Armstrong, Baxter H., "Thermal Conductivity of SiO_2," pp. 128-132, The Physics of SiO_2 and its Interfaces, Edited by Sokrates T. Pantelides, Pergamon Press, Inc., New York, 1978.

82. Jastrzebski, Zbigniew D., The Nature and Properties of Engineering Materials, John Wiley and Sons, Inc., New York, 1959.

83. Rawson, Harold, Properties and Applications of Glass, Glass Science and Technology 3, Elsevier Science, New York, 1980.

84. Herman, Herbert, Advances in Materials Research, Volume 5, Wiley-Interscience, New York, 1971.

85. Hillig, W. B., "Plastic Behavior and Fracture in Glass," in Microplasticity, edited by Charles J. McMahon, Jr., Wiley-Interscience, New York, 1968.

86. Lacy, E. D., "A Statistical Model of Polymerization/Depolymerization Relationships in Silicate Melts and Glasses," Physics and Chemistry of Glasses, Vol. 6, No. 5, pp. 171-180, October 1965.

87. Hetherington, G., Jack, K. H., Kennedy, J. C., "The Viscosity of Vitreous Silica," Physics and Chemistry of Glasses, Vol. 5, No. 5, pp. 130-136, October 1964.

88. Chui, Granger K., Gardon, Robert, "Interaction of Radiation and Conduction in Glass," Journal of The American Ceramic Society, Vol. 52, No. 10, pp. 548-553, October 1969.

89. Bell, R. J., Dean, P., "The Configurational Entropy of Vitreous Silica in the Random Network Theory," Physics and Chemistry of Glasses, Vol. 9, No. 4, pp. 125-127, August 1968.

90. Condon, E. U., "Physics of the Glassy State. III. Strength of Glass," American Journal of Physics, Vol. 22, No. 4, pp. 224- 232, April 1954.

91. Anderson, E. E., Viskanta, R., Stevenson, W. H., "Heat Transfer Through Semitransparent Solids," Transactions of the ASME, Journal of Heat Transfer, pp. 179-186, May 1973.

92. Eryou, N. D., Glicksman, L. R., "An Experimental and Analytical Study of Radiative and Conductive Heat Transfer in Molten Glass," Transactions of the ASME, Journal of Heat Transfer, pp. 224-230, May 1972.

93. Kellett, B. S., "The Steady Flow of Heat through Hot Glass," Journal of the Optical Society of America, Vol. 42, pp. 339-343, No. 5, May 1952.

94. Sibulkin, Merwin, "Radiative Properties of Model Gases for Applications in radiative Energy Transfer," Journal of Quantum Spectroscopic Radiation Transfer, Vol. 8, pp. 451-470, 1968.

95. Gardon, Robert, "Some Heat Transfer Problems in Glass Technology," pp.85-95, Eighth International Congress on Glass (1968), Society of Glass Technology, Sheffield England, 1969.

96. Nishimura, M., Hasatani, M., Sugiyama, S., "Simultaneous Heat Transfer by Radiation and Conduction. High-Temperature One-Dimensional Heat Transfer in Molten Glass," International Chemical Engineering, Vol. 8, No. 4, pp. 739-745, October 1968.

97. Gardon, Robert, "A Review of Radiant Heat Transfer in Glass," Journal of The American ceramic Society, Vol. 44, No. 7, pp. 305-312, July 1961.

98. Kingery, W. D., "Heat-Conductivity Processes in Glass," Journal of The American ceramic Society, Vol. 44, No. 7, pp 302-304, July 1961.

99. Napolitano, Albert, Hawkins, Earl, G., "Viscosity of a Standard Soda-Lime-Silica Glass," Journal of Research of the National Bureau of Standards-A. Physics and Chemistry, Vol. 68A, No. 5, pp. 439-448, September-October, 1964.

100. Glicksman, L. R., "The Cooling of Glass Fibers," Glass Technology, Vol. 9, No. 5, pp. 131-138, October 1968.

101. Anderson, O. L., "Cooling Time of Strong Glass Fibers," Journal of Applied Physics, Vol. 29, No. 1, pp. 9-12, January 1958.

102. Antonov, V. F., Kutepov, V. S., Naumkin, O. V., Puchenkov, V. G., Shushkevich, G. A., "Measurement of Elastic Moduli for Quartz Fibers," Measurement Techniques, Vol. 25, No. 7, pp. 826-828, July 1982, Translated from Russian December 1982.

103. Alekseyenko, M. P., Khabarov, Yu. M., "Viscosity of Glass Fibers with and without Concentric Glass Casings," Soviet Journal of Optical Technology, Vol. 34, No. 1, pp. 444-448, January-February 1967.

104. Homsy, G. M., Walker, K., "Heat Transfer in Laser Drawing of Optical Fibers," Glass Technology, Vol. 20, No. 1, pp. 20-26, February 1979.

105. Smith, Harry D., Mattox, Douglas M., "Estimates of the Melting Rate of Quartz," Glass Technology, Vol. 23, No. 6, December 1982.

106. Hetherington, G., Jack, K. H., "Water in Vitreous Silica. Part I. Influence of 'Water' Content on the Properties of Vitreous Silica," Physics and Chemistry of Glasses, Vol. 3, No. 4, August 1962.

107. Namihira, Yoshinori, "Opto-Elastic Constant in Single Mode Optical Fibers," Journal of Lightwave Technology, Vol. LT-3, No. 5, pp. 1078-1083, October 1985.

108. Schere, G., Vergano, P. J., Uhlmann, D. R., "A Study of Quarts Melting," Physics and Chemistry of Glasses, Vol. 11, No. 3, pp. 53-58, June 1970.

109. Paek, U. C., Kurkjian, C. R., "Calculation of Cooling Rate and Induced Stresses in Drawing of Optical Fibers," Journal of The American Ceramic Society, Vol. 58, No. 7-8,pp. 330-335, July-August 1975.

110. Weir, G. J., White, S. P., "A Two Dimensional Mathematical Model of a Forehearth," Glass Technology, Vol. 23, No. 2, pp. 113-119, April 1982.

111. Moult, A., "Two and Three Dimensional Mathematical Models of Glass Tank Furnaces," Glass Technology, Vol. 23, No. 2, pp. 106-112, April 1982.

112. Cozzi, C., Blanchet, P., Segond, J., "Design of a Glass Furnace Throat by Means of a Simple Mathematical Model," Glass Technology, Vol. 24, No. 2, pp. 63-66, April 1983.

113. Pekcelen, Sina, "Verification of Model of Molten Glass Flow in a Forehearth," Thesis presented to the United States Naval Postgraduate School, December 1969.

114. Carling, J. C., "A Reappraisal of the Mathematical Modeling of Flow and Heat Transfer in Glass Tank Forehearths," Glass Technology, Vol. 23, No. 5, pp. 201-222, October 1982.

115. Suendermann, J., "The Application of Finite Element and Finite Difference Techniques in Hydrodynamical Numerical Models," Formulations and Computational Algorithms in Finite Element Analysis: U.S.-Germany Symposium, edited by Klaus-Jurgen Bathe, J. Tinsley Oden, and Walter Wunderlich, Boston, Massachusetts, August 1976, Halliday Lithograph Corporation, 1977.

116. Ryskin, G., Leal, L. G., "Numerical Solution of Free-Boundary Problems in Fluid Mechanics. Part 1. The Finite-Difference Technique," Journal of Fluid Mechanics, Vol. 148, pp. 1-17, November 1984.

117. Beale, J. Thomas, "The Initial Value Problem for the Navier-Stokes Equations with a Free Surface," Communications of Pure and Applied Mathematics, Vol. 34, pp. 359-392, May 1981.

118. Chien, John C., "A General Finite-Difference Formulation with Application to Navier-Stokes Equations," Computers and Fluids, Vol. 5, pp. 15-31, 1977.

119. MacCormack, R. W., "A Numerical Method for Solving the Equations of Compressible Viscous Flow," AIAA Journal, Vol. 20, No. 9, pp. 1275-1281, September 1981.

120. Kawahara, Mutsuto, Takeuchi, Norio, "Mixed Finite Element Method for Analysis of Viscoelastic Fluid Flow," Computers and Fluids, Vol. 5, pp. 33-45, 1977.

121. Reddy, K. R., Tanner, R. I., "Finite Element Solution of Viscous Jet Flows with Surface Tension," Computers and Fluids, Vol. 6, pp. 83-91, 1978.

122. Harlow, Francis H., Welch J. Eddie, "Numerical Calculation of Time-Dependent Viscous Incompressible Flow of Fluid with Free Surface," The Physics of Fluids, Vol. 8, No. 12, pp. 2182-2189, December 1965.

123. Napolitano, I. G., Ceiia, C., Viviani, A., "Numerical Simulation of Unsteady Thermal Marangoni Flows," Proceedings of the 5th European Symposium on Material Sciences under Microgravity, Schloss Elmau, pp. 251-258, 5-7 November 1984.

124. McNeil, Thomas J., Cole, Robert, Subrimanian, R. Shankar, "Surface-Tension-Driven Flow in a Glass Melt," Journal of American Ceramic Society, Vol. 68, No. 5, pp. 254-259, May 1985.

125. Kawahara, M., Ramaswamy, B., Anjyu, A., "Lagrangian Finite Element Method for Non Linear Free Surface Motions," Finite Elements in Computational Mechanics, Volume 2, edited by Tarun Kant, Proceedings of FEICOM-85, Bombay, India, 2-6 December 1985, Pergamon Press, Inc., New York, 1986.

126. Shah, Yatish T., Pearson, J. R. A., "On the Stability of Nonisothermal Fiber Spinning - General Case," Industrial Engineering Chemical Fundamentals, Vol. 11, No. 2, pp. 150-153, 1972.

127. Burgman, J. A., "Liquid Glass Jets in the Forming of Continuous Glass Fibres," Glass Technology, Vol. 11, No. 4, August 1970.

128. Sokkar, T. Z. N., "Determination of Dopant Flow Variation in Graded-Index Fiber," Applied Optics, Vol. 24, No. 14, pp. 2048-2050, 15 July 1985.

129. Oh, Shin Moo, "Cooling Rates of Optical Fibers During Drawing," Ceramic Bulletin, Vol. 58, No. 11, pp. 1108-1110, 1979.

130. Arridge, R. G. C., Prior, Kathleen, "Cooling Time of Silica Fibres," Nature, Vol. 203, No. 4943, pp. 386-387, July 25, 1964.

131. Jaeger, Raymond E., "Laser Drawing of Glass Fiber Optical Waveguides," Ceramic Bulletin, Vol. 55, No. 3, pp. 270-273, 1976.

132. Kase, Susumu, Matsuo, Tatsuki, "Studies on Melt Spinning. I. Fundamental Equations on the Dynamics of Melt Spinning," Journal of Polymer Science: Part A, Vol. 3, pp. 2541-2554, 1965.

133. Manfre, G., "Some Aspects of Rheology During Spinning of Glass Fibers," 7th International Congress on Glass, Vol. 1, pp. 78.2-7, 1965.

134. Miller, T. J., Geyling, F. T., "One-Dimensional Models for the Co-Drawing of Preform Rods in Tubes," Journal of Lightwave Technology, Vol. LT-2, No. 4, pp. 349-353, August 1984.

135. Geyling, F. T., Walker, K. L., Csencsits, R., "The Viscous Collapse of Thick-Walled Tubes," Transactions of the ASME Journal of Applied Mechanics, Vol. 50, pp. 303-, June 1983.

136. Paek, U. C., Runk, R. B., "Physical Behavior of the Neck-Down Region During Furnace Drawing of Silica Fibers," Journal of Applied Physics, Vol. 49, No. 8, pp. 4417-4422, August 1978.

137. Paek, U. C., Weaver, A. L., "Formation of a Spherical Lens at Optical Fiber Ends with a CO_2 Laser," Applied Optics, Vol. 14, No. 2, pp. 294-298, February 1975.

138. Mhaskar, R. D., Shah, Y. T., "Stability Analysis of Glass Fibre Spinning," Glass Technology, Vol. 18, No. 5, pp. 152-158, October 1977.

139. Meyyappan, M., Subramanian, R. S., Wilcox, W. R., Smith, H., "Bubble Behavior in Molten Glass in a Temperature Gradient," Proceedings of the Materials Research Society 1981 Annual Meeting, Materials Processing in the Reduced Gravity Environment of Space, Edited by Guy E. Rindone, pp. 311-314, 1982.

140. Weinberg, Michael, "Glass Processing In Space," The Glass Industry, pp. 22-27, March 1978.

141. Tress, H. J., "Some Distinctive Contours Worn on Alumina-Silica Refractory Faces by Different Molten Glasses: Surface Tension and the Mechanism of Refractory Attack," Journal of the Society of Glass Technology, Vol. XXXVIII, pp. 89-100, 1954.

142. Shartsis, Leo, Capps, Webster, "Surface Tension of Molten Alkali Borates," Journal of The American Ceramic Society, Vol. 35, No. 7, pp. 169-172, July 1952.

143. Subramanian, R. Shankar, Cole, Robert, Annamalai, P., Jayaraj, K., "Physical Phenomena in Containerless Glass Processing," NASA Contractor Report No. NASA CR-162007, January 1982.

144. Cassidy, D. C., Gjostein, N. A., "Capillarity-Induced Smoothing of Glass Surfaces by Viscous Flow," Journal of The American Ceramic Society, Vol. 53, No. 3, pp. 161-168, March 1970.

145. Bochove, Erik, Costa, Jose', M. L., "Surface Tension Effects on the Making of Smooth Coatings for Optical Fibers," pp. 5.5-2 - 5.5-4, Proceedings of European Conference on Optical Communication, Amsterdam, September 17-19, 1979.

146. Schwabe, D., Scharmann, A., Preisser, F., Oeder, R., "Experiments on Surface Tension Driven Flow in Floating Zone Melting," Journal of Crystal Growth, Vol. 43, pp. 305-312, 1978.

147. Marwedel, H. Jersen, "Remarks on the Influence of Surface Tension in Glass Melting Processes," Journal of the Society of Glass Technology, Vol. XXI, pp. 432-441, 1937.

148. Levich, V. G., Krylov, V. S., "Surface-Tension-Driven Phenomena," Annual Review of Fluid Mechanics, pp. 293-316, Edited by William R. Sears and Milton Van Dyke, Volume 1, Annual Reviews, Inc., Palo Alto, California, 1969.

149. Mackenzie, J. K., Shuttleworth, R., "A Phenomenological Theory of Sintering," Proceedings of Physical Society, Vol. LXII, 12-B, pp. 833-852, 1949.

150. Cutler, Ivan B., Henrichsen, Roy E., "Effect of Particle Shape on the Kinetics of Sintering of Glass," Journal of The American Ceramic Society, Vol. 51, No. 10, pp. 604-605, October 1968.

151. Cutler, Ivan B., "Sintering of Glass Powders During Constant Rates of Heating," Journal of The American Ceramic Society, Vol. 52, No. 1, pp. 14-17, January 1969.

152. Cutler, Ivan B., "Effect of Water Vapor on the Sintering of Glass Powder Compacts," Journal of The American Ceramic Society, Vol. 52, No. 1, pp. 11-13, January 1969.

153. Scherer, George W., "Sintering of Low-Density Glasses: I, Theory, "Journal of The American Ceramic Society, Vol. 60, No. 5-6, pp. 236-239, May - June 1977.

154. Scherer, George W., Bachman, David L., "Sintering of Low-Density Glasses: II, Experimental Study," Journal of The American Ceramic Society, Vol. 60, No. 5-6, pp. 239-243, May - June 1977.

155. Scherer, George W., "Sintering of Low-Density Glasses: III, Effect of a Distribution of Pore Sizes," Journal of The American Ceramic Society, Vol. 60, No. 5-6, pp. 243-246, May - June 1977.

156. Krohn, David A., "Determination of Axial Stress in Clad Glass Fibers," Journal of The American Ceramic Society, Vol. 53, No. 9, pp. 505-507, September 1970.

157. Xiao, Y. M., Bass, Michael, "Thermal Stress Limitations to Laser Fire Polishing of Glasses," Applied Optics, Vol. 22, No. 16, pp. 2933-2936, September 15, 1983.

158. Wolffer, Nicole, Zaganiaris, Alcibiade, Balay, Jean-Jacques, "Internal Stress Evaluation and Reliability of Fiber Fusion Splices," pp. 125-128, Optical Communication, Proceedings of the Ninth European Conference on Optical Communication, Geneva, Switzerland, 23-26 October, 1983.

159. Scriven, L. E., Sternling, C. V., "The Marangoni Effects," Nature, Vol. 187, pp. 186-188, July 16, 1960.

160. Scherer, G. W., "Optical Profile Distortion Caused by Thermal Stresses," pp. 10.5-1 - 10.5-3, Proceedings of the European Conference on Optical Communication, Amsterdam, September 17-19, 1979.

161. Llewellyn-Jones, F., The Glow Discharge and an Introduction to Plasma Physics, John Wiley and Sons, Inc., New York, 1966.

162. Brown, Sanborn C., Introduction to Electrical Discharges in Gases, John Wiley and Sons, Inc., New York, 1966.

163. Papoular, Renaud, Electrical Phenomena in Gases, Elsevier Science, New York, 1965.

164. Sigmond, R. S., Goldman, M., "Corona Discharge Physics and Applications," NATO Advanced Study Institute on Electrical Breakdown and Discharges in Gases, Part B: Macroscopic Processes and Discharges, Edited by Erich E. Kunhardt and Lawrence H. Luessen, Plenum Press, New York, 1983.

165. Loeb, Leonard B., Electrical Coronas: Their Basic Physical Mechanisms, University of California Press, Berkeley, 1965.

166. Powell, C. W., Ryan, H. M., "The Effects of Elevating Temperature on the Breakdown Properties of Atmospheric Air," pp. 209-212, Sixth International Conference on Gas Discharges and Their Applications, 8-11 September, 1980.

167. Berger, G., "Influence of a Corona Discharge on the Subsequent One in Atmospheric Air," pp. 294-297, Third International Conference on Gas Discharges, 9-12 September 1974.

168. Ellion, M. Edmund, "A Study of Electrical Discharge in Low-Pressure Air," Jet Propulsion Laboratory, Technical Report No. 32-678, NASA-CR 57646, April 1, 1965.

169. Vriens, L., Smeets, A. H. M., Cornelissen, H. J., "Modeling of a Glow Discharge," NATO Advanced Study Institute on Electrical Breakdown and Discharges in Gases, Part B: Macroscopic Processes and Discharges, Edited by Erich E. Kunhardt and Lawrence H. Luessen, Plenum Press, New York, 1983.

170. Warren, Roger, "Interpretation of Field Measurements in the Cathode Region of Glow Discharges," Physical Review, Vol. 98, No. 6, pp. 1658- 1664, June 15, 1955.

171. Bergmann, G., Gerthsen, P., "Pre-Breakdown Phenomena of Discharges Between Heated Tungsten Electrodes," pp. 270-272, 2nd International Conference on Gas Discharges, 11-15 September 1972.

172. Breene, R. G., Nardone, M. C., "Radiant Emission from High Temperature Equilibrium Air," Journal of Quantitative Spectroscopy and Radiative Transfer, Vol. 2, pp. 272-292, 1962.

173. Kivel, B., Bailey, K., "Tables of Radiation from High Temperature Air," Avco Research Laboratory, Research Report No. 21, December 1957.

174. Marston, C. H., Pugmire, T. K., "Real Gas Radiation with Self-Absorption and Space Varying Temperature," NTS Report No. N65-12395, 1965.

175. Armstrong, B. H., Sokoloff, J., Nicholls, R. W., Holland, D. H., Meyerott, R. E., "Radiative Properties of High Temperature Air," Journal of Quantitative Spectroscopy and Radiative Transfer, Vol. 1, pp. 143-162, 1961.

176. Sampson, Douglas H., Radiative Contributions to Energy and Momentun Transport in a Gas, Wiley-Interscience, New York, 1965.

177. Chandrakar, K., "Electron Temperature in an A.C. Glow Discharge in Air," British Journal of Applied Physics, Vol. 16, pp. 449-451, 1965.

178. Boulloud, A., Charrier, J., "Current Density on the Plane Electrode of a Positive Point-To-Plane Glow Corona Discharge," pp. 110-113, Sixth International Conference on Gas Discharges and Their Applications, 8-11 September 1980.

179. Akazaki, M., Tsuneyasu, I., "Breakdown Mechanisms of the Positive Point to Plane Gap in Air Under Impulse Voltages," pp.220-223, Third International Conference on Gas Discharges, 9-12 September, 1974.

180. Kip, Arthur F., "Onset Studies of Positive Point-to-Plane Corona in Air at Atmospheric Pressure," Physical Review, Vol. 55, pp. 549-556, March 15, 1939.

181. Starr, E. C., "High-Voltage D-C Point Discharges," AIEE Transactions, Vol. 60, pp. 356-362, 1941.

182. Burden, Richard L., Faires, J. Douglas, Numerical Analysis, third edition, Prindle, Weber and Schmidt, Boston, Massachusetts, 1985.

183. Weber, H. E., Pugmire, T. K., "Comparisons of Experimental and Theoretical Arc Column Characteristics," IEEE Transactions on Nuclear Science, pp. 237-248, January 1964.

184. Llewellyn-Jones, F., The Glow Discharge and an Introduction to Plasma Physics, John Wiley and Sons, Inc., New York, 1966.

185. Corbine, J. D., Gaseous Conductors, Theory and Engineering Applications, Dover Publications, Inc., New York, 1958.

186. Private Communications with Tsutomu Onodera, Fujikura, Ltd., January, 1987.

187. Viegas, John R., Peng, T.C., "Electrical Conductivity of Ionized Air in Thermodynamic Equilibrium", Journal of The American Rocket Society, Vol. 31, No. 1, pp. 654-657, May 1961.

188. Marston, C. H., Frind, G., Mishkovsky, V., "Research Study of Radiation Heat Flux from High Pressure Air Arcs", Arnold Engineering Development Center Report No. AEDC-TR-66-258, December 1966.

189. Neel, C. A., Lewis, Clark, H., "Interpolations of Imperfect Air Thermodynamic Data II. At Constant Pressure", Arnold Engineering Development Center, Report No. AEDC-TR-64-184, September 1984.

190. Kaminow, I. P., Ramaswamy, V., "Single-Polarization Optical Fibers: Slab Model," Applied Physics Letters, Vol. 34, No. 4, pp. 268-270, February 15, 1979.

191. Rashleigh, S. C., Marrone, M. J., "Temperature Dependence of Stress Birefringence in an Elliptically Clad Fiber," Optics Letters, Vol. 8, NO. 2, pp. 127-129, February 1983.

192. Kingery, W. D., "Surface Tension of Some Liquid Oxides and Their Temperature Coefficients", Journal of The American Ceramic Society, Vol. 42, No. 1, pp. 6-10, January 1959.

193. Shartsis, L., Spinner, S., Smock, A. W., "Surface Tension of Compositions in the Systems PbO-B_2O_3 and PbO-SiO_2", Journal of The American Ceramic Society, Vol. 31, No. 1, pp. 23-27, January 1948.

194. Parikh, N. M., "Effect of Atmosphere on Surface Tension of Glass", Journal of The American Ceramic Society, Vol. 41, No. 1, pp.18-22, January 1958.

195. Bani, R. E., Derge, G., "Surface Tensions of Silicates", Journal of Metals, Vol. 8, Transactions AIME, pp.53-59, January 1956.

196. Scholze, H., Kreidl, N. J., "Technological Aspects of Viscosity", pp. 223-273, in Glass: Science and Technology, Vol. 3: Viscosity and Relaxation, Ed. by D. R. Uhlmann and N. J., Kreidl, Academic Press, Inc., New York, 1986.

197. Hagy, H. E., "Rheological Behavior of Glass", pp. 343-371, Introduction To Glass Science, Ed. by L. D. Pye, H. J. Stevens, and W. C. LaCourse, Plenum Press, New York, 1972.

198. Das, A. K., Bhattacharyya, S., "Low-Loss Fusion Splices of Optical Fibers", Journal of Lightwave Technology, Vol. Lt-3, No. 1, pp. 83-87, February, 1985.

199. Meseguer, J., Sanz, A., Rivas, D., "The Breaking of Axisymmetric Non-Cylindrical Liquid Bridges", Proceedings of the 4th European Symposium on Materials Sciences Under Microgravity, Madrid, Spain, pp. 261-265, 5-8 April, 1983.

200. Meseguer, J., Sanz, "The Breaking of Axisymmetric Slender Liquid Bridges", Journal of Fluid Mechanics, Vol. 130, pp. 123-151, 1983.

201. Schwabe, D., Scharmann, A., Preisser, F., Oeder, R., "Experiments on Surface Tension Driven Flow in Floating Zone Melting," Journal of Crystal Growth Vol. 43, pp. 305-312, 1978.

202. Fu, Being-I, Ostrach, S., "Numerical Solutions of Floating-Zone Thermocapillary Flows," Proceedings of the 4th European Symposium on Materials Sciences Under Microgravity, Madrid, Spain, pp. 239-245, 5-8 April, 1983.

203. Levich, V. G., Krylov, V. S., "Surface-Tension-Driven Phenomena," pp. 293-316, Annual Review of Fluid Mechanics, Vol. 1, Edited by William R. Sears and Milton Van Dyke, Annual Reviews, Inc., Palo Alto, California, 1969.

204. Barakat, N., El-Hennawi, H. A., Medhat, M., Sobie, M. A., El-Diasti, F., "Interferometric Examination of Spliced Optical Fibers," Applied Optics, Vol. 25, No. 19, pp. 3466-3468, 1 October, 1986.

205. Vlack, L. H. V., Elements of Materials Science and Engineering, Fourth Edition, Addison-Wesley, Reading, Massachusetts, 1980.

206. Serafini, E., "Mechanical Strength of Optical Fiber Arc Fusion Splices," Vol. 1 of 5th International Conference on Integrated Optics and Optical Fibre Communication and 11th European Conference on Optical Communication (IOOC-ECOC '85), Venezia, Italy, October 1-4, 1985.

207. Sparrow, E.M., Cess, R.D., Radiation Heat Transfer, Revised Edition, Brooks/Cole, Belmont, California, 1970.

208. Parkus, Heinz, Thermoelasticity, Springer-Verlag/Wien, New York, 1976.

209. Saada, A.S., Elasticity Theory and Applications, Pergamon Press, Inc., Elmsford, New York, 1974.

210. Champion, F.C., Davy, N., Properties of Matter, Third Edition, Blackie and Son, Ltd., Glasgow, England, 1959.

211. Holland, L., The Properties of Glass Surfaces, John Wiley and Sons, Inc., New York, 1964.

212. Geyling, F.T., Homsy, G.M., "Extensional Instabilities of the Glass Fibre Drawing Process," Glass Technology, Vol. 21, No. 2, pp. 95-102, April 1980.

213. Obert, Edward F., Young, Robert L., Elements of Thermodynamics and Heat Transfer, Second Edition, McGraw-Hill Book Company, New York, 1962.

214. Burton, K. R., Anderson, B. J., "Evaluation and Application of Data from Low Gravity Orbital Experiment. Phase 2 - Marker and Cell Method for Solution of Fluid Dynamic Problems," Convair Division of General Dynamics, Final Report No. GDC-DDB70-004, NASA Report No. NASA-CR-102844, 31 July, 1970.

APPENDIXES

APPENDIX A

PHYSICAL PROPERTIES OF SILICA FIBERS

Fiber optic filaments of interest in this study are manufactured of high purity silica with a small amount of dopant added to the core and/or cladding region. The primary purpose of the dopant is to increase the index of refraction in the core region to produce an optical waveguide.

Popularity of silica as a fiber optic material is a result of its superior tensile strength, excellent light conduction, chemical inertness, and its resistance to thermal shock. The impurities (primarily Boric Oxide, B_2O_3, and Germania, GeO_2) are added to the core region in parts per million and have a limited but sometimes perceptible influence on the physical properties of fibers [196]. In this study, physical properties of the doped silica layers are assumed to be represented by those of the outer layers of pure silica. These are known to be similar in material properties to bulk fused silica. In the following sections, properties of bulk and filament shaped fused silica are given.

Most material properties change with temperature. This tendency is often less for silica than for many materials, primarily due to its low linear coefficient of thermal expansion. However, the material properties of silica do have an important impact on the surface evolution of the fiber filament and therefore need to be modeled with a high degree of fidelity. In the following section, thermal, mechanical, and optical properties of fused silica is given as a function of temperature where possible.

Material property values used in the analytical model have a significant impact on the fidelity of the results. Because of this sensitivity, a continual effort has been maintained to improve on the quality and accuracy of the functions used to represent the material properties. As a result, some of the functions used to obtain the results reported in this dissertation have been improved. In these cases, both functions are given.

Vitreous and Fused Silica

Silica can exist in a highly polymerized amorphous state known as vitreous silica or in several crystalline states. Fused silica is an aggregate of crystalline forms in an amorphous matrix. Both vitreous and fused silica exhibit similar material properties which therefore may be used interchangeably.

In general, the crystalline forms of silica do not exist in fibers because they are cooled very rapidly during the manufacturing process quenching in the amorphous vitreous silica state. Once cooled to a lower temperature, the energy required to reorder the molecules is unavailable to effect crystallization. This crystallization, known as devitrification, has been suggested as a root cause for the weakening of high silica fiber regions heated above 1100 °C in the arc fusion splicing process [191].

Melting Characteristics and Viscosity

Vitreous silica does not undergo a phase transition characteristic of true melting. Rather, it is a supercooled liquid and undergoes a

gradual softening similar to that characteristic of many waxes and plastics.

An initial function for the viscosity of fused silica was derived from a graph reported in the open literature [83]. This function was a double exponential curve fit given by:

$$\mu = 6\exp[42.931\exp(-1.0601 \times 10^{-3}T)] \qquad \text{(Eq. A-1)}$$

where μ is the absolute viscosity in poises

T is the absolute temperature in °K

Further study has resulting in the development of another function for the viscosity of fused silica which is believed to be of a higher fidelity. The following discussion gives the details of this development.

Commonly used definitions for describing the melting characteristics of glassy material relate the "stages of melting" to its viscosity [84]. These values are typically very large numbers and are normally represented as the value obtained after taking the logarithm to the base 10 of the viscosity in poises. The glass transition (strain point) temperature, T_{g1}, is the temperature at which the viscosity of the material equals 14.6 $\log_{10}$ poises. The stress relaxation (annealing point) temperature is the temperature at which the viscosity of the material equals 13.4 $\log_{10}$ poises. The yield (softening point) temperature is the temperature at which the viscosity of the material equals 7.6 $\log_{10}$ poises [196]. The flow point temperature is defined as the temperature at which the viscosity of the material equals 5 $\log_{10}$ poises. The working point temperature is defined to be the temperature

at which the viscosity of the material equals 4 $\log_{10}$ poises. The melting point temperature is defined to be the temperature at which the viscosity of the material equals 2 $\log_{10}$ poises [197]. A relationship between the viscosity of transparent fused silica and its temperature has been found to be [87]:

$$\log_{10}(\mu) = (3.05 \times 10^4/T) - 7.74$$

or (Eq. A-2)

$$\mu = 1.813 \times 10^{-8} \exp[(140{,}000 \text{ cal/mole})/R_gT]$$

where μ is the absolute viscosity in poises

R_g is the Universal Gas Constant (1.98588 cal/mole-°K)

T is the absolute temperature in °K

This equation gives the strain point temperature as 1092 °C, the annealing point temperature as 1170 °C, the softening point temperature as 1715 °C, and the flow point temperature is 2121 °C. The defined "stages of melting", corresponding viscosity values, and temperatures are given in Table A-1.

As shown in the table, the defined working point temperature (2325 °C) and the melting point (2856 °C) is never attained because silica volatilizes at 2310 °C. Therefore the viscosity of silica has a minimum of 4.07 $\log_{10}$ poises. The softening point temperature of 1715 °C is taken as that required for coalescence of silica in performing a fusion splice This temperature corresponds to an activation energy of 140 kcal/mole for viscous flow as seen in Eq. A-2. This value also corresponds well with the values of 1700-2100 °C given in the literature for the range of fusion temperatures [8, 9, 22]. It is noted, that the

higher splicing temperatures are often preferred due to the shorter splicing times required and therefore the less time for waveguide distortion to occur.

Table A-1. Melting Characteristics of Fused Silica

Defined Points	Viscosity (log_{10} poises)	Temperature (°K)
Strain Point (Glass Transition), T_{gl}	14.6	1365
Annealing Point (Stress Relaxation)	13.4	1443
Softening Point (Yield)	7.6	1988
Flow Point	5	2394
Working Point	4	-- *
Melting Point	2	-- *

* Silica volatilizes at 2583 °K corresponding to 4.07 in log_{10} poises

Thermal Conductivity

The true thermal conductivity of bulk fused silica as a function of temperature has been approximated by a third order polynomial and is given by [75]:

$$k_c = 9.373 \times 10^{-3} + 1.149 \times 10^{-5}T - 8.506 \times 10^{-9}T^2 + 4.559 \times 10^{-12}T^3 \qquad \text{(Eq. A-3)}$$

where k_c is the molecular thermal conductivity in W/cm-°K

T is the temperature in °K

The effective thermal conductivity for bulk fused silica is a strong function of temperature due to the presence of simultaneous conduction and radiation at temperatures in excess of 200 °K. At high temperatures, a considerable proportion of thermal energy in fused silica begins to be transmitted by radiation. This radiation adds to the apparent thermal conductivity in the optically thick limit (when the photon mean free path is small compared to the system dimension). In this case, an effective conductivity is given by [93]:

$$k_{eff} = k_c + k_{rad} \qquad \text{(Eq. A-4)}$$

where k_{eff} is the effective thermal conductivity

k_c is the molecular thermal conductivity

k_{rad} is the conductivity due to radiation

The coefficient of thermal conductivity due to radiation (the Rosseland approximation) can be expressed as [118]:

$$k_{rad} = 16 n_o^2 \sigma_{SB} T^3 / 3\mathring{a} \qquad \text{(Eq. A-5)}$$

where n_o is the refractive index

σ_{SB} is Stefan-Boltzmann's constant (5.67×10^{-12} Watt/cm^2-°K)

T is the absolute temperature in °K

$\mathring{a}$ is the absorption coefficient

The index of refraction and the absorption coefficient of fused silica in the above relationship is a function of the radiation wavelength and is given in the following sections. For the purposes of this calculation a value of 1.45 is used for the refractive index. A

value of 4 cm-1 is typically used for the absorption coefficient of silica optical fibers where the internal radiation is governed by the fiber temperature [92, 104].

The Rosseland approximation becomes invalid when the absorption coefficient times the material thickness is much less than unity. In the radial direction, the fiber thickness (diameter) is only 1.25×10^{-2} cm. The absorption coefficient of 4 cm^{-1} times the fiber diameter yields a value of 5×10^{-2} and the Rosseland approximation is, therefore, invalid in the radial direction.

Heat Capacity (Mean Specific Heat)

The heat capacity of fused silica at different temperatures is given in Table A-2 [75,196].

Table A-2. Heat Capacity of Fused Silica

Heat Capacity (J/g-°K)	Temperature (°K)
0.741	300
0.754	325
0.942	725
1.005	875
1.143	1675
1.189	1875
1.340	2275

The data for the heat capacity of bulk fused silica has been approximated by a third order polynomial and is given by:

$$C_p = 0.4903 + 10^{-3}T - 6.147\times10^{-7}T^2 + 1.486\times10^{-10}T^3 \quad \text{(Eq. A-6)}$$

where C_p is the heat capacity in J/g-°K

T is the temperature in °K

Linear Coefficient of Thermal Expansion

Fused silica has a low linear coefficient of thermal expansion which is responsible for its remarkable thermal shock resistance even though it is a glassy material. Data for the linear coefficient of thermal expansion was approximated by a second order polynomial given by [75]:

$$\alpha_{th} = (1.1228 - 2.0428\times10^{-3}T + 8.6463\times10^{-7}T^2)\times10^{-6} \quad \text{(Eq. A-7)}$$

where α_{th} is the linear coefficient of thermal expansion in cm/cm-°K

T is the temperature in °K

Further investigation has shown that this property can be better approximated by a piecewise linear relationship with a value of 5.5×10^{-7} cm/cm-°C below the glass transition temperature of 1092 °C and a value of 25×10^{-7} cm/cm-°C above the glass transition temperature [67, 83, 197].

Density

The very low value of the linear coefficient of thermal expansion gives silica excellent thermal shock resistance and permits rapid cooling of parts during manufacturing. This rapid quenching is

performed during the manufacture of silica fiber optic filaments [100, 101, 104, 109, 126-138]. One effect of the quenching process is the retention of the fused silica structure at lower temperatures.

Because of the very low thermal expansion properties of silica, the initial function for density used in the analytical model was assumed to be constant with a value of 2.2 gm/cm^3 (137.33 lb/ft^3). Further analysis indicates that this assumption may contribute to large "effective" stresses and the following discussion is provided to guide potential improvements in the fidelity of the model.

Transitions in silica take a significant amount of time [78,79]. The slow transitions usually result in a "freezing" of the higher temperature material structure which is maintained at the lower temperatures. This is the case for quenched fiber optic filaments made of high silica glass where the fused silica state is maintained at the lower temperatures.

For a given mass of isotropic material such as fused silica, the density at a given temperature is related to the density at a reference temperature and the linear thermal expansion coefficient by [205]:

$$\rho = \rho_0(1 + 3\alpha_{th}\Delta T)^{-1} \qquad \text{(Eq. A-7)}$$

where ρ is the density at the new temperature in g/cm^3

ρ_0 is the initial density in g/cm^3

α_{th} is the linear thermal expansion coefficient in °K^{-1}

ΔT is the change in temperature from the reference in °K

The change in the value of the linear coefficient of thermal expansion at a temperature of about 1092 °C results in a change in the

equation for density as a function of temperature over the same region. Therefore, two equations exist for the density of fused silica as a function of temperature. The first equation for the density of fused silica is valid up to the temperature of 1092 °C (1365 °K) and is given by:

$$\rho(<1365\ ^\circ K) = 2.202(1 + 1.65 \times 10^{-6}\ \Delta T)^{-1} \qquad \text{(Eq. A-8)}$$

where ρ is density at the new temperature in g/cm^3

ΔT is the temperature above the reference temperature of 300 °K (room temperature)

This equation gives the density of fused silica at 1365 °K as 2.198 g/cm^3. This value is used as the initial density for the second equation for the density of fused silica valid above the temperature of 1365 °K. This equation is given by:

$$\rho(>1365\ ^\circ K) = 2.197(1 + 7.5 \times 10^{-6}\ \Delta T)^{-1} \qquad \text{(Eq. A-9)}$$

where ρ is density at the new temperature in g/cm^3

ΔT is difference in the new temperature and 1365 °K

Data for the density of fused silica was obtained from the above two equations for the temperature range of 300 °K to 2300°K. This data was then approximated by a single third order polynomial equation given by:

$$\rho(300\text{-}2300\ ^\circ K) = 2.202 + 1.258 \times 10^{-6}T - 3.314 \times 10^{-13}T^2 - 3.716 \times 10^{-13}T^3 \quad \text{(Eq. A-10)}$$

where ρ is the density in g/cm^3

T is the absolute temperature in °K

Elastic (Young's) Modulus

The elastic modulus of fused silica is well approximated as a linear function of temperature and is given by [75]:

$$E = [745 + 0.1026(T - 300)] \times 10^3 \quad \text{(Eq. A-11)}$$

where E is the elastic modulus in kg/cm^2

T is the temperature in °K

Shear (Rigidity) Modulus

The shear modulus of fused silica is well approximated as a linear function of temperature and is given by [75]:

$$G = [320 + 0.0333(T - 373)] \times 10^3 \quad \text{(Eq. A-12)}$$

where G is the shear modulus in kg/cm^2

T is the temperature in °K

Poisson's Ratio

Poisson's ratio was initially derived from data supplied by a manufacturer of bulk fused silica [75]. This data was curve fit to a third order equation given by:

$$\eta = 0.1795 - 5.08273 \times 10^{5}T + 5.43895 \times 10^{-8}T^{2} - 1.21879 \times 10^{-11}T^{3} \quad \text{(Eq. A-13)}$$

It was later discovered that this relationship is not good at the higher temperatures experienced during the arc fusion splicing process. As a result, an improved function was sought. The Poisson's ratio for a material can be derived from its elastic modulus and its shear modulus by [205]:

$$\eta = (E/2G) - 1 \quad \text{(Eq. A-14)}$$

where η is Poisson's ratio

E is the elastic modulus

G is the shear modulus

Using the equations previously given for the elastic modulus and the shear modulus results in an equation for Poisson's ratio given by:

$$\eta = [745 + 0.1026(T - 300)]/[640 + 0.0666(T - 373)] - 1 \quad \text{(Eq. A-15)}$$

where η is Poisson's ratio

T is the temperature in °K

Surface Tension

Surface tension for fused silica has not been experimentally determined over the complete temperature range of interest. However, fiber manufacturing studies typically assume a surface tension of approximately 300 dynes/cm at a fiber spinning temperature of 1800 °C [133]. Other measurements of fused silica at 1800 °C have reported

values of 298, 310, and 313 dynes/cm [192]. Therefore, a value of 307 dynes/cm at 1800 °C was assumed in this effort.

The change in surface tension with temperature is given by an equation of the form [192, 193]:

$$\sigma = \sigma_0(1 + \Delta T d[\sigma]/dT) \qquad \text{(Eq. A-16)}$$

where σ is the surface tension at a new temperature

σ_0 is the surface tension at a known temperature

ΔT is the change in temperatures

$d[\sigma]/dT$ is the temperature coefficient of surface tension

A positive temperature coefficient ($d[\sigma]/dT$) on the order of 0.031 dyne/cm-°K has been reported for fused silica [192]. However, this trend was the result of interpolating between two different sets of experimental data. Each set of data showed fairly tight grouping but each set was obtained using different experimental methods. A decrease of surface tension with respect to temperature is more characteristic of most material and has been reported as having a slope of -0.017 dyne/cm-°C for fused silica exposed to dry nitrogen and air saturated with moisture [194].

The relationship for surface tension as a function of temperature used in this effort is given by:

$$\sigma = 342 - 0.017T \qquad \text{(Eq. A-17)}$$

where σ is the surface tension in dynes/cm

T is the temperature in °K

Absorption Coefficient

The absorption coefficient of fused silica determines the amount of radiation which is absorbed in a given thickness of material. In fused silica, its magnitude is not very sensitive to changes in temperature but is a relatively complex function of the radiation wavelength.

A useful approximation to the absorption coefficient has made by treating the spectral characteristics of fused silica as being composed of five discrete partially absorbing regions bordered by total absorption regions [79]. The value of the absorption coefficient in each of these regions is given in Table A-3.

Table A-3. Spectral Characteristics of Fused Silica

Wavelength (μm)	Absorption Coefficient (cm^{-1})
0.2 - 2.0	0.01
2.0 - 2.4	0.10
2.4 - 3.3	1.00
3.3 - 3.9	1.09
3.9 - 4.6	2.66
4.6 - ∞	∞

Radiation from the electric glow discharge is assumed to be blackbody in nature. Analysis of blackbody radiation indicates that almost no radiation energy (less than 1%) exist at wavelengths shorter than 0.2 μm for temperatures of interest (less than 7,000 °K). Over 50% of the radiation is in the wavelength band 0.2 - 2.0 μm for temperatures

above 2,000 °K. This percentage increases to over 75% for temperatures greater than 3,000 °K.

A composite absorption coefficient has been estimated by adding the contributions from individual wavelength bands. The contribution from each absorption region was calculated by integrating the radiant energy within each band and applying the appropriate absorption coefficient. This process was repeated for a range of black-body temperatures to determine a composite value for the absorption coefficient.

Radiant energy striking the surface of the fiber in each of the bands is given by:

$$e_{(\lambda_1-\lambda_2)} = [\int_0^{\lambda 2} e_\lambda \, d\lambda - \int_0^{\lambda 1} e_\lambda \, d\lambda]/\sigma_{SB}T^4 \qquad \text{(Eq. A-18)}$$

where e_λ is the monochromatic emissive power in watts/cm$^2\Delta\lambda$

$(\lambda_1-\lambda_2)$ is the wavelength band of interest

σ_{SB} is Stefan-Boltzmann's constant (5.67 x10^{-12} watt/cm^2°K^4)

T is the absolute temperature in °K

The monochromatic emissive power (spectral radiant energy emitted into a hemisphere), e_λ , is given for a black-body by Planck's distribution law:

$$e_\lambda = C_1\lambda^{-5}/[e^{(C_2/\lambda T)} - 1] \qquad \text{(Eq. A-19)}$$

where C_1 is a radiation constant

($C_1 = 2\pi c^2 h = 3.741832 \times 10^{-20}$ watt-cm^2)

C_2 is a second radiation constant

($C_2 = hc/k = 1.438786 \times 10^3$ cm-°K)

λ is wavelength of interest in cm

T is the absolute temperature in °K

c is the speed of light in a vacuum (3×10^{10} cm/sec)

h is Planck's constant (6.62618×10^{-34} joule-sec)

K is Boltzmann's constant (1.38066×10^{-23} joule/°K)

For this effort, the overall absorption coefficient for silica exposed to the electric discharge is taken as being constant with a value of 0.05 cm^{-1} over the glow discharge conditions of interest.

It is noted that the re-absorption of radiation emitted internally by the fiber contributes to the "effective" thermal conductivity of silica as previously discussed. For this calculation it is the temperature of the fiber which is important in determining the spectral distribution of the emitted radiation. Radiant heat transfer in silica fibers is dominant at temperatures above about 1000 °K. Over the temperature range between 1000 and 2000 °K between on-set of significant radiant heat transfer and typical arc fusion splicing temperatures, these values do not change dramatically. For these conditions, the absorption of fused silica has been estimated to be 4 cm^{-1} [104].

Absorptivity and Emissivity

Kirchhoff's law states that the emissivity and absorptivity of a real surface are equal for radiations with identical temperatures and wavelengths [213]. For a black-body or gray-body, this means that the emissivity and absorptivity are equal for all radiations at all temperatures and wavelengths.

Values for the emissivity of fused silica fibers have been given as ranging from 0.05 to 0.91 for fused silica over the temperature range of interest [76, 97, 104, 129-138, 212]. Part of the wide discrepancy is due to the fact that fused silica is a semi-transparent material where part of the emission of radiation is a bulk and not a surface phenomenon. These materials, are often treated as a "gray-body" where the emission of radiation is a volume emissive phenomenon related to the absorption of radiation.

One result of the volume dependence is that for dimensions on the order of the fiber diameter, the emissivity approaches zero [109]. It has been estimated, that the emissivity for silica with a thickness less than 0.2 cm is on the order of 0.1 [136]. Therefore, the value of emissivity of fused silica was taken to be the lower reported value of 0.1 for this effort.

Convective Heat Transfer Coefficient

The convective heat transfer coefficient is a function of material properties, surface characteristics, and the conditions of interaction with the gas in which the surface is immersed. It is particularly sensitive to the relative motion of the gas past the surface of the material. No experimentally measured values for the coefficient of heat

transfer corresponding to 125 μm diameter fibers placed horizontally in an AC glow discharge has been reported. A value of 5.7 $x10^{-4}$ cal/sec-cm^2-°C (~4.2 Btu/hr-ft^2-°F) has been reported as yielding satisfactory results in heat transfer calculations for arc fusion splicing [206].

It is noted, however, that values of 7.17 x 10^{-3} cal/sec-cm^2-°C (~53 Btu/hr-ft^2-°F) has been reported for the condition which exist in the furnace drawing of fiber optic filaments where forced cooling is employed [136].

Other values reported for the heat transfer coefficient of fiber optic filaments undergoing heating are 1 x 10^{-2} cal/sec-cm^2-°C (~73.8 Btu/hr-ft^2-°F) for the conditions which exist in CO_2 laser splicing of fibers and formation of spherical ends on fiber optic filaments [49,137]. A value of approximately 3.78 x 10^{-3} cal/sec-cm^2-°C (~28 Btu/hr-ft^2-°F) has been reported for 125 μm diameter silica fibers immersed in H_2/O_2 torch flames [129].

The uncertainty in the convective heat transfer coefficient for the 125 μm diameter fibers undergoing arc fusion splicing resulted in the use of initial values between 1 x 10^{-4} cal/sec-cm^2-°C (~0.74 Btu/hr-ft^2-°F) and 1 x 10^{-2} cal/sec-cm^2-°C (~74 Btu/hr-ft^2-°F). The value during the heating phase was estimated to be approximately ten times the value during the cooling phase.

By iteration, a value of 2.7 x 10^{-3} cal/sec-cm^2-°C (~20 Btu/hr-ft^2-°F) for the heating phase was found to yield fiber temperatures of approximately 2050 °C which corresponded to those reported throughout the open literature for optimum arc fusion splicing conditions [4-60]. It is noted that this value approximates that reported for H_2/O_2 torch

flame fusion of fiber optics where the gas turbulence might be expected to be similar to that in an electrical discharge [129].

A value of 2.7×10^{-4} cal/sec-cm^2-°C (~2 Btu/hr-ft^2-°F) was estimated for the heat transfer coefficient during the cooling phase where natural convection conditions exist and found to give satisfactory results. This value provides fiber cooling times on the order of a few seconds in reasonable agreement with values reported in the open literature [100, 101, 109, 129, 130].

APPENDIX B

GRAVITATIONAL FORCES ON FLUID REGION

During the arc fusion splicing of fiber optic filaments, a portion of the fiber is placed horizontally in an electric discharge heating zone. As the fiber temperature increases, its viscosity decreases. As a result the fiber material characteristics undergo a transition from those of an elastic solid to those of a viscous fluid. Most fluids undergo flow in response to body forces such as those due to gravitational acceleration.

The following discussion is directed toward establishing the relative importance of gravitational forces when compared to surface tension forces in influencing the viscoelastic response of the heated fiber.

A worst case approach is taken which maximizes the gravitational forces and minimizes the surface tension forces. This is achieved by assuming a uniformly heated length of fiber is suspended vertically by surface tension forces alone. The mass of the heated fiber is chosen to represent the maximum length of fiber which is above silica's 1092 °C glass transition temperature when undergoing an arc fusion splicing operation. A density characteristic of silica at 1092 °C is used. Surface tension forces are minimized by using a surface tension characteristic of that for silica at the 2050 °C maximum temperature of a fiber undergoing an arc fusion splicing operation. A nominal 125 micron fiber diameter is initially assumed.

The length of silica fiber heated above the glass transition temperature when undergoing an arc fusion splicing operation is

typically less than the electrode spacing [28, 38, 158]. This observation is borne out in the analytical results obtained using the arc fusion splicing model.

The gravitational force at the suspension interface due to a length of heated fiber material is given by:

$$F_g = \rho g(L\pi r^2) \qquad \text{(Eq. B-1)}$$

where F_g is the gravitational force at the interface

ρ is the density of the silica fiber material at 1092 °C (2.198 g/cm^3)

g is the acceleration due to gravity at the Earth's surface (980.7 cm/sec^2)

L is the heated length of fiber (0.15 cm)

r is the radius of the fiber (6.25 x 10^{-3} cm)

This yields a value of 3.96 x 10^{-2} dynes for the total gravitational force due to the suspended length of heated fiber.

The force at the suspension interface due to surface tension is given by:

$$F_S = 2\pi\sigma r \qquad \text{(Eq. B-2)}$$

where F_S is the surface tension force at the interface

σ is the surface tension of the silica fiber material at 2050 °C (302.5 dyne/cm)

r is the radius of the fiber (6.25 x 10^{-3} cm)

This yields a value of 11.9 dynes for the total surface tension force at the suspension interface.

The value calculated for the surface tension force is more than two orders of magnitude greater than that determined for the gravitational force when assuming worst case conditions. It is therefore concluded that the gravitational force on the fiber undergoing arc fusion splicing is negligible.

APPENDIX C

FOSPLICE COMPUTER PROGRAM

Practical solution of the numerical algorithms developed for the arc fusion model require the use of a computer system. This section is devoted to the description of the program developed to carry out the calculations, file handling, input/output requirements, and operator control of the program status.

Program Overview

As pointed out in Chapter I, an objective of this study was to develop a widely adaptable computer code. It was decided to use a computer language which was well known and available for a large number of computer systems. BASIC was chosen as the programming language because it met these requirements and because it is an interpreted language which enhances its ease of modification and adaptability. In addition, BASIC compilers are available which can generate an executable code which runs faster but is less conveniently modified if this tradeoff is desirable. Although the program and/or parts of it were developed and run primarily on the IBM/PC compatible family of computers, every attempt was made to keep the program generic. Graphic routines were included as subroutines to facilitate their conversion or omission. This approach was taken because of the lack of standard graphic output commands. Graphic output routines, therefore, are typically unique for operation on specific computer systems, computer languages, and printer/plotter combinations.

The program, entitled FOSPLICE, was structured to run in a interactive mode with a menu driven main routine and many specialized subroutines. Subroutines were used extensively in order to enhance the structured nature of the program and to add to the ease with which it could be maintained and modified. These subroutines initialize the program, present information and menu displays to the program operator, perform file handling operations, perform calculations, and control input/output operations. The general program structure is shown in Figure C-1.

FOSPLICE is composed of three major parts. The first part consists of a very short main program which consists of a series of subroutine calls. These subroutines are responsible for displaying program information to the operator, program initialization, setting default values for variables, and initializing values used in internal calculations. The second major part of the program consists of menu driven subroutines which permit operator interaction with the program. These subroutines are responsible for controlling keyboard entry of program changes, parameter data file handling, displaying the current parameter values, entering the algorithm calculation portion of the program, and exiting the program to BASIC. The third major part of the program consists of subroutines implementing the numerical algorithms for heat transfer, viscoelastic glass flow, and matrix algebra.

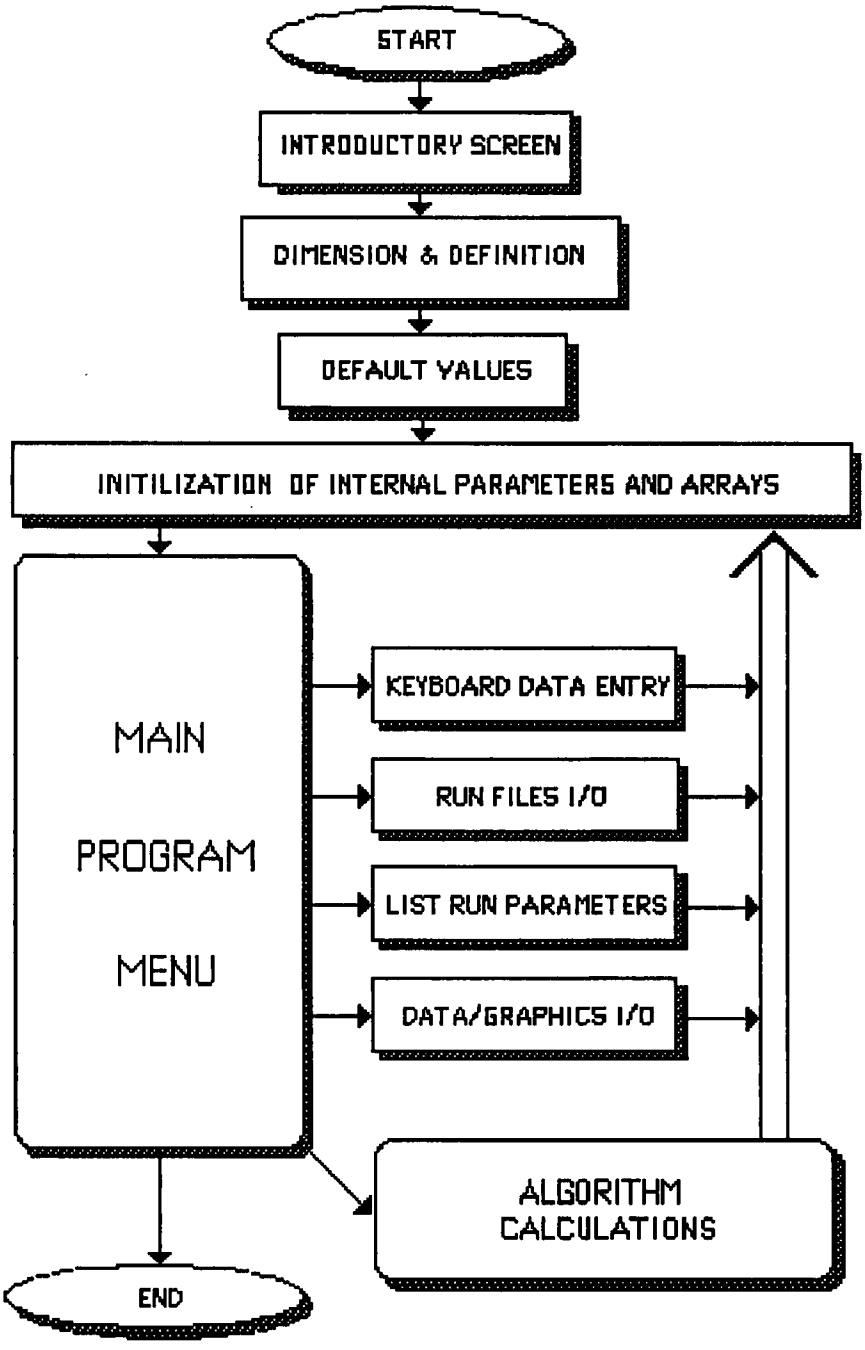

Figure C-1. Structure of FOSPLICE program

Program input and output consists of communications with the program operator, a diskette storage device, and a line printer. Communication with the program operator is provided through output to the screen and input from the keyboard in a normal manner. Printer output program statements contained in early versions of FOSPLICE were eliminated in favor of a monitor screen-print command entered from the keyboard. This added to program brevity and enabled a more thorough internal documentation through the liberal use of remark statements.

Initial Subroutines

Immediately upon running FOSPLICE, an introduction subroutine presents program information to the operator with a series of print statements. These print statements include the name and version of the program, a brief description of its utility, and the names and affiliations of the principal authors.

A dimension and definition subroutine sets up memory allocation for numeric and string variables. It defines functions used in internal calculations and defines functions used in the calculation of material properties. These material property functions are derived from curve fits of empirical data valid for the range of conditions expected in the arc fusion splicing process. The material property functions are physically located near the end of the program listing to permit ease of alteration for use with fibers which are not made from nearly pure silica.

A default subroutine establishes default values for all of the input variables used in the program. Defaults are included to speed operator response to questions and reduce operator fatigue. Values for

the defaults are based on safe-sided answers and on frequently given answers. The default value subroutine is physically located near the end of the program listing to permit ease of location and alteration.

An initialization subroutine is executed to set constants, convert conventional units to standard units, and initialize variables used in internal calculations. This subroutine is executed each time new values for variables are entered either from the keyboard, default values, or from diskette storage files.

Menu Selected Subroutines

The main program of FOSPLICE turns program control over to a menu driven subroutine for operator interaction. This menu presents the program operator with choices of individual subroutines for special activities. The operator may elect to enter values of splicing parameters from the keyboard, read parameter values from a diskette storage file, store parameters in a diskette storage file, list the current parameter values on the screen, alter the extent of output data, enter into arc fusion splice modeling calculations, or exit from program control to BASIC.

Keyboard entry of program control data is grouped into the categories of fiber heating conditions, splicing parameter variations, and simulation algorithm calculation controls. Fiber electric discharge heating conditions include conventional splices with an initial gap between filament ends, repeated heating of the splice region, heating of an unbroken fiber, and heating of a single fiber filament end. Splicing parameters which can be modified by keyboard entry include the discharge current, discharge time, room temperature, atmospheric

pressure, heating time before the press stroke, and the length of the press stroke. Calculation controls include the number of cells used to model the fiber length, size of each cell, total number of time steps over which the model runs, and the incremental length of each time step.

All information entered from the keyboard may be stored in and read from a diskette sequential data file to permit the creation of standard run conditions and to facilitate documentation. The operator is queried for a data file name and is permitted to preview all diskette directories prior to responding. The file extension "PRM" is suggested as a means of identifying parameter data files.

Current values of all operator selectable parameters plus a few set by the default subroutine may be listed on the monitor screen. A printout of this list may be obtained in the standard fashion of entering a screen-print command from the keyboard.

Output from the simulation algorithm calculations may be presented as an expanded list showing many of the intermediate values calculated, or an abbreviated list showing only the final results. The former is quite useful for understanding how the final results were obtained or as a diagnostic aid while the latter is much faster for routine runs.

A graceful exit to the BASIC interpreter is allowed as one of the options to permit the entry of microprocessor system level commands. This avoids the time delay of a system reboot and maintains the program intact in memory.

Subroutines which perform calculations of heat transfer and the viscoelastic response of the fiber optic filaments are presented in the following sections.

Heat Transfer and Viscoelastic Flow Subroutines

Subroutines implementing the numerical algorithms for heat transfer, viscoelastic glass flow, and matrix algebra constitute the heart of the FOSPLICE program.

Heat transfer and viscoelastic flow calculations were performed in a cyclic fashion for each time step as shown previously in Figure II-3 on page 18. Parameters were adjusted as a function of time to represent heating or cooling conditions. The overall procedure for each time cycle was to determine the temperature profile along the fiber from heat transfer algorithms, update the temperature dependent fiber properties within each cell, determine the viscoelastic flow resulting from stress calculations, and determine the resulting fiber profile for use in the next cycle of calculations.

Values for the parameters of each cell were tracked by means of one dimensional variable arrays. In addition, where calculations required values of parameters before and after a time step, separate variable arrays were used. These arrays were updated in each time step. Prior to the closure of the gap region, parameter values were calculated for the left and right portion of the fiber separately.

Coupling of heat transfer calculations across the gap region was by means of an "effective" heat transfer coefficient. Thermal conductivity across the gap region was determined by a routine which adjusted the value between the gas thermal conductivity value and the silica thermal conductivity as a function of gap distance. This provided a smooth transition of the value during gap closure.

Calculation of the heat transfer includes a calculation of the heat flux to and from the electric discharge and surrounding air along

with thermal transfer between the fiber elements. These calculations follow a calculation sequence shown in Figure C-2. Calculation of viscoelastic flow includes a calculation of stresses on the fiber elements and their resulting strains. These strains constitute the glass flow which is seen as a change of the fiber surface curvature and follow a calculation sequence shown in Figure C-3.

For the heat transfer calculation sequence, time and geometry input data are required to enable the position of fiber elements relative to the electric discharge be adjusted for mechanical fiber motion, thermal expansion, and viscoelastic flow. In addition, viscoelastic flow required that each cell geometry be tracked throughout the process. Temperatures were calculated for the midpoints of each cell by essentially establishing conservation of energy relationships between each cell and its nearest neighbors then solving all their equations simultaneously. A matrix technique was used to solve the equations efficiently due to their resulting tri-diagonal nature.

For the viscoelastic flow calculation sequence, fiber temperature profile and material property as a function of temperature are input along with the fiber geometry.

Stresses were determined for the axial and radial direction independently in sequential routines. Prior to gap closure, mechanical stresses were calculated for each fiber end by assuming free expansion into the gap region. After gap closure, stresses in each cell was adjusted to include mechanical forces due to the clamped ends. This was accomplished by adjusting the boundary conditions upon gap closure in a routine which included the effects of a press stroke if present.

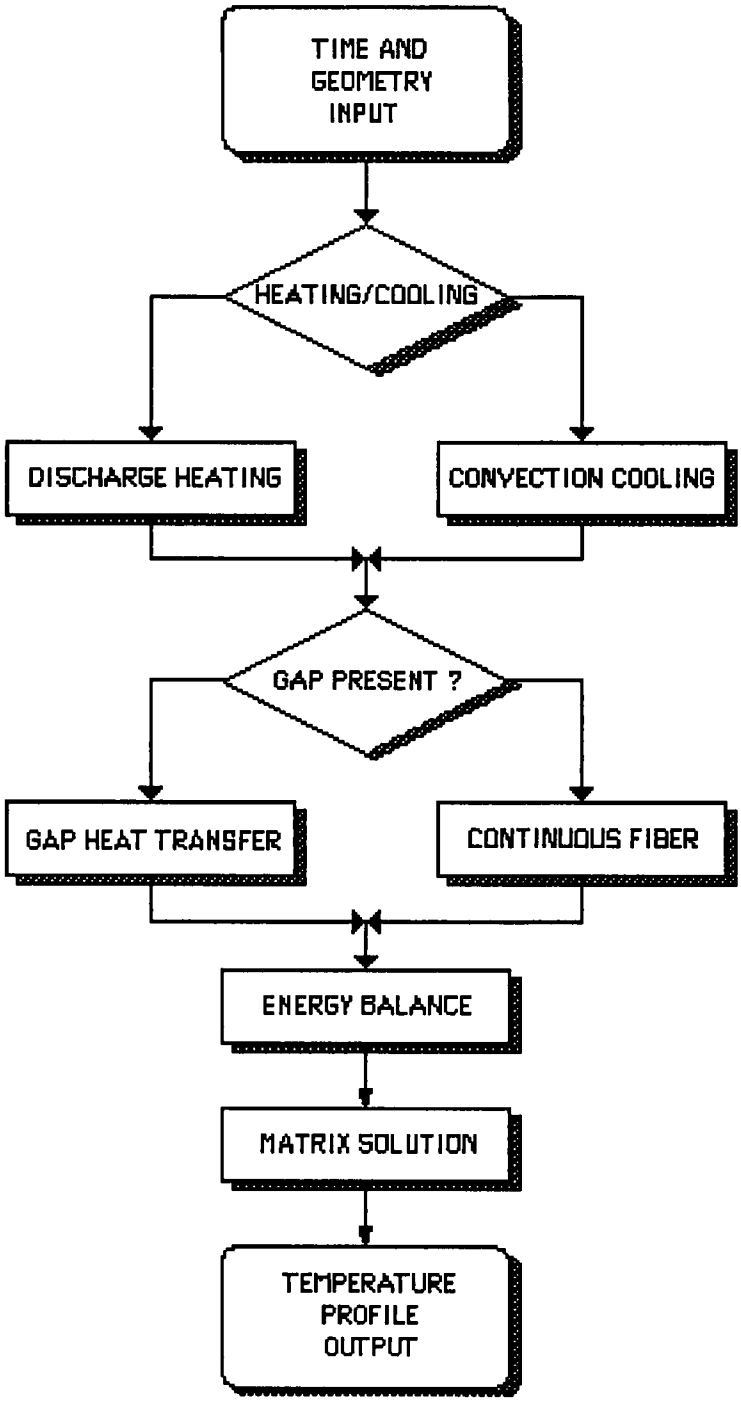

Figure C-2. Heat Transfer Calculation Sequence

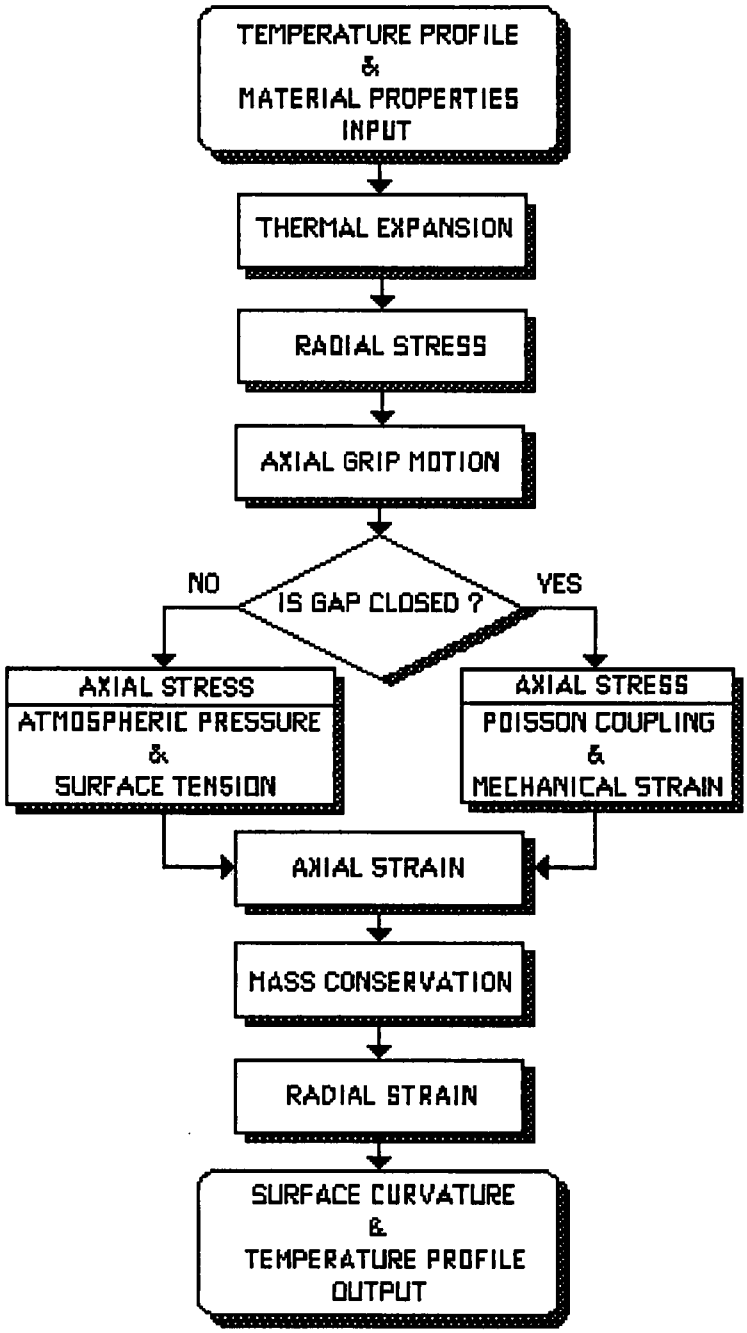

Figure C-3. Viscoelastic Flow Calculation Sequence

A routine determines the stress resulting from a press stroke within each time step. This stress is added into the mechanical stress resulting from all other causes. Press stroke strain rate values were converted into stress values by using a Maxwell viscosity model with the viscosity set to the lowest value in the fiber for each time step. This value was determine by locating the highest temperature in the fiber and using the viscosity of silica at that temperature.

Strains were determined from total stresses by using a Maxwell type relationship for the viscoelastic response of the heated silica. These routines included a coupling between the axial and radial directions by requiring conservation of mass in the calculation of each cell radius. The fiber surface contour was then calculated from each cell radius by performing a curve fit along adjoining cells.

As previously mentioned, output of data was initially restricted to the monitor screen with printouts obtained by the use of a screen-print keyboard command. This data was in the form of an abbreviated or complete listing.

VITA

VITA

The author, C. Wayne Long, was born in Wynne, Arkansas on July 15, 1952 as the son of Mr. and Mrs. H.C. Long. He graduated from Wynne High School in May 1970 where he studied mathematics, chemistry, and physics.

He graduated from Arkansas State University (ASU) in 1973 with a Bachelor of Science degree and a physics major. There he expanded his studies to include electronics and computer programming.

He graduated from Memphis State University (MSU) in 1975 with a Master of Science degree and a physics major. He elected to pursue a thesis topic on the construction of cryogenically cooled solid state thin film quantum mechanical devices known as Josephson Junctions.

He served as an intern for NASA at the Space Science Laboratory of the Marshall Space Flight Center in Huntsville, Alabama in 1975. There, he helped design spectroscopic and radiosonde instrumentation.

He supported magnetohydrodynamic (MHD) research at the University of Tennessee Space Institute (UTSI) as a materials engineer in 1975. There, he specialized in slag resistant refractories, high temperature polymer insulators, sealants, and noble metal cladding for oxidation/sulfidation protection of electrodes.

He joined Precision International in Tullahoma, Tennessee as an optical design engineer in 1981. There, he was responsible for the design and testing of prototype optical rangefinding instrumentation.

The author joined BDM International in Huntsville, Alabama in 1982 as a systems analyst. There, he supported the Department of Defense's strategic and tactical defense programs in efforts related to optical engineering, material science, and computer science.